



저작자표시-비영리-변경금지 2.0 대한민국

이용자는 아래의 조건을 따르는 경우에 한하여 자유롭게

- 이 저작물을 복제, 배포, 전송, 전시, 공연 및 방송할 수 있습니다.

다음과 같은 조건을 따라야 합니다:



저작자표시. 귀하는 원저작자를 표시하여야 합니다.



비영리. 귀하는 이 저작물을 영리 목적으로 이용할 수 없습니다.



변경금지. 귀하는 이 저작물을 개작, 변형 또는 가공할 수 없습니다.

- 귀하는, 이 저작물의 재이용이나 배포의 경우, 이 저작물에 적용된 이용허락조건을 명확하게 나타내어야 합니다.
- 저작권자로부터 별도의 허가를 받으면 이러한 조건들은 적용되지 않습니다.

저작권법에 따른 이용자의 권리는 위의 내용에 의하여 영향을 받지 않습니다.

이것은 [이용허락규약\(Legal Code\)](#)을 이해하기 쉽게 요약한 것입니다.

[Disclaimer](#)

공학박사학위논문

고체산화물 연료전지와
스파크-어시스트 점화 엔진의
하이브리드 시스템 설계 및 최적 운전

System Design and Optimal Operation for a Hybrid
System of a Solid Oxide Fuel Cell and an Internal
Combustion Engine Using Spark-assisted Ignition

2019 년 8 월

서울대학교 대학원

기계항공공학부

김 재 현

고체산화물 연료전지와
스파크-어시스트 점화 엔진의
하이브리드 시스템 설계 및 최적 운전

System Design and Optimal Operation for a Hybrid
System of a Solid Oxide Fuel Cell and an Internal
Combustion Engine Using Spark-assisted Ignition

지도교수 송 한 호

이 논문을 공학박사 학위논문으로 제출함

2019년 4월

서울대학교 대학원

기계항공공학부

김 재 현

김재현의 공학박사 학위논문을 인준함

2019년 7월

위원장 : 김 민 수



부위원장 : 송 한 호



위원 : 민 경 덕



위원 : 도 형 록



위원 : 안 국 영



Abstract

System Design and Optimal Operation for a Hybrid System of a Solid Oxide Fuel Cell and an Internal Combustion Engine Using Spark-assisted Ignition

Jaehyun Kim

Department of Mechanical Engineering

The Graduate School

Seoul National University

The objective of the proposed hybrid system is to increase system efficiency by using the residual fuel of anode off-gas from a solid oxide fuel cell (SOFC) in an internal combustion engine (ICE). In this study, a novel hybrid system using spark-assisted ignition (SAI) in ICE operation is proposed. Since it is the first attempt to use such a new combustion concept in the hybrid system, feasibility of SAI and its effect on the system operation are investigated in this study. Furthermore, a novel system configuration is designed for the optimal operation of the hybrid system of a SOFC and an ICE using SAI, based on natural gas. This is the first study to find the optimal configuration design of the SOFC-ICE hybrid system through case study which includes all the possible configurations

considering heat transfer quality for the most efficient balance of plants (BOPs) operation. In the end, optimal operating conditions affecting power generation related to electrochemical and combustion reaction such as load distribution and air supply rate for SOFC and SAI engine are investigated through response surface method (RSM).

The SOFC-SAI engine hybrid system consists of a fuel cell, an engine, external reformers, heat exchangers, catalytic oxidizer and mixers. For system-level analysis, simplified zero-dimensional simulation model was developed except the SAI engine. Especially, fuel cell model was developed considering electro-chemical, internal reforming and water-gas shift reaction, and validated with stack experimental data including load, fuel composition and air flow rate variation. The feasibility and performance of the SAI engine was investigated directly through actual experiments with a single-cylinder engine under all the operable ranges. Finally, analysis on the energy conversion system performance was conducted by integrating the engine experiment results with the simulation model for fuel cell and BOPs.

Firstly, in order to analyze only the effect of the combustion nature on the system, the engine experiments on the SAI were conducted by changing only the engine operating parameters, such as the intake temperature, equivalence ratio and spark timing. As a result, the performance of the hybrid system using SAI was analyzed in terms of both energy and exergy perspectives. In the operating conditions of this study, it was confirmed that the anode off-gas combustion can be controlled stably (COV: 5–7%) through the SAI, even though the intake temperature is decreased to $\sim 280^{\circ}\text{C}$ at the low compression ratio of 8.2. It enables better use of thermal energy in the hybrid system, and it leads to increase in

exergy efficiency of engine to ~37%. Consequently, thermal self-sustainability is improved and indicated efficiency of ~61.6% is achieved in the hybrid system. In the operating condition, the SAI engine is responsible for ~14% of the system power and produces considerably low NOX emissions ($< \sim 3$ ppm at 15% O₂ on a dry basis).

Secondly, system configuration has been newly developed for the further improved self-operability and system efficiency. Thus, case study of system configurations was performed for the optimal thermal energy distribution, considering the heat transfer quality between heat source and heat sink, e.g., available thermal energy of anode/cathode off-gas and required heat-supply for BOPs operation. Consequently, for the increased external reforming which is important for the hybrid system operation including a fuel cell based on natural gas, the configuration and the arrangement of external reformers have been re-designed. Furthermore, in order to recover the residual heat loss of system exhaust due to pinch limit at a heat exchanger for steam generation, an additional heat exchanger was adopted for the hybrid system.

Finally, optimization of operating conditions was performed for the novel SOFC-SAI hybrid system proposed in this study. Prior to the optimization process, parametric study was conducted to understand the hybrid system behavior. Based on the parametric study results, design of experiment (DOE) and response surface method (RSM) were used for the optimization of operating conditions, i.e., fuel utilization, air utilization in the fuel cell and equivalence ratio of the engine. The response surface of the energy conversion system is a multiple linear regression model obtained by least squares method (LSM), using observation data by DOE. The optimal design point on the response surface was

investigated by solving the non-linear inequality constraint problem, considering the system operability, i.e., combustion stability in the engine and thermal self-sustainability of the fuel cell. Consequently, the 5-kW class SOFC-SAI engine hybrid system is expected to be capable of achieving the promising efficiency of ~63.2% in the novel system design which has the efficient structure for the optimal heat distribution of anode/cathode off-gas. Furthermore, optimal and off-design operating characteristics of the hybrid system are discussed in this study.

In conclusion, this study proposed a novel hybrid system of a SOFC and an ICE using spark-assisted ignition, which refers to multiple combustion strategies, including spark-assisted homogeneous charge compression ignition (SA-HCCI or SACI) as well as conventional spark ignition (SI). This is the very first study implementing such new combustion concept in the SOFC-ICE hybrid system. Feasibility of such SAI operation was investigated through the actual engine experiment. Based on the investigation, SAI has been adopted in the hybrid system for the ICE operation to cope with ever-varying anode off-gas from the fuel cell stack. The SAI engine could properly combust the almost non-diluted fuel during the system start-up as well as fully-diluted fuel in the design-point operation. Furthermore, the optimal operation for the novel hybrid system designed considering the efficient thermal energy distribution of anode/cathode off-gas was investigated. In the end, it has been confirmed that operability and efficiency of the 5-kW class SOFC-SAI engine hybrid system are improved. This study is expected to have a considerable significance in the areas of energy conversion system due to the growing demands on natural gas and its promising system efficiency, and to contribute to development and commercialization of SOFC-ICE hybrid system.

Keywords:

Fuel cell, Solid oxide fuel cell–internal combustion engine hybrid system, Synthesis gas combustion, Spark ignition, Spark-assisted compression ignition, System-level modeling and analysis, System design, Optimal operation, System efficiency

Identification Number : 2013 – 23058

Contents

Abstract.....	i
Contents.....	vi
List of Figures.....	x
List of Tables.....	xv
Nomenclature.....	xvi
Chapter 1. Introduction	1
1.1. Combined cycle of SOFC.....	1
1.2. SOFC-ICE hybrid system.....	3
1.3. Optimization of SOFC hybrid system	6
1.4. Research motivation and objectives	8
1.5. Summary.....	11
Chapter 2. Feasibility of spark-assisted ignition engine in SOFC-ICE hybrid system	14
2.1. Research methodology	14
2.1.1. System configuration	14
2.1.2. Engine experimental apparatus	19
2.1.3. Simulation model descriptions	24
2.1.3.1. Fuel cell model	24
2.1.3.2. BOP model.....	29
2.1.4. Assumptions for the system-level analysis	31
2.1.5. Integration of engine experimental results and simulation model for system-level analysis.....	32
2.2. Details for operating conditions of the hybrid system.....	36
2.2.1. Available control and geometric parameters	36
2.2.2. Operating conditions for the engine experiment and the system operation.....	39

2.2.3. Definitions of related terms.....	41
2.3. Engine experimental results.....	44
2.3.1. HCCI under intake temperature variation	44
2.3.2. Spark-assisted ignition at the late-burn HCCI cycle condition	47
2.3.3. Spark-assisted ignition under intake temperature variation	51
2.3.3.1. Desirable spark timing for stable combustion and maximum indicated work.....	51
2.3.3.2. Operating performance at the desirable spark timing	53
2.3.4. Combustion mode under intake temperature variation	57
2.4. System performance	63
2.4.1. Improvement in efficiency and thermal self-sustainability	64
2.4.2. Improvement in exergy destruction.....	70
2.5. Conclusions	75
Chapter 3. Design of system configuration for the SOFC-SAI engine hybrid system	77
3.1. Considerations	77
3.1.1. Thermal energy distribution of anode/cathode off-gas	77
3.1.2. Order of heat-supply for each BOP operation.....	82
3.2. Details in designed configuration	85
Chapter 4. Parametric analysis on the SOFC-SAI engine hybrid system operation.....	88
4.1. Research methodology	88
4.1.1. Assumptions and feasible operating conditions	89
4.1.1.1. Assumptions for system-level analysis.....	89
4.1.1.2. Feasible operating conditions	91
4.1.2. Integration of engine experimental results and simulation model for system-level analysis.....	93
4.1.2.1. Engine experimental setup.....	93
4.1.2.2. Simulation model descriptions.....	95

4.1.2.3. System-level analysis.....	97
4.2. Details in the hybrid system operation	101
4.2.1. Parameter selection	101
4.2.2. Engine experimental conditions	104
4.3. Engine experimental results under variation of fuel utilization and equivalence ratio	106
4.3.1. Intake gas	106
4.3.2. Combustion characteristics	108
4.3.3. Power	113
4.3.4. Exhaust gas.....	115
4.4. Effect of parameter variation on the system performance	122
4.4.1. Effectiveness of external reformers.....	122
4.4.2. Fuel utilization and equivalence ratio	126
4.4.2.1. External reforming.....	126
4.4.2.2. Fuel cell operation	128
4.4.2.3. System performance	130
4.4.3. Fuel utilization and air utilization	132
4.4.3.1. External reforming.....	132
4.4.3.2. Fuel cell operation	134
4.4.3.3. System performance	136
Chapter 5. Optimization of operating conditions for SOFC-SAI engine hybrid system	138
5.1. Methodology for optimization.....	138
5.1.1. Design of experiment.....	138
5.1.2. Response surface method.....	138
5.2. Optimization results.....	140
5.2.1. Design of experiment and response surface	140
5.2.1.1. Variables of DOE.....	140
5.2.1.2. Response surface and constraint surfaces	141

5.2.2. Performance at design/off-design operation.....	144
5.2.2.1. Fuel cell and engine operation.....	144
5.2.2.2. BOP operation.....	147
5.2.2.3. Optimal operation (design point).....	151
5.3. Conclusions	153
5.4. Discussions.....	155
Chapter 6. Summary and Conclusions.....	157
6.1. Modeling for system-level analysis.....	158
6.2. Feasibility of SAI operation in engine.....	159
6.3. System design.....	161
6.4. Optimal operation.....	162
Appendix A. Fuel cell modeling based on steady-state and zero- dimensional equation.....	164
A.1. Specifications of the fuel cell model.....	164
A.2. Thermodynamic states in anode and cathode	164
A.3. Current, voltage and heat transfer of the fuel cell.....	165
Appendix B. Ignition delay calculation	171
Appendix C. Stream properties of SOFC-SAI engine hybrid system (in Chapter 2)	174
Appendix D. Equation of the response surface.....	175
Appendix E. Stream properties of SOFC-SAI engine hybrid system at the optimal operation (in Chapter 5)	176
References	177
국문 초록	184

List of Figures

Figure 1.1 – Increase in natural gas demand (consumption) [5]	2
Figure 1.2 – Electric efficiency and LCOE: SOFC stand-alone, SOFC-GT hybrid system and SOFC-HCCI engine hybrid system; re-produced from [12]	3
Figure 1.3 – Research motivation and objectives: combustion strategy, system design and optimization of SOFC–ICE hybrid system	13
Figure 2.1 – Configuration of SOFC–SAI engine hybrid system	18
Figure 2.2 – Experimental apparatus: engine and peripherals.....	20
Figure 2.3 – Experimental apparatus: (a) Engine (Honda GX 390) (b) In-house oil cooler (c) Encoder and coupling (d) spark plug integrated in-cylinder pressure sensor (Kistler)	21
Figure 2.4 – Experimental apparatus: (a) 12-kW heater (Watlow) (b) Exhaust analyzer (Greenline MK 2) (c) Mass flow controller (Bronkhorst and Brooks).....	22
Figure 2.5 – Experimental apparatus: (a) Engine experimental system (b) Simulink model for data acquisition and equipment control	23
Figure 2.6 – SOFC model validation: (a) changes in load, fuel composition, reformed gas temperature and air flow rate (b) reformed gas temperature variation (c) estimation of anode in/outlet states.....	28
Figure 2.7 – External reformer model validation with experimental results from [2]: under variation of reformed gas temperature	30
Figure 2.8 – Iteration sequence of system-level analysis on the hybrid system.....	35
Figure 2.9 – Engine intake conditions in the hybrid system: equivalence ratio and intake temperature varied with heat extraction from anode off-gas.....	38
Figure 2.10 – HCCI averaged-cycle characteristics under intake temperature variation (400–440°C): (a) combustion stability (COV) and combustion phasing (CA50) (b) net indicated power (c) exhaust temperature (d) CO emission and combustion efficiency (e) NO _x emission and peak of mean in-cylinder temperature (f) measured in-cylinder pressure; estimated results from experimental data: CA50, combustion efficiency and peak temperature (red line in (a), (d), (e)).....	46

Figure 2.11 – Cycle-to-cycle variations of the HCCI and SAI cycles at the extremely late-burn condition of the HCCI described in Section 2.3.1: (a) return maps of gross indicated power (b) in-cylinder pressure profile for individual cycles and estimated CA50 from the pressure profile.....	47
Figure 2.12 – Desirable spark timing region for stable combustion and maximum indicated work: (a) stable combustion region and MIW on the COV map [%] (b) gross indicated work under spark timing variation	51
Figure 2.13 – Correlation of combustion stability and power with CA50 controlled by SAI: (a) COV(GMEP) under CA50 variation (b) gross indicated power under CA50 variation.....	53
Figure 2.14 – Operating performance of the SAI at the MIW region: (a) CO emission and combustion efficiency (b) NO _x emission and peak of mean in-cylinder temperature (c) exhaust temperature (d) available sensible energy of anode off-gas and exhaust (e) indicated power (f) estimated heat loss of engine.....	56
Figure 2.15 – Laminar flame speed of methane and anode off-gas under equivalence ratio variation calculated using Cantera toolbox and GRI 3.0 mechanism	57
Figure 2.16 – Combustion phasing and duration under spark timing and intake temperature variation: (a) CA10 [CAD aTDC] (b) combustion duration from CA10 to CA90 [CAD].....	58
Figure 2.17 – SAI combustion characteristics predicted by Livengood–Wu correlation during combustion process: (a) net heat release rate profile (b) auto-ignition probability in the unburned gas on the Livengood–Wu integration map...59	59
Figure 2.18 – Effect of the SAI engine on the hybrid system operation: (a) total reforming rate and reformed gas temperature (b) power of the hybrid system (c) heat transfer of the fuel cell to the environment to achieve the fuel cell operating temperature (750°C) (d) indicated efficiency of the hybrid system including the additional heat-supply requirements as represented in the negative values of Figure 2.18(c)	64
Figure 2.19 – Exergy analysis on the hybrid system: (a) flow exergy of the hybrid system exhaust (b) exergy destruction in the hybrid system.....	70
Figure 2.20 – Exergy destruction in fuel cell and BOPs by additional BOPs (intake temperature = 362°C).....	72
Figure 2.21 – Exergy and indicated efficiency of the engine under the intake temperature (equivalence ratio) variation.....	73

Figure 3.1 – Energy flow of anode/cathode off-gas in SOFC–SAI engine hybrid system.....	77
Figure 3.2 – All the possible cases for system configuration based on Table 3.1 ..	81
Figure 3.3 – Operating temperature range of BOPs and flow diagram for thermal energy of the anode/cathode off-gas in the Case 2 discussed in Figure 3.2	82
Figure 3.4 – All the possible configurations of heat exchange for external reforming and cathode air heating by using engine exhaust and cathode off-gas: (a),(b) cathode off-gas → cathode air heating → external reforming (c),(d) cathode off-gas → external reforming → cathode air heating (a),(c) fuel-steam mixture → cathode off-gas → engine exhaust (b),(d) fuel-steam mixture → engine exhaust → cathode off-gas	83
Figure 3.5 – System configuration for case study under variation of thermal energy supply for external reforming: (a) Case 1 (b) Case 2 (c) Case 3	87
Figure 4.1 – Assumptions for system-level analysis and limitations on the feasible operation: (1)–(10) assumptions (a)–(c) feasible operating conditions (limitations on the feasible operating range)	92
Figure 4.2 – Experimental apparatus: (a) Yamaha MZ 300 (b) Exhaust analyzer (MK 9000)	94
Figure 4.3 – Algorithm for the integration of engine experimental result and simulation model of fuel cell and BOPs.....	100
Figure 4.4 – Operating parameters of the SOFC-SAI engine hybrid system designed in Chapter 3	103
Figure 4.5 – Parameters affecting the engine intake condition	105
Figure 4.6 – Engine intake condition in experiment: (a) anode off-gas composition under variation of fuel utilization (b) intake temperature [°C] (c) available thermal energy of anode off-gas [kW]	107
Figure 4.7 – Combustion characteristics: (a) spark timing for maximum work [CAD aTDC] (b) COV(NMEP) [%] (c) time required for initial flame development (CA10–spark timing) [CAD] (d) CA10 [CAD aTDC] (e) combustion duration (CA90–CA10) [CAD].....	108

Figure 4.8 – Normalized net heat release rate profile from experimental data: (a) in the case that fuel utilization in fuel cell is 70% (b) in the case that fuel utilization in fuel cell is 80%.....	110
Figure 4.9 – Performance of engine: (a) net indicated work [kW] (b) NMEP [bar] (c) heat loss fraction based on LHV of anode off-gas [-] (d) thermal efficiency [%].	113
Figure 4.10 – Emissions: (a) CO emission corrected to 15% O ₂ [ppm-dry] (b) H ₂ emission corrected to 15% O ₂ [ppm-dry] (c) CO emissions and combustion stability (COV).....	115
Figure 4.11 – Estimation accuracy of exhaust gas composition using emission measurement (CO and H ₂)	116
Figure 4.12 – Combustion efficiency estimated by exhaust measurement: (a) CO burned fraction [-] (b) H ₂ burned fraction [-] (c) combustion efficiency [%]	118
Figure 4.13 – Heat transfer quality of exhaust gas: (a) exhaust temperature [°C] (b) temperature increase through catalytic oxidizer [°C] (c) temperature after catalytic oxidizer [°C] (d) available thermal energy of exhaust [kW].....	120
Figure 4.14 – System efficiency under effectiveness variation of external reformer 1 and 3: (a) system efficiency [%] (b) effectiveness of HEX 2 for steam generation [-] (c) effectiveness of HEX 3 for cathode air heating [-]	123
Figure 4.15 – Fuel cell operation under effectiveness variation of external reformer 1 and 3: (a) overall external reforming rate (methane conversion rate) [%] (b) cell voltage [V] (c) inlet temperature of fuel cell [°C].....	125
Figure 4.16 – Heat-supply used for external reforming under variation of fuel utilization and equivalence ratio: (a) external reformer 1 using engine exhaust heat [kW] (b) external reformer 2 using anode off-gas heat [kW] (c) external reformer 3 using cathode off-gas heat [kW]	127
Figure 4.17 – Fuel cell performance under variation of fuel utilization and equivalence ratio: (a) H ₂ mole fraction in the anode inlet gas on a wet basis [%] (b) cell voltage [V] (c) heat transfer from fuel cell to the environment for satisfying the operating temperature [kW]	129
Figure 4.18 – System performance under variation of fuel utilization and equivalence ratio: (a) fuel cell power [kW] (b) thermal efficiency of fuel cell [%] (c) hybrid system power [kW] (d) hybrid system efficiency [%]	131
Figure 4.19 – Heat-supply used for external reforming under variation of fuel utilization and air utilization: (a) external reformer 1 using engine exhaust heat [kW] (b) external reformer 2 using anode off-gas heat [kW] (c) external reformer 3 using	

cathode off-gas heat [kW]	133
Figure 4.20 – Fuel cell performance under variation of fuel utilization and air utilization: (a) H ₂ mole fraction in the anode inlet gas on a wet basis [%] (b) cell voltage [V] (c) heat transfer from fuel cell to the environment for satisfying the operating temperature [kW]	135
Figure 4.21 – System performance under variation of fuel utilization and air utilization: (a) fuel cell power [kW] (b) thermal efficiency of fuel cell [%] (c) hybrid system power [kW] (d) hybrid system efficiency [%]	137
Figure 5.1 – Multi-level and full factorial design.....	140
Figure 5.2 – Response surface and constraint surfaces of the hybrid system: (a) accuracy of the response surface for hybrid system efficiency (b) feasible region from the observation data for the combustion stability and thermal self-sustainable operation maintaining the design operating temperature (c) response surface and constraint surfaces in the case that fuel utilization is 75%.....	143
Figure 5.3 – Optimization results under the variation of fuel utilization: (a) optimal operating condition of air utilization and equivalence ratio (b) power generation of the fuel cell and the engine at optimal condition.....	144
Figure 5.4 – BOP operation under optimal operating conditions: (a) heat-supply for the external reforming (b) reforming proportion of each external reformer and external reforming rate (c) heat-supply proportion of each BOP for the steam generation and the cathode air heating.....	147
Figure 5.5 – Power generation share of engine in the hybrid system.....	155
Figure A.1 – Configuration of the fuel cell model	169
Figure A.2 – Calculation of heat distribution in the fuel cell	170
Figure B.1 – In-cylinder pressure and temperature profile over crank angle; in the case of the experimental results in Section 4.3	173
Figure B.2 – Validation result of the modeling for synthesis gas ignition delay calculation; with experimental results from previous studies ((1):[57] (2):[58] (3):[59]).....	173

List of Tables

Table 2.1 – Specification of a single-cylinder engine: Honda GX 390	21
Table 2.2 – Stack experimental data for validation of the fuel cell model [32].....	27
Table 2.3 – Operating conditions for the fuel cell model and the engine experiment	40
Table 2.4 – Comparison of the averaged-cycle performance between the HCCI and SAI engine.....	50
Table 3.1 – Case study for thermal energy distribution of anode/cathode off-gas for BOP operation	79
Table 4.1 – Specifications of a single-cylinder engine: Yamaha MZ 300	94
Table 4.2 – Parameter variation range and reference condition.....	102
Table 5.1 – Variable selection for response surface and optimization	141
Table 5.2 – Optimization result: design point for the hybrid system.....	151
Table 5.3 – Performance of the hybrid system at the design point (optimal operation)	152
Table A.1 – Specifications of the fuel cell model	164
Table C.1 – Stream properties of the SOFC–SAI engine hybrid system at the operating condition achieving the efficiency of ~61.6% (in Chapter 2)	174
Table D.1 – Response surface model by multiple linear regression through least squares method.....	175
Table E.1 – Stream properties of the SOFC–SAI engine hybrid system at the optimal operation (in Chapter 5)	176

Nomenclature

b	least squares estimator	P_c	pressure at critical point [atm]
C	heat capacity [J K ⁻¹]	P^o	pressure at stand reference state = 1 atm (= 101.325 kPa)
c	specific heat [J kg ⁻¹ K ⁻¹]	p	partial pressure [Pa]
D	diffusivity [m ² s ⁻¹]	Q	heat [J]
E	energy [J]	q	heat [J kg ⁻¹]
e	electron	R_u	universal gas constant [8.3145 J mol ⁻¹ K ⁻¹]
F	Faraday constant [96,485 C mol ⁻¹]	r	pore radius [μm]
H	enthalpy [J]	T	temperature [K]
h	enthalpy [J kg ⁻¹]	T_c	temperature at critical point [K]
i	current [A]	t	time [s]
j	current density [A m ⁻²]	U	internal energy [J]
j_0	exchange current density [A m ⁻²]	u	internal energy [J kg ⁻¹]
k	number of regression variables	V	volume [m ³] or voltage [V]
K_p	equilibrium constant	W	work [J]
MW	molecular weight [kg kmol ⁻¹]	X	exergy [J] or matrix of regressor variables
m	mass [kg]	x	mole fraction or quality of steam or regressor variables
\dot{N}	mole flow rate [mol s ⁻¹]	y	observation data
n	mole [mol]		
n_{cell}	number of cells		
n_e	electrons transferred		
P	pressure [Pa] (1 bar = 100 kPa)		
<u>Greek letter</u>			
γ	specific heat ratio	η_{burn}	burned fraction
γ	coefficients for exchange current density [A m ⁻²]	θ	crank angle degree [CAD]
δ	thickness [μm]	ρ	resistivity [Ω m]
ε	porosity [%] or effectiveness or error	σ	standard deviation
η	efficiency	τ	tortuosity
		τ_{id}	ignition delay [s]

Superscripts and subscripts

<i>act</i>	activation	<i>h</i>	hot gas
<i>an</i>	anode	<i>in</i>	inlet
<i>atm</i>	atmosphere	<i>int</i>	interconnection
<i>avg</i>	averaged	<i>K</i>	Knudsen
<i>C</i>	carbon	<i>n</i>	net
<i>c</i>	cylinder or cold gas	<i>o</i>	start of combustion
<i>cv</i>	control volume	<i>ohm</i>	ohmic
<i>ca</i>	cathode	<i>out</i>	outlet
<i>con</i>	concentration	<i>rfm</i>	reformer
<i>des</i>	destruction	<i>sys</i>	system
<i>eff</i>	effective	<i>T</i>	temperature
<i>el</i>	electrolyte	<i>u</i>	unburned gas

Abbreviations

<i>aBDC</i>	after bottom dead center	<i>LHV</i>	lower heating value [J kg ⁻¹]
<i>aTDC</i>	after top dead center	<i>RFM</i>	reformer or reforming
<i>bTDC</i>	before top dead center	<i>SMR</i>	steam methane reforming
<i>CAD</i>	crank angle degree	<i>Util</i>	utilization
<i>COV</i>	coefficient of variation [%]	<i>WGSR</i>	water-gas shift reaction
<i>ER</i>	external reformer	<i>%p</i>	percentage point
<i>HEX</i>	heat exchanger		

Chapter 1. Introduction

1.1. Combined cycle of SOFC

At present, there is a growing need to develop new energy conversion methods in preparation for the depletion of fossil fuels and increasingly stringent global environmental regulations [1-4], and natural gas production and demand are expected to increase in response to enhanced global environmental regulations and its low prices, as shown in Figure 1.1 [5]. Fuel cells, which directly convert chemical energy into electricity, are a promising technology because of their efficiency and emission characteristics [6]. In particular, solid oxide fuel cell (SOFC) has high efficiency, a nonprecious metal catalyst and fuel flexibility, i.e., capability of using natural gas or other hydrocarbon as fuel through internal reforming, because its operating temperature is as high as 750°C [6].

In general, anode off-gas has unused fuel because of the fuel utilization limitation for the performance at the anode [7]. Thus, a typical SOFC stand-alone system has the unused fuel oxidized using a catalytic combustor and only recovers the waste-heat for thermally self-sustainable operation [8].

Hence, high operating temperature fuel cells, such as SOFC or molten carbonate fuel cell (MCFC), have been studied for hybridization with other power generation systems, in order to convert the residual chemical energy of anode off-gas into additional power for improved efficiency. In particular, many researchers have studied large-scale (MW) fuel cell–gas turbine (GT) hybrid systems [9], e.g., in terms of combined cycle type, operating conditions [10] and

economic analysis [11]. However, in sub-megawatts range for distributed generation, an internal combustion engine (ICE) also has high electrical efficiency and economic feasibility when hybridized with SOFC, as shown in Figure 1.2 [12]. Nevertheless, there are few studies focused on hybridization with the engine, which is a well-known device and superior in terms of maintenance, purchase cost and operation stability [8, 13].

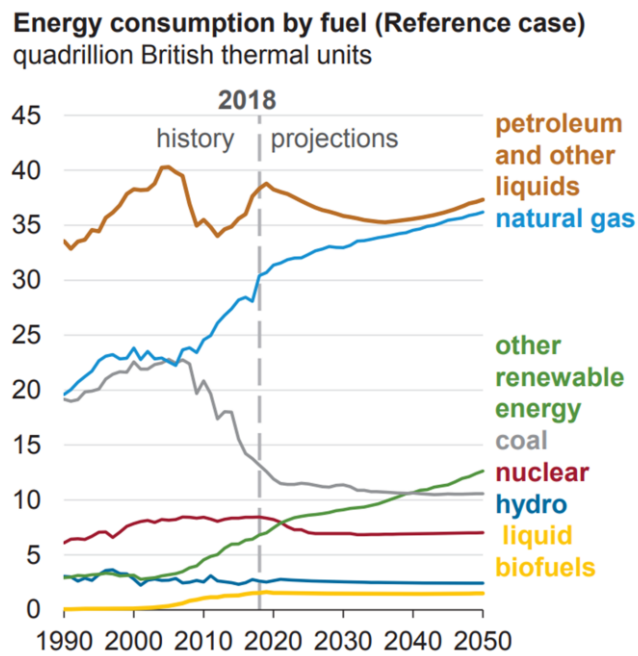


Figure 1.1 – Increase in natural gas demand (consumption) [5]

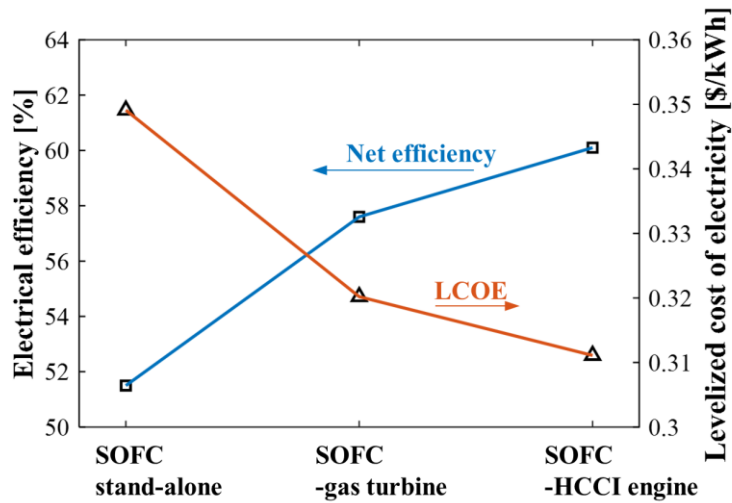


Figure 1.2 – Electric efficiency and LCOE: SOFC stand-alone, SOFC-GT hybrid system and SOFC-HCCI engine hybrid system; re-produced from [12]

1.2. SOFC-ICE hybrid system

For the SOFC–ICE hybrid system, several combustion strategies have been studied, such as homogeneous charge compression ignition (HCCI) [8, 12-17] and reactivity-controlled compression ignition (RCCI) [18].

In the case of the SOFC–HCCI engine hybrid system, various approaches have been conducted. Economic feasibility mentioned above has been confirmed based on thermo-economic analysis [8, 12, 13, 16], and dynamic model has been developed for the optimal control strategy and dynamic behavior, e.g., load transition, has been investigated through the model [15]. In addition, HCCI engine performance in the hybrid system based on methane as fuel has been also

studied through a single-cylinder engine experiment with variation of operating conditions such as varying fuel utilization [14]. It has been confirmed that HCCI engine can combust anode off-gas successfully, which has many diluent gases up to 70–80%, e.g., H₂O and CO₂. In general, the HCCI engine has the advantages of high efficiency, lean-burn and low emission of NO_x. Recently, SOFC-HCCI engine hybrid system has been analyzed which is coupled with metal hydride for hydrogen addition into the HCCI engine that contributes to increase in the overall system efficiency, but the engine performance has been investigated by the simplified engine model developed as the Otto-cycle without the actual engine experiments [17].

However, the HCCI engine has some important issues. It is difficult to control the combustion timing because it has no direct ignition input and the combustion occurs by auto-ignition, which is considerably sensitive to the intake temperature [19]. In addition, sufficiently high intake temperature is required for the anode off-gas composition [14]. If not properly operated, a misfire or partial-burn in the engine may cause disturbance in the hybrid system operation. Finally, because of the HCCI load limitation by pressure rise rate at high load or instability at low load, there could be difficulties in coping with large variation of the fuel utilization in the fuel cell stack, i.e., off-design operation [20-23].

There has been a modeling approach of developing SOFC–RCCI engine hybrid system. Fuel cell system model was developed in combination of engine combustion model validated by the RCCI engine experiment and system-level approach has been conducted for the performance evaluation of the hybrid system based on C₇H₁₆ as surrogate fuel of diesel [18]. To find optimal operating conditions, design of experiments of simulation and genetic algorithm was used.

As a result, it was predicted that the system may achieve ~70% efficiency at MW power generation level.

However, the RCCI engine still has the similar issues of combustion stability, control and pressure rise rate despite its slight advantage over HCCI [18]. In addition, the aforementioned study adopted diesel, or high reactivity fuel, as an ignition source, which may require additional supply of such fuel in the field operation, sometime not being practical. On the other hand, if natural gas is adopted for the SOFC–RCCI engine hybrid system, the RCCI engine using natural gas as ignition input may be not favorable for the operating performance compared to diesel, due to its low reactivity, gaseous compression work and difficulty in selecting injector for high-pressure direct injection.

1.3. Optimization of SOFC hybrid system

In the previous studies, optimization of operating conditions has been conducted for SOFC hybrid system. Yi et al. [24] investigated the optimal fuel utilization and pressure ratio of SOFC-GT combined cycle through parametric analysis by using system modeling. It was confirmed that optimal fuel utilization of SOFC combined cycle is always lower than SOFC stand-alone system. Gandiglio et al. [11] investigated the effect of operating pressure on the SOFC-GT cycle with heat recovery steam cycle, based on thermo-economic analysis, and it is confirmed that the levelized cost of electricity (LCOE) of the pressurized cycle is lower than that of the atmospheric one without GT. In addition, Rokni [25] proposed SOFC-Stirling hybrid system using alternative fuels such as natural gas, ammonia, di-methyl ether (DME), methanol and ethanol. The author investigated the effect of fuel utilization, fuel cell operating temperature and fuel type on the hybrid system efficiency through simulation modeling.

However, there has been few studies focused on the optimization of operating conditions for SOFC-ICE hybrid system. Chauhy et al. [18] investigated the optimal operating condition for SOFC-RCCI engine hybrid system through system modeling that engine and fuel cell were validated with experimental data. The objective function was system efficiency, and constraints for engine and fuel cell such as peak pressure, peak pressure rise rate and temperature rise in cathode were considered for the optimization. They obtained the optimum through genetic algorithm, such as engine intake temperature, fraction of anode off-gas re-circulation, fuel utilization, fuel bypass for RCCI, excess air ratio (air utilization) and compressor outlet pressure. The variables are related to the reaction in the fuel cell and the engine, i.e., electrochemical reaction and

combustion reaction.

In addition, Park et al. [26] conducted comparative study for optimized layout design of SOFC–combined heat and power system. The authors investigated 14 potential system layout designs through T-Q diagram analysis, and 4 effective layouts were analyzed through further detailed thermodynamic perspectives. Finally, the authors selected one layout for the optimal thermal integration, which combusts directly the mixed gas of anode/cathode off-gas in afterburner and uses branching of the exhaust gas, but it has not been confirmed that this layout is appropriate for the hybrid system such as SOFC-GT or SOFC-ICE system.

Most studies focused on optimization of operating conditions have been performed for a given configuration. Especially, in the case of SOFC-ICE hybrid system, optimization or comparative evaluation for system configuration design has not been performed in previous studies, although optimal configuration design is significant to maintain the high operating temperature of SOFC hybrid system which consists of hot BOPs. Furthermore, most studies have been conducted based on simulation modeling of the additional energy conversion device, i.e., ICE, despite anode off-gas is not typical fuel for the devices. For the reliable optimization of SOFC-ICE engine hybrid system, it is necessary to investigate the effect of optimization parameters on the engine operating characteristics through actual experiments. Hence, for the most efficient SOFC-ICE hybrid system operation, it is important to find the optimal system configuration and optimize operating conditions with actual engine experiments for all the operable conditions.

1.4. Research motivation and objectives

Spark ignition (SI), compression ignition (CI), HCCI and RCCI are currently available combustion strategies developed for ICE operation. As mentioned earlier, HCCI and RCCI were investigated in SOFC-ICE hybrid system, and they had some challenges to overcome to be practically applied, even though they showed relatively high potential in conversion efficiency. The conventional CI engine uses a direct ignition input which is direct injection of compressed liquid fuel into cylinder. If CI is adopted as the combustion strategy of anode off-gas, it should be compressed before direct injection. However, the anode off-gas is a gaseous fuel with much diluent, which would require significant compression work. Hence, CI is neither practical for the combustion strategy of the anode off-gas.

Hence, it is necessary to investigate the feasibility of the spark-assisted ignition (SAI) engine in the SOFC-ICE hybrid system, although the composition of anode off-gas is unfavorable to flame propagation owing to much dilution. However, it still has some advantages over the operating condition of general gasoline-fueled spark ignition (SI) engine, in terms of overall higher intake temperature and the main component of the fuel, hydrogen. Additionally, if the spark ignition can be successfully applied, this new combustion strategy has the possibility to ignite the intake mixture stably at relatively lower intake temperature than required in HCCI, since the latter depends purely on the chemical reaction kinetics of the highly-diluted fuel. Finally, due to the relatively high intake temperature, it is also expected that the initial flame propagation by spark ignition might lead to the auto-ignition of the unburned mixture, i.e., inducing HCCI-like combustion. In literatures, it is sometimes referred to as

spark-assisted HCCI. Consequently, a novel SOFC–ICE hybrid system using spark-assisted ignition is developed and investigated, for the first time in this study.

For the newly proposed SAI engine operation in an SOFC–ICE hybrid system, it is important to understand the combustion controllability and performance of the engine and its effect on the fuel cell system, especially the potential of better using thermal energy of the anode off-gas by lowering the engine intake temperature. Thus, in this study, the feasibility of the SAI engine is confirmed directly through the engine experiments, considering the combustion stability, power, emission characteristics and available thermal energy of the engine exhaust and the anode off-gas, with the intake temperature variation. Furthermore, the system-level analysis is important because the available thermal energy should be supplied to balance of plants (BOPs) for the system operation. Finally, the operating characteristics of the SOFC–SAI engine hybrid system, such as efficiency, thermal self-sustainability and exergy destruction, are analyzed through the system-level analysis integrating the SAI engine experimental results and simulation model for fuel cell and BOPs developed in this study.

Furthermore, this is the first study where we provide a systematic approach to design the optimal system configuration of SOFC–ICE hybrid system for the most efficient heat distribution, and then optimize operating conditions to maximize system efficiency. In SOFC–SAI engine hybrid system based on natural gas, thermal energy in the system should be distributed efficiently at optimal operating condition for thermally self-sustainable operation and improved system efficiency, since the heat source is essential to perform steam

generation, external reforming and cathode air heating for proper system operation. If not, the fuel cell operating temperature decreases, or supplementary heat supply should be required for the BOPs operation, and it leads to decrease in the system efficiency.

Hence, the novel system configuration of SOFC-SAI engine hybrid system is designed to distribute thermal energy of anode/cathode off-gas efficiently to BOPs operation. It is conducted through case study and parametric study under variation of BOP configuration, considering all the possible cases of heat distribution and heat transfer quality, i.e., temperature gradient and heat capacity of the heat exchanging streams.

In the end, operating conditions related to SOFC and SAI engine are optimized at the designed configuration. Fuel utilization, air utilization and equivalence ratio affecting electrochemical reaction in the fuel cell and combustion reaction in the engine are considerably important factors for understanding the operating characteristics of the system. Thus, parametric study is performed under variation of the operating conditions. Furthermore, based on the understanding, it is optimized to achieve the most efficient operation of the newly designed SOFC–SAI engine hybrid system. For an optimization scheme, design of experiment and response surface method are used under consideration of some constraints related to stable and sustainable operation. The performance of BOPs required to achieve the optimal operation is also investigated through the response surface.

1.5. Summary

ICE using SAI in the SOFC hybrid system is aimed to convert the residual chemical energy in the anode off-gas into additional power in order to improve the overall system efficiency. The main objective of this study is to develop a novel SOFC-ICE hybrid system which is capable of achieving the most stable and efficient operation. The details are summarized as the following.

Firstly, a new combustion concept for the hybrid system, i.e., spark-assisted ignition, is introduced to achieve stability and controllability of the combustion and reduce the thermal energy of anode off-gas required for the combustion. It is important to reduce the energy consumption in the engine while generating the additional power, since the off-gas energy also should be used for BOPs operation. It means that exergy efficiency is a significant indicator of the engine operation in the hybrid system. Secondly, the system configuration is newly designed for the efficient thermal energy distribution of anode/cathode off-gas. BOPs should be operated to increase the cell voltage and maintain the operating temperature of the stack. Finally, the operating conditions related to the electrochemical and combustion reaction are optimized for the most efficient operation of the SOFC-SAI engine hybrid system considering the operability of the fuel cell and the engine.

The main body consists of five chapters. In Chapter 2, the feasibility and the effect of SAI engine on the hybrid system are investigated. Methodology for system-level analysis is also provided including the descriptions of engine experiment and simulation model for fuel cell and BOPs. In Chapter 3, the details for the system design are described. In Chapter 4, parametric study results are provided. The most desirable configuration of the hybrid system is selected in

this Chapter. The effect of fuel utilization, air utilization and equivalence ratio on the hybrid system is also discussed. In Chapter 5, based on the understanding in Chapter 4, optimization results are discussed. Finally, the summary and conclusions of this study are discussed in Chapter 6. In Appendices, additional details are provided such as fuel cell modeling, response surface of the hybrid system and stream properties at optimal operation.

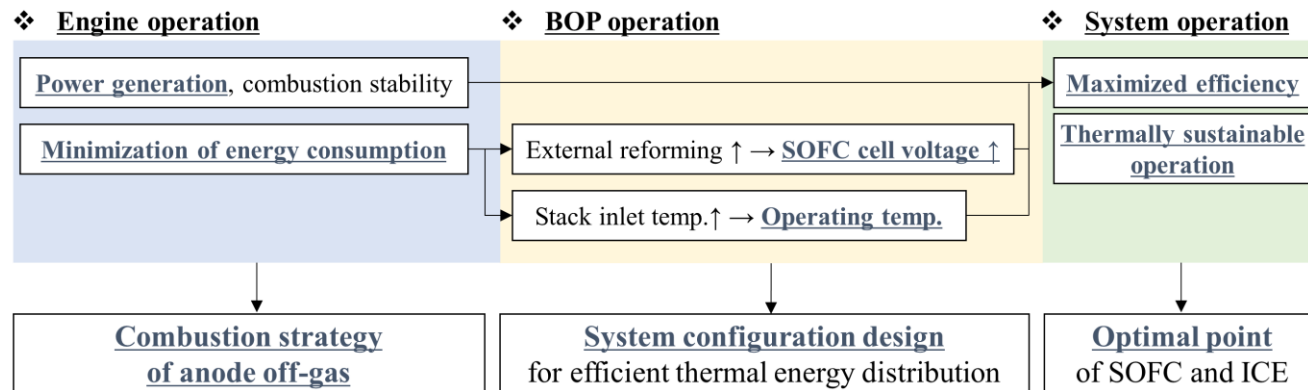
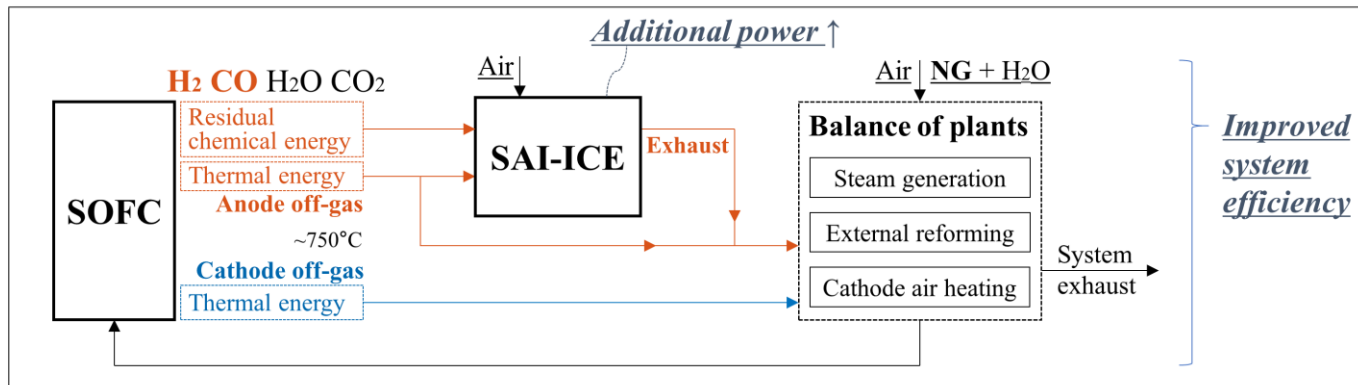


Figure 1.3 – Research motivation and objectives: combustion strategy, system design and optimization of SOFC–ICE hybrid system

Chapter 2. Feasibility of spark-assisted ignition engine in SOFC-ICE hybrid system

2.1. Research methodology

The SOFC–SAI engine hybrid system consists of a fuel cell, an engine, external reformers, heat exchangers, a catalytic oxidizer and mixers. In this study, the operating performance of the engine, which is the key understanding in the newly proposed hybrid system, was measured through actual experiments. For the simulated experiments, intake gas conditions for the engine experiment were calculated based on the simulation system model. Here, the system model includes all the components of the hybrid system, except the engine. The simulation model of the fuel cell and external reformers was validated with the representative experimental results. Finally, operating characteristics of the full hybrid system were analyzed by integrating the engine experiment results with the simulation model.

2.1.1. System configuration

The hybrid system configuration, including BOPs, is shown in Figure 2.1. Methane, the main component of natural gas, is used as system fuel. Although the SOFC has fuel flexibility, external reforming is also necessary to prevent a large thermal gradient in the stack by the endothermic reforming reaction, carbon deposit and other durability issues [15, 27]. Furthermore, it is desirable to increase overall H₂ fraction in anode channel in order to improve the cell voltage which results in increase of the SOFC power. For the high H₂ yields, it is

necessary to increase the extent of the external reforming by the efficient thermal energy distribution, and to supply the externally reformed gas into the stack. Thus, steam-methane reforming (SMR) is adopted for external reforming that has high hydrogen yield [28]. The engine exhaust heat is supplied to external reformer 1 and the thermal energy of anode off-gas is supplied to external reformer 2. As a result, steam-methane mixture is reformed in two steps. The partially reformed gas enters the anode, and the anode off-gas has many diluent gases, e.g., H₂O and CO₂, because of electrochemical reaction. In addition, it has also many diluents, if high steam-carbon ratio (S/C ratio) is required for preventing from carbon coking [29-31].

As mentioned earlier, we adopted spark-assisted ignition engine for combusting such diluted gas. The combustion phenomena are expected to include full flame propagation (i.e., conventional SI), flame propagation and induced auto-ignition (i.e., spark-assisted HCCI), and pure HCCI, depending on the thermodynamic state of the intake mixture, such as temperature and composition. The detailed discussion will be presented in Section 2.3.4. Considering the high temperature anode off-gas which is the intake gas of the engine and ensuring sufficient exhaust enthalpy out of the engine, the compression ratio is selected as typical spark ignition (SI) engine level, which is lower than the typical HCCI counterpart (11~13) [4]. This relatively low compression ratio also enables the whole range of the aforementioned combustion strategies in a given engine, without abnormal combustion such as knocking. Details for the engine specifications are described in Section 2.1.2.

In the hybrid system, additional work is extracted from chemical/thermal energy of anode off-gas, which is only used for the BOP operation in the case of

a SOFC stand-alone system. Thus, the energy consumption in the engine should be minimized while generating power, e.g., decrease in heat loss, and all the available thermal energy in the hybrid system should be used efficiently as much as possible, in order to maintain the operating performance of BOPs for steam generation, external reforming and cathode air heating. If not, thermally self-sustainable operation of the SOFC could not be achieved. In the perspective of the system operation, the thermal energy of the anode off-gas should be used as much as possible to take advantage of the highest temperature in the hybrid system, given that the temperature gradient is important for heat exchange. Thus, two external reformers are adopted for the hybrid system operation which uses thermal energy of the anode off-gas and the engine exhaust gas. It is aimed to improve efficiency and thermally self-sustainable operability of the hybrid system through two external reformers. Furthermore, the residual chemical energy in the engine exhaust, i.e., combustion inefficiency, should be used for the external reforming. Hence, the external reformer 2 and the assistant catalytic oxidizer, which are newly introduced in the hybrid system that are absent from the general stand-alone SOFC system, are significant components, and its operating characteristics are directly affected by the SAI operating performance.

In fact, it is difficult to achieve complete combustion with clean emissions in the present internal combustion engine, even at the conventional operating condition, i.e., gasoline or diesel. Hence, after-treatment system, which is appropriate for each fuel type and combustion strategy, is inevitably adopted for the emission reduction of the present internal combustion engine. In the SOFC–SAI engine hybrid system, the assistant catalytic oxidizer is adopted as an after-treatment component in order to convert the unburned fuel such as H_2 and CO

into the thermal energy.

Fresh air supplied to the cathode is heated by the cathode off-gas in heat exchanger 3 (HEX 3). To generate steam for SMR, thermal energy of the engine exhaust and cathode off-gas are used in heat exchangers (HEX 1–2), while water becomes super-heated vapor, i.e., steam.

In this study, the target power capacity of the SOFC–SAI engine hybrid system is about the 5-kW level, which is based on the availability of the commercial fuel cell stack and its validation data [32].

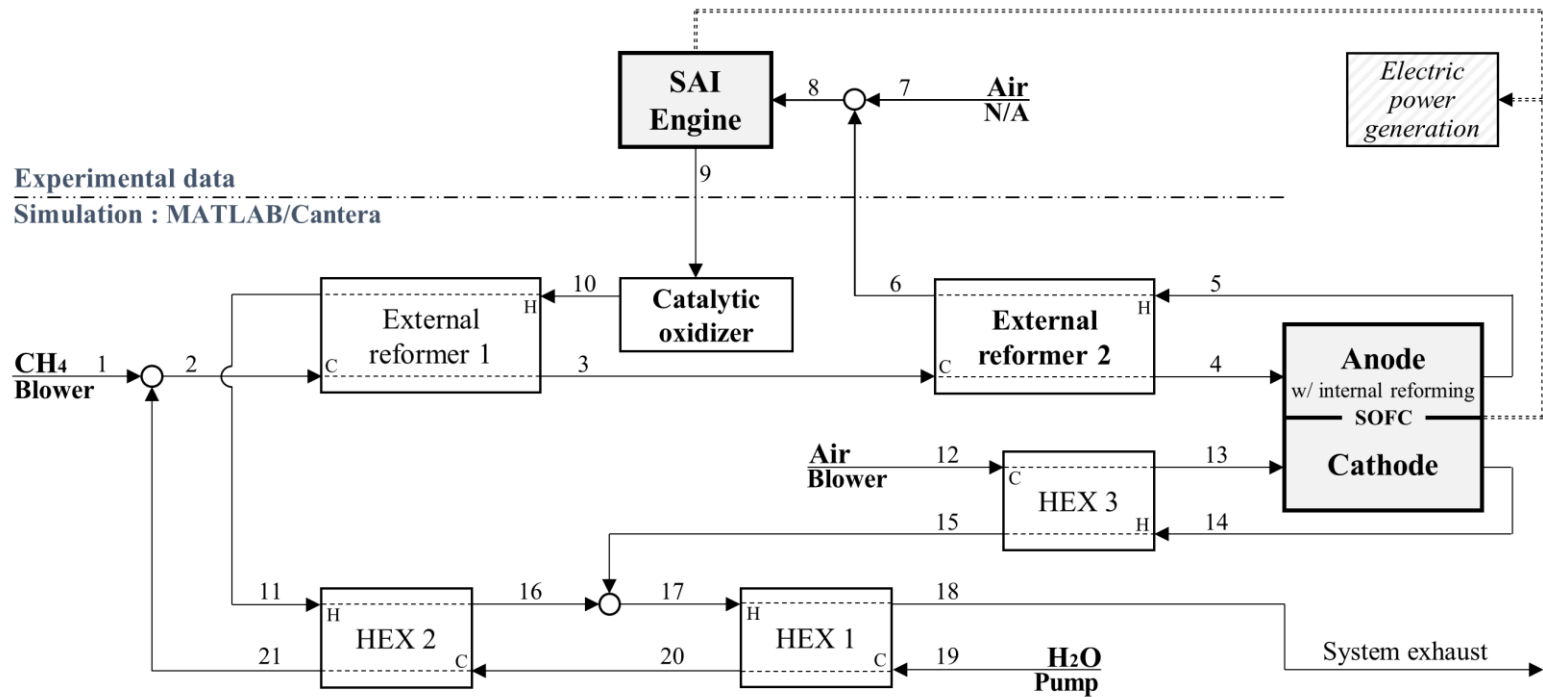


Figure 2.1 – Configuration of SOFC-SAI engine hybrid system

2.1.2. Engine experimental apparatus

A schematic diagram of the experimental setup for the engine is shown in Figure 2.2, which emulates composition, temperature and flow rate of intake gas in which anode off-gas and fresh air are mixed. A single-cylinder engine (Honda GX390) was used and detailed specifications are listed in Table 2.1. Mass flow controllers (Brooks and Bronkhorst) and a water pump (KNF) were used for flow rate control of each species. Naturally aspirated (N/A) air supply was used only for heating/cooling of a main heater. The 12-kW heater (Watlow) was used for temperature control of the intake gas. For the uniformity of intake gas, static mixer was used. Engine speed was controlled by motor/inverter (Higen). An encoder (Autonics) was connected to crank shaft for crank angle measurement. An in-house oil cooler was used to maintain the engine oil temperature within a certain range. The oil cooler circulates the engine oil in the crank case to the outside for cooling, and then supplies the cooled oil to the inside of the crank case again. A spark plug integrated in-cylinder pressure sensor (Kistler 6118BFD16) was mounted on the engine to measure in-cylinder pressure and generate a spark. Exhaust compositions such as O₂ and CO, as well as NO_x emissions, were measured by an exhaust analyzer (Greenline MK 2) on a dry basis. Data acquisition and equipment control were performed by MATLAB/Simulink and xPC target. For data processing of each experimental point, 150 consecutive steady-state cycles were used. The equipment for the engine experiment is shown in Figure 2.3–Figure 2.5.

Emulating intake gas

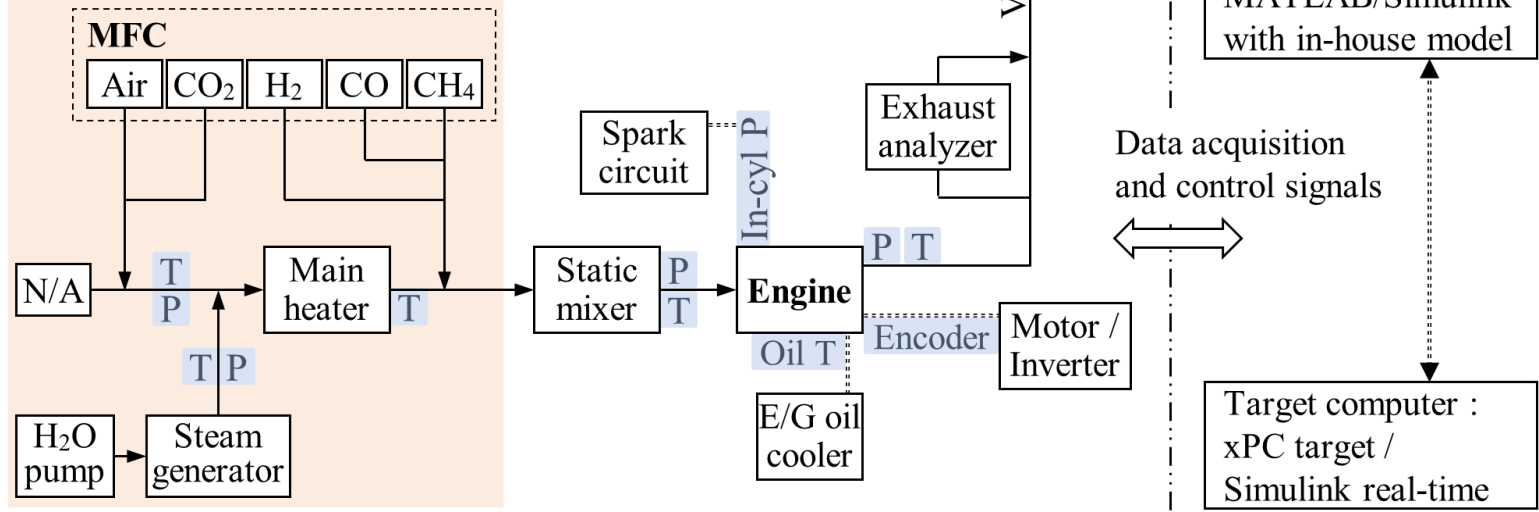


Figure 2.2 – Experimental apparatus: engine and peripherals

Table 2.1 – Specification of a single-cylinder engine: Honda GX 390

Honda GX 390	
Bore	88 mm
Stroke	64 mm
Compression ratio	8.2
Displacement	389 cc (cm ³)
Engine speed	1,800 RPM
Cooling system	air-cooled
Oil temperature	90 ± 5°C

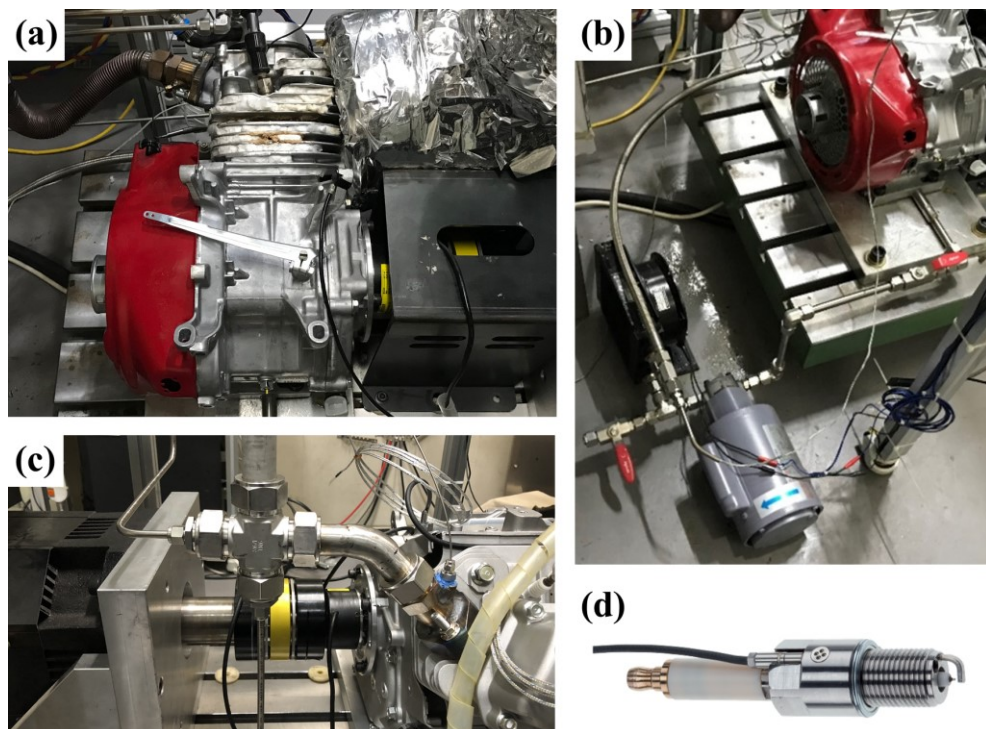


Figure 2.3 – Experimental apparatus:

(a) Engine (Honda GX 390) (b) In-house oil cooler (c) Encoder and coupling
(d) spark plug integrated in-cylinder pressure sensor (Kistler)

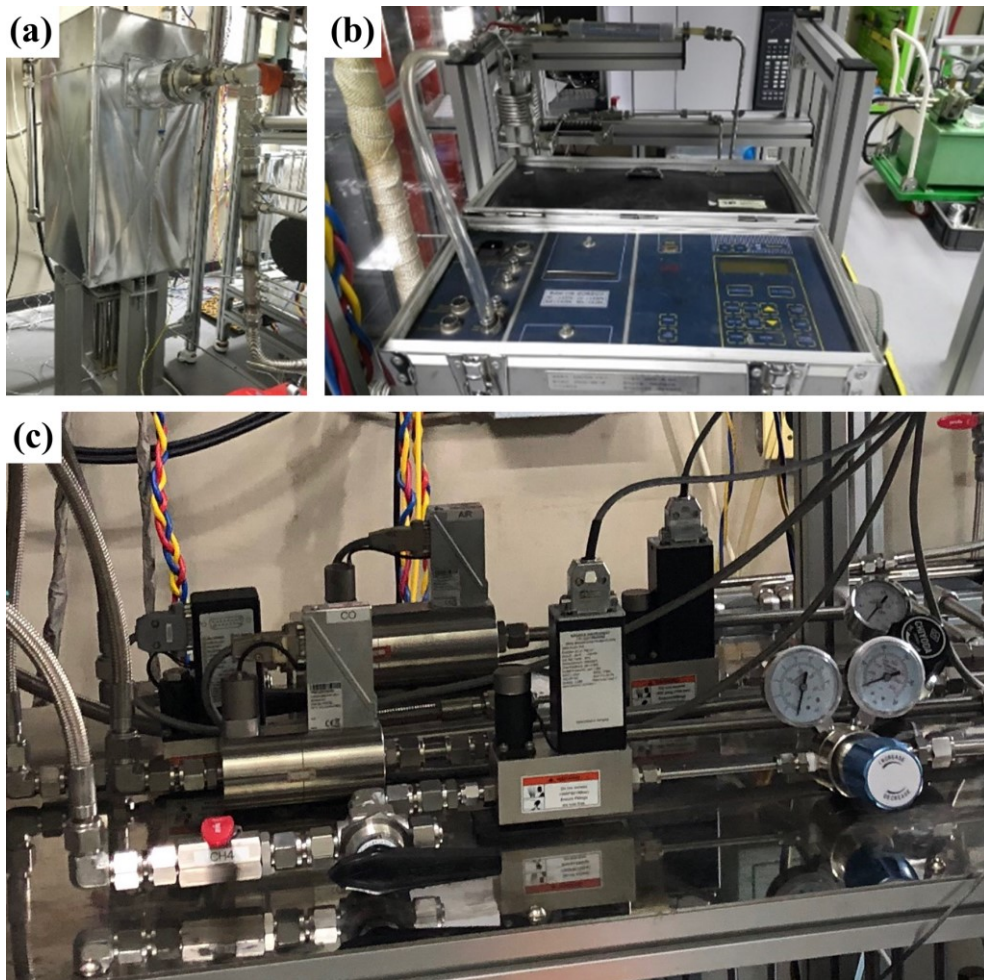


Figure 2.4 – Experimental apparatus:

(a) 12-kW heater (Watlow) (b) Exhaust analyzer (Greenline MK 2)

(c) Mass flow controller (Bronkhorst and Brooks)

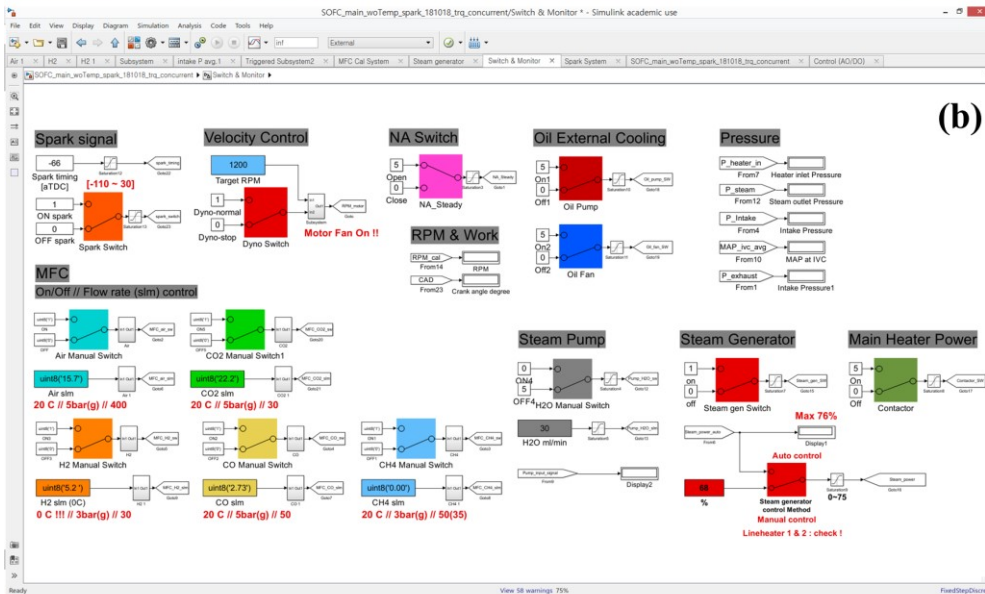
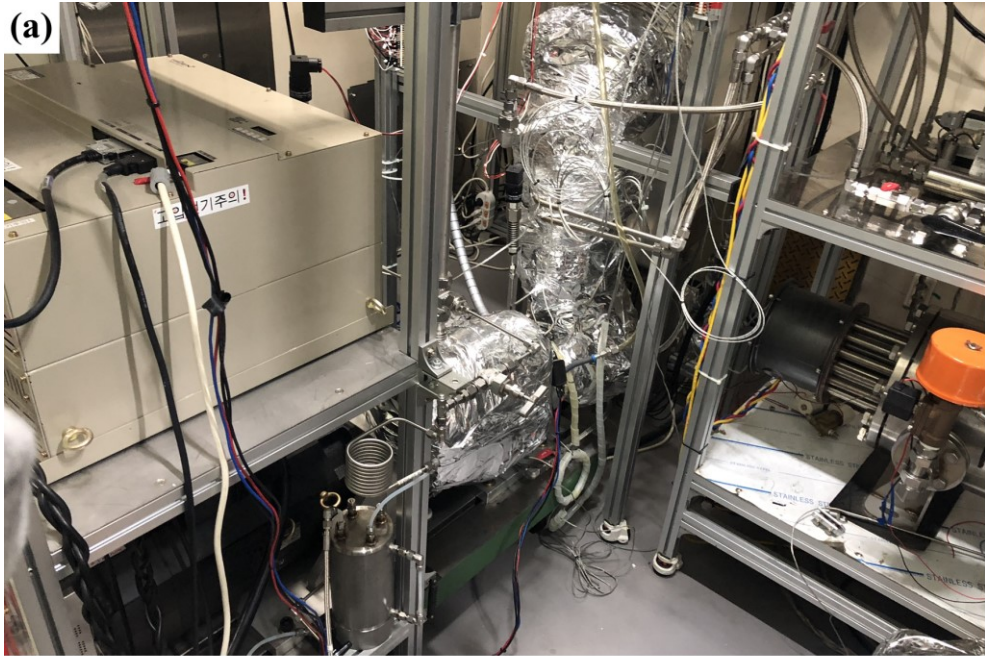


Figure 2.5 – Experimental apparatus:

(a) Engine experimental system (b) Simulink model for data acquisition and equipment control

2.1.3. Simulation model descriptions

The simulation model was developed by using MATLAB based on a steady and equilibrium-state and zero-dimensional equation for each component, i.e., fuel cell and BOPs. Cantera toolbox [33] and GRI 3.0 mechanism [34] were used for thermodynamic properties of methane and synthesis gas [35].

2.1.3.1. Fuel cell model

In this study, a zero-dimensional model was developed, because the main objective of the fuel cell model for this study is the prediction for off-gas composition, power generation trend, and thermal self-sustainability of the system at the design operating temperature and pressure. Thus, each anode and cathode is modeled as one control volume, and representative values are used for the calculation of thermodynamic properties in each control volume.

The major reactions in the fuel cell are electrochemical reaction (Eqs. (2.1)–(2.2)), steam-methane reforming reaction, i.e., internal reforming (Eq. (2.3)), and water-gas shift reaction (Eq. (2.4)). Thus, there are four unknown quantities for calculation of anode off-gas composition, i.e., the extent of each reaction.



The fuel cell is assumed to operate at the equilibrium-state of the given operating temperature and pressure in this model, i.e., isothermal and isobaric process, and it is operated at a given current demand, i.e., fuel utilization. Hence, the anode off-gas state can be determined by requirement for the transfer of the ionic charge carrier, i.e., oxygen ions, at the given current demand, even though the extent of each electrochemical reaction is not calculated in the zero-dimensional model. It means that the anode off-gas is in an equilibrium-state in which the Gibbs free energy is minimized with the oxygen ion transferred to the anode for satisfying the current demand. Consequently, the unique solution for the anode off-gas state can be obtained at the given current demand considering steam-methane reforming and water-gas shift reaction (WGSR), regardless of the reactivity of each electrochemical reaction. In this way, the anode off-gas state becomes a sole function of the design operating temperature, pressure and the current demand at given system fuel and S/C ratio. The equilibrium-state is calculated by using Cantera toolbox [33] in this study.

Although the extent of each electrochemical reaction is not calculated in this model, the electrochemical reaction of CO is generally negligible due to its slow reactivity compared to electrochemical reaction of H₂ and WGSR [36, 37]. Thus, it can be assumed that CO is only involved in WGSR. Even if the electrochemical reaction of CO is not negligible, the potential generated by each parallel electrochemical reaction is the same in a cell [38]. Hence, the fuel cell performance is calculated based on the H₂ in this model, considering Nernst voltage, activation loss, ohmic loss, concentration loss and heat transfer, after the state estimation of the off-gases at a given fuel and air utilization. The detailed descriptions of the fuel cell model are provided in Appendix A.

For the validation of the fuel cell model, the stack experimental results performed in the previous study [32] was used, which are listed in Table 2.2. The average temperature between anode/cathode outlet temperature was used as the operating temperature of each case under the validation process, since the temperature rise in anode/cathode channel is below $\sim 30^{\circ}\text{C}$. In cases 1 and 2, H_2 and N_2 were fed to anode path with varying air flow rate supplied to cathode. This was done to check the performance of fuel cell stack, i.e., i - V curve without internal reforming in the stack. In cases 3–6, CH_4 and H_2O (S/C ratio: ~ 3.2) were fed to the anode path. The mixture gas was partially reformed in an external reformer at the reformed gas temperature listed in Table 2.2, and internal reforming occurred inside the stack. The reformed gas temperature which was measured at the experiments means the extent of external reforming of the fuel-steam mixture, since it was confirmed in the previous study [2] that the shell-and-tube methane-steam reformer is capable of reforming the fuel-steam mixture to the equilibrium-state composition even at the low operating temperature. The anode inlet temperature listed in Table 2.2 is the actual inlet temperature of the partially reformed gas increased by an external heat source in order to operate the fuel cell at isothermal condition as much as possible. The fuel cell model is validated at the same operating conditions, e.g., the external reforming rate and the inlet temperature.

Table 2.2 – Stack experimental data for validation of the fuel cell model [32]

Case #			1	2	3	4	5	6
Anode	Flow rate before external reformer [mol/hr]	H ₂	139.20	139.20	–	–	–	–
		N ₂	139.20	139.20	–	–	–	–
		CH ₄	–	–	35.84	35.84	35.84	35.84
		H ₂ O	–	–	113.07	113.07	114.44	114.44
	Average temperature [°C]	Reformed gas	–	–	602	541	585	530
		Inlet	732	740	714	716	725	715
		Outlet	743	759	750	740	751	743
Cathode	Flow rate [mol/hr]	Air	685.29	835.19	835.19	792.37	835.19	685.29
	Average temperature [°C]	Inlet	739	743	732	722	737	725
		Outlet	746	766	752	744	756	745
Performance	Fuel cell load variation	Current [A]	2 → 55	55 → 65	33 → 50	50	40 → 50	43 → 68

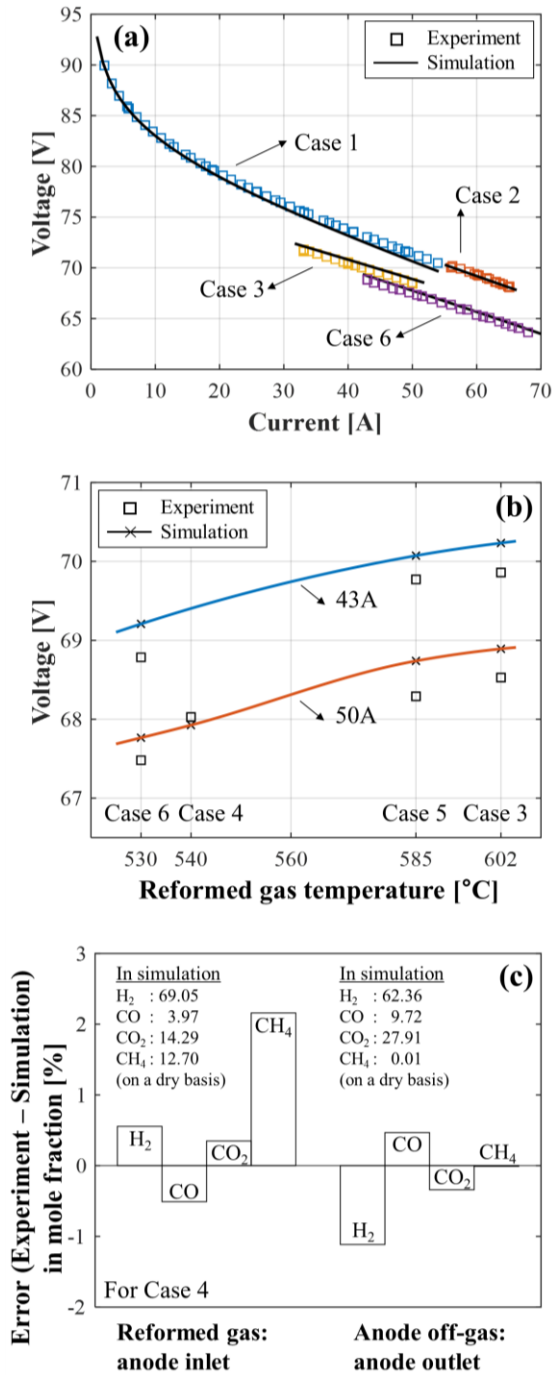


Figure 2.6 – SOFC model validation:

- (a) changes in load, fuel composition, reformed gas temperature and air flow rate
- (b) reformed gas temperature variation
- (c) estimation of anode in/outlet states

The results of the model validation with the actual stack performance are shown in Figure 2.6. The effects of load variation, air flow rate at cathode, reformed gas temperature and system fuel are included in the validation results. In particular, the effect of external reforming rate on the fuel cell performance is significantly important because the composition of inlet gas is affected by the change in external reforming rate due to the thermal energy distribution in the system. Hence, the model is validated with the reformed gas temperature variation, i.e., the external reforming rate variation, as shown in Figure 2.6(b) and validated with data measured by gas chromatography for each composition at the outlet of the external reformers and anode as shown in Figure 2.6(c). As a result, the validation results represent that the fuel cell model reliably predicts the anode off-gas composition and power.

2.1.3.2. BOP model

Each BOP is modeled as an adiabatic process, unlike the fuel cell model. Cantera toolbox [33] is used where the equilibrium-state calculation is required.

Heat exchangers are modeled as counter-flow, using the effectiveness method, and so are the external reformers. The effectiveness for heat transfer is represented as Eq. (2.5) [39].

$$\varepsilon = \frac{q_{HEX}}{\min(C_h, C_c) \cdot (T_{h,in} - T_{c,in})} \quad (2.5)$$

For the external reformers, the composition and temperature of the reformed gas are calculated under equilibrium-state after heat exchange, including the endothermic reforming reaction. The energy balance equation for cold fuel

stream to be reformed is represented in Eq. (2.6). The validation results of the external reformer modeling with experimental results from [2] are provided in Figure 2.7.

$$h_{RFM,in}(T_{c,in}, x_{steam-methane}) + q_{RFM} = h_{RFM,out}(T_{c,out}, x_{reformed\ gas}) \quad (2.6)$$

Catalytic oxidizer is modeled as being capable of oxidizing the fuel components of the exhaust gas under the isobaric and adiabatic process, considering equilibrium-state. The energy balance equation is represented in Eq. (2.7).

$$h_{Catalytic\ oxidizer,in}(T_{in}, x_{in}) = h_{Catalytic\ oxidizer,out}(T_{out}, x_{out}) \quad (2.7)$$

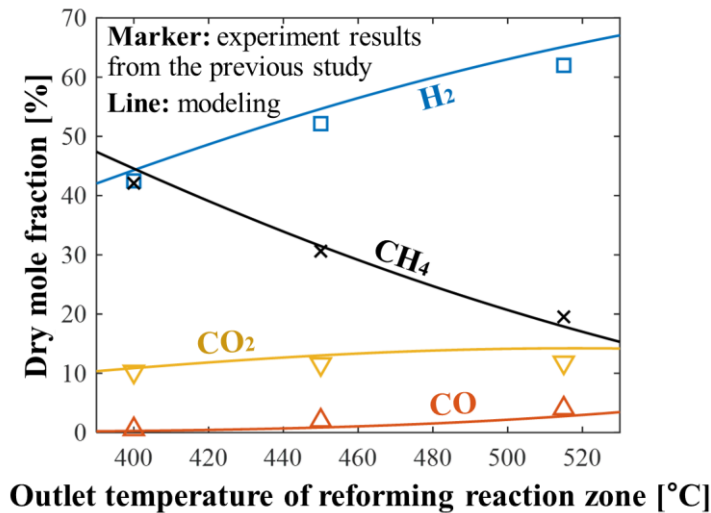


Figure 2.7 – External reformer model validation with experimental results from [2]: under variation of reformed gas temperature

2.1.4. Assumptions for the system-level analysis

The followings are the major assumptions introduced in the hybrid system analysis.

- 1) The pressure of all flow paths is 1 atm. There is no pressure drop considered.
- 2) The operating temperature of the fuel cell is fixed at 750°C, which is one representative temperature for the typical SOFC operation [6], as well as where the present fuel cell model is validated around (see Table 2.2 for cathode air temperature). Hence, heat transfer loss of the fuel cell, on the other hand, is calculated based on the first law of thermodynamics to meet this operating temperature requirement. ($T_5=T_{14}=750^{\circ}\text{C}$)
- 3) Heat losses (or heat transfer with environment) are only considered for the fuel cell and the engine. The actual heat loss of the engine operation is calculated based on the experiment.
- 4) The cathode inlet temperature is equal to the anode inlet temperature, for reducing thermal gradient inside the fuel cell. In the system simulation, the cathode inlet temperature is adjusted through HEX 3. ($T_4=T_{13}$)
- 5) The temperature after mixing of methane and steam is fixed at 150°C, considering the typical external reformer inlet temperature [40]. ($T_2=150^{\circ}\text{C}$)
- 6) For the heat exchange model, the upper limit of effectiveness is 0.85, considering the realistic operation. In the system simulation, the external reformer 2 has the maximum effectiveness as much as possible within the upper limit to use the available thermal energy of the anode off-gas. HEX 1 and HEX 2 are also to be as effective as possible within the upper limit to

generate enough steam that the mixture temperature after mixing with methane becomes 150°C (=T₂). However, there is additional constraint for the effectiveness of HEX 1 that the hot exhaust gas including vapor water (state 17) should not be cooled down below its dew point during heat exchange.

2.1.5. Integration of engine experimental results and simulation model for system-level analysis

For the analysis on the hybrid system performance, the iteration sequence integrating the engine experimental results and the simulation model of the fuel cell and BOPs is shown in Figure 2.8.

At given operating conditions such as fuel flow rate, S/C ratio, fuel and air utilization and operating temperature of the fuel cell, the information of the anode off-gas and cathode in/outlet gas such as temperature, composition and flow rate can be calculated first as described above. Based on this calculated anode off-gas composition and mass flow rate, engine experiment is conducted at various operating conditions such as equivalence ratio, intake temperature, spark timing, intake pressure, engine speed.

Steam-methane mixture (state 2) which is fixed by the assumption as described above and the engine exhaust after catalytic oxidizer (state 10) are used for calculation of external reformer 1 operation, and then external reformer 2 operation is calculated by using the anode off-gas (state 5) previously determined and the partially reformed gas through external reformer 1 (state 3). As a result, anode off-gas into the engine (state 6) and anode inlet gas (state 4) are determined.

If the calculated temperature (state 8) where the anode off-gas (state 6) and fresh air (state 7) are mixed at a given equivalence ratio is lower than the given intake temperature measured at the engine experiment, the external reformer 2 operation should be re-calculated considering the available thermal energy of anode off-gas, which is the maximum enthalpy difference that can be used before mixing with the fresh air while satisfying the given intake temperature and equivalence ratio.

Cathode inlet gas (state 13) and cathode off-gas (state 14) are determined by the assumptions that there is no inlet temperature difference, and the fuel cell operates at a given operating temperature as described above. Thus, HEX 3 operation and cathode off-gas after HEX 3 (state 15) are calculated using the information (state 12–14), and it is then used to generate steam. However, since HEX 1 and HEX 2 affect each other, the operation cannot be calculated at once. Thus, iteration process is necessary after initially setting the water state (state 20). The engine exhaust after external reformer 1 (state 11) and the initially assumed water state (state 20) are used for the calculation of HEX 2 operation, and then super-heated vapor (state 21) is determined. The engine exhaust after HEX 2 (state 16) and cathode off-gas after HEX 3 (state 15) are used for calculation of HEX 1 operation, and then the water state (state 20) is newly determined. If the previous value is equal to the updated value, the operation of HEX 1 and HEX 2 is determined and the iteration process finishes.

Then, it is checked whether the state of steam-methane mixture (state 2) after methane (state 1) and the super-heated vapor (state 21) are mixed satisfies the reformer inlet temperature requirement, i.e., 150°C as described above or not. If not, additional iteration is necessary until convergence. If steam-methane mixture

temperature (state 2) is lower than the required temperature at the first iteration, effectiveness for external reformer 1 is adjusted in a direction to reduce the heat-supply for the external reforming to generate enough super-heated vapor. In the opposite case, effectiveness for HEX 2 is adjusted in a direction to reduce the heat-supply for the steam generation. If the state of the steam-methane mixture (state 2) converges, all iteration process for the system analysis finishes, and then the fuel cell performance is calculated by using the information of anode in/outlet gas (state 4,5) and cathode in/outlet gas (state 13,14). Finally, all states and operation performance of the hybrid system are determined.

Operating conditions

Fuel cell: fuel flow rate, S/C ratio, fuel utilization, air utilization, operating temperature
Engine: equivalence ratio, intake temperature, intake pressure, spark timing, engine speed

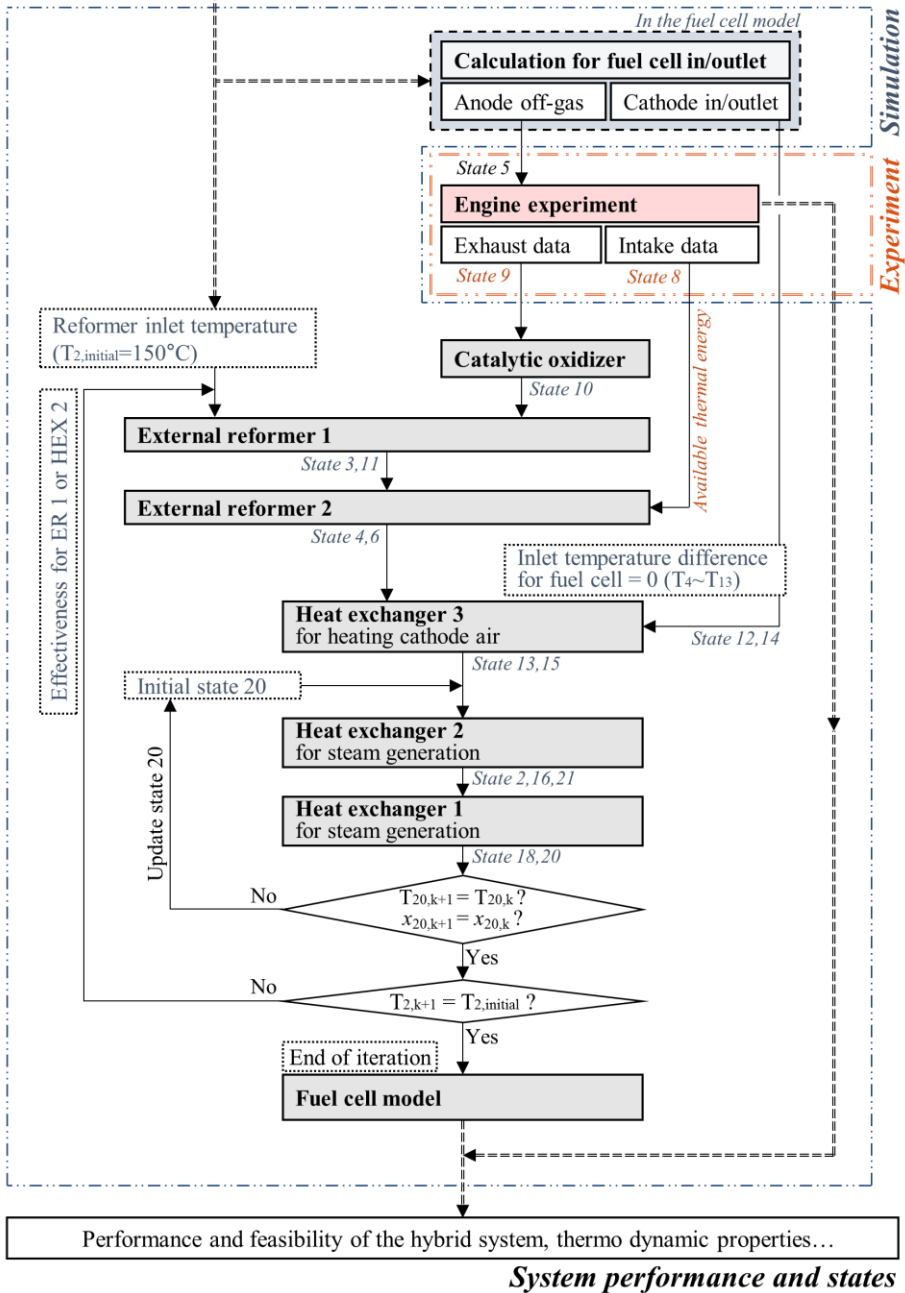


Figure 2.8 – Iteration sequence of system-level analysis on the hybrid system

2.2. Details for operating conditions of the hybrid system

2.2.1. Available control and geometric parameters

As shown in Figure 2.8, there are various available control parameters for the hybrid system. Fuel flow rate, S/C ratio and utilization of fuel and air are controllable for the fuel cell. The S/C ratio on the mole basis is described in Eq. (2.8). The fuel utilization of the anode is defined as Eq. (2.9), based on lower heating value (LHV) of reformed gas at the fuel cell operating temperature. The air utilization in the cathode is defined as the ratio of oxygen used in the supplied oxygen, as provided in Eq. (2.10).

$$S/C = \frac{\dot{N}_{H_2O}}{\dot{N}_{Fuel,C}} \quad (2.8)$$

$$\text{Fuel utilization of anode} = 1 - \frac{LHV_{an,out}}{LHV_{reformed\ gas\ @\ T_{Fuelcell}}} \quad (2.9)$$

$$\text{Air utilization of cathode} = \frac{\dot{N}_{ca \rightarrow an, O_2}}{\dot{N}_{ca, in, O_2}} \quad (2.10)$$

For the engine, intake pressure can be controlled by using a throttle valve, but it is desirable to operate the engine at wide-open-throttle (WOT) condition for decreasing pumping loss and preventing vacuum pressure at the anode channels. As the mass flow rate of the anode off-gas entering the engine is given for each fuel cell operating condition while the total volume flow rate into the engine is determined by its displacement volume and rotational speed, equivalence ratio between fuel in the anode off-gas and the air for engine operation is governed by the intake pressure and temperature. For example, if the specific volume of the anode off-gas decreases by its temperature decrease, more

fresh air would be needed to satisfy the total volume flow rate in a given intake pressure, and thus the intake mixture would be leaner. Hence, intake temperature and equivalence ratio are adjusted simultaneously by the sensible energy usage of anode off-gas in the external reformer 2, in a given intake pressure, which is unique characteristic of the engine operation in such hybrid system as shown in Figure 2.9. On the other hand, spark timing, engine speed and valve timing are control parameters as in general engines, and displacement and compression ratio are geometric parameters for engines.

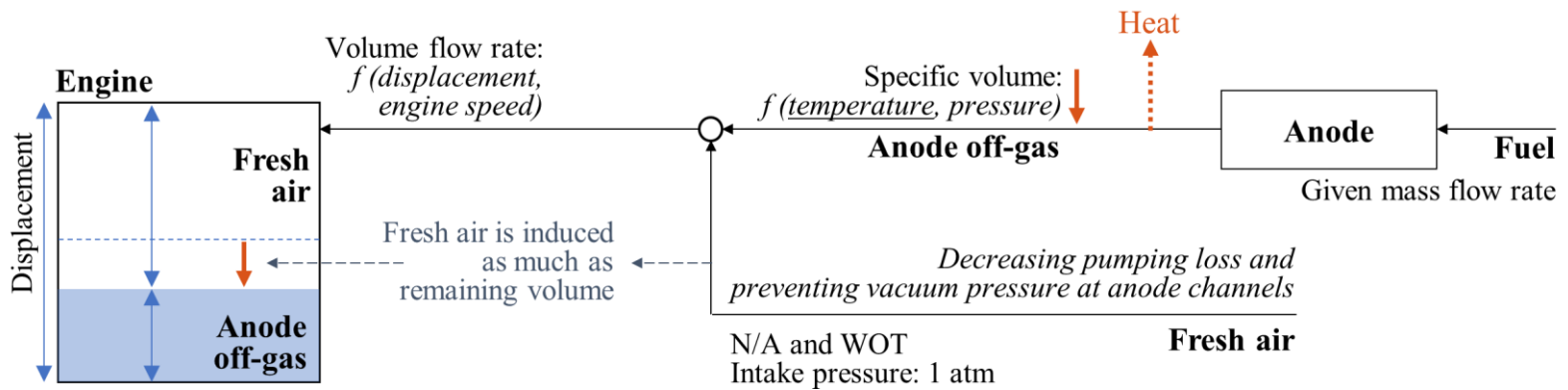


Figure 2.9 – Engine intake conditions in the hybrid system:
equivalence ratio and intake temperature varied with heat extraction from anode off-gas

2.2.2. Operating conditions for the engine experiment and the system operation

In the hybrid system, additional power generation from the engine which combusts anode off-gas is the main reason that it has higher efficiency than SOFC stand-alone system. In this study, among the aforementioned control and geometric parameters, intake temperature, equivalence ratio and spark timing, i.e., three major control factors for engine operation are investigated, because the main objective is to analyze the effect of spark-assisted ignition on the performance improvement of the hybrid system including the engine, e.g., comparison between SAI and HCCI operation in terms of both energy and exergy. Other operating parameters are fixed in order to analyze the effect of combustion nature clearly. The operating conditions are described in Table 2.3, and all the following results in Section 2.3 and Section 2.4 were carried out under these conditions.

Table 2.3 – Operating conditions for the fuel cell model and the engine experiment

Fuel cell	Operating conditions	Fuel (CH ₄) LHV [kW]	10.0				
		S/C ratio	2.5				
		Fuel utilization [%]	70				
		Air utilization [%]	35				
		Operating temperature [°C]	750				
	Mole fraction of anode off-gas [%]	H ₂	18.50				
		CO	3.32				
		H ₂ O	63.32				
		CO ₂	14.86				
		CH ₄	0.00				
Engine	Experimental conditions	Intake temperature [°C]	440	394	362	322	287
		Equivalence ratio	0.95	0.85	0.75	0.65	0.55
		Spark timing [CAD bTDC]	HCCI SAI: 40–90				
		Intake pressure [bar]	0.98 ± 0.03				

2.2.3. Definitions of related terms

In this study, **coefficient of variation** (COV) in gross mean effective pressure (GMEP) is used for the engine combustion stability measurement, which is the standard deviation divided by mean GMEP over 150 cycles, as described in Eq. (2.11). The stability limit is adopted as 10% of COV [41].

$$COV_{GMEP} (\%) = \frac{\sigma_{GMEP}}{GMEP} \times 100 \quad (2.11)$$

Combustion efficiency from the engine experimental results is defined as Eq. (2.12) based on LHV. For the calculation of LHV at engine exhaust, the combustion reaction with major species is used as provided in Eq. (2.13).

$$Combustion\ efficiency = 1 - \frac{LHV_{Engine,out}}{LHV_{Engine,in}} \quad (2.12)$$

$$\begin{aligned} n_{H_2}H_2 + n_{CO}CO + n_{CO_2}CO_2 + n_{H_2O}H_2O + n_{O_2}(O_2 + 3.7619N_2) \\ \rightarrow n_{H_2}(1 - \eta_{burn,H_2})H_2 + n_{CO}(1 - \eta_{burn,CO})CO \\ + (\eta_{burn,CO}n_{CO} + n_{CO_2})CO_2 + (\eta_{burn,H_2}n_{H_2} + n_{H_2O})H_2O \\ + (n_{O_2} - (\eta_{burn,H_2}n_{H_2} + \eta_{burn,CO}n_{CO})/2)O_2 \\ + 3.7619n_{O_2}N_2 \end{aligned} \quad (2.13)$$

The burned fraction of H₂ and CO is calculated separately using Eq. (2.13) and emission measurement such of CO and O₂. Finally, it can be obtained by solving these two following equations, i.e., Eq. (2.14) and Eq. (2.15), since the intake mixture, which is left side of Eq. (2.13), is a given condition controlled by MFC in this engine experiment. The combustion efficiency is calculated based on the LHV of the exhaust gas which is obtained by substituting the burned fraction of H₂ and CO into right side of Eq. (2.13).

$x_{exhaust,CO,measured,dry}$

$$= \frac{n_{CO}(1 - \eta_{burn,CO})}{n_{H_2} + n_{CO} + n_{CO_2} + 4.7619n_{O_2} - \left(\frac{3\eta_{burn,H_2}n_{H_2} + \eta_{burn,CO}n_{CO}}{2}\right)} \quad (2.14)$$

$x_{exhaust,O_2,measured,dry}$

$$= \frac{\left(n_{O_2} - \frac{\eta_{burn,H_2}n_{H_2} + \eta_{burn,CO}n_{CO}}{2}\right)}{n_{H_2} + n_{CO} + n_{CO_2} + 4.7619n_{O_2} - \left(\frac{3\eta_{burn,H_2}n_{H_2} + \eta_{burn,CO}n_{CO}}{2}\right)} \quad (2.15)$$

Combustion phasing in engine is calculated from net heat release rate (NHRR) profiles of engine experimental results, which is derived by the first law of thermodynamics as given in Eq. (2.16). For the terms such of pressure, volume and crank angle, measured values through the engine experiments are used. The change of specific heat ratio by the composition and the temperature is included in the calculation. The net heat release (NHR) profile obtained by integrating the NHRR profile is generally used as energy release fraction or burned mass fraction, after being normalized [41]. Thus, combustion phasing and burning rate are estimated by using NHR and NHRR in this study, e.g., CA10 is crank angle which is 10% of NHR, and time required for initial flame development is defined as from spark timing to CA10 which generally represents the onset of steady flame propagation [41].

$$\frac{dQ_n}{d\theta} = \frac{\gamma}{\gamma-1} P \frac{dV}{d\theta} + \frac{1}{\gamma-1} V \frac{dP}{d\theta} \quad (2.16)$$

Reforming rate for each external reformer is defined as the ratio of methane conversion on the mass basis through the designated reformer to the initial methane mass supply into the system, as described in Eq. (2.17).

$$\text{Reforming rate} = \frac{m_{CH_4,in} - m_{CH_4,out}}{m_{CH_4,sys,in}} \quad (2.17)$$

Available thermal energy of anode off-gas is defined as the maximum enthalpy change that can be exploited before it is fed into the engine (state 6) while satisfying the given intake gas condition (state 8) after mixed with fresh air. Available thermal energy of engine exhaust is defined as the enthalpy difference until cooling to its dew point.

Indicated efficiency of the hybrid system is defined as Eq. (2.18) including additional heat-supply, if any, to the hybrid system.

$$\text{Indicated efficiency} = \frac{W_{indicated,Engine} + W_{indicated,Fuelcell}}{LHV_{fuel,sys,in} + Q_{heat,in}} \quad (2.18)$$

For an **exergy analysis**, exergy destruction for individual components is given as Eq. (2.19) for steady-state operation.

$$X_{des} = X_{flow,in} + X_{heat,in} - W_{indicated} - X_{flow,out} \quad (2.19)$$

Finally, the whole system **exergy efficiency** is defined as Eq. (2.20) [42].

$$\text{Exergy efficiency} = \left(\frac{W_{indicated}}{X_{flow,in} - X_{flow,out}} \right)_{sys} \quad (2.20)$$

2.3. Engine experimental results

2.3.1. HCCI under intake temperature variation

At sufficiently high intake temperature, the engine with anode off-gas might operate in a pure HCCI mode. In this section, in order to understand the limit behavior of a SAI engine at the higher limit of intake temperature, we firstly discuss the operating characteristics of the engine working in an HCCI combustion mode. For the stable HCCI combustion of the anode off-gas in a given geometric compression ratio of 8.2, high intake temperature over 400°C, which is the mixture temperature of the anode off-gas and fresh air, is required, even though it has hydrogen favorable for auto-ignition. In the nominal fuel cell operation listed in Table 2.3, 70% of the fuel is already used in the fuel cell, and thus the engine is operating under low-load condition (NMEP ~1.49 bar). Still, at the intake mixture temperature of 440°C, net indicated efficiency is 23.2%, gross indicated efficiency is 26.8%, and overall efficiency of the hybrid system can be expected to increase significantly by 7%p.

In fact, it has a considerable heat loss due to the overall high in-cylinder temperature at small size single-cylinder engine, and the estimated quantity of heat loss is ~61% based on the LHV of intake gas. Furthermore, the engine operates under the lower compression ratio than typical HCCI counterpart as mentioned earlier. Hence, the pure HCCI mode has relatively low indicated efficiency, although it has good combustion efficiency of ~94% at the high intake temperature condition.

However, as shown in Figure 2.10, the combustion characteristics drastically deteriorate when the intake mixture temperature is lowered by more than 20°C,

because auto-ignition characteristics of the HCCI are considerably sensitive to in-cylinder temperature. When the intake temperature becomes lower, in-cylinder temperature also decreases during compression stroke, and ignition delay becomes longer enough to significantly affect the combustion phasing of the engine. Hence, the combustion phasing, represented by CA50 (crank angle which is 50% of net heat release), is retarded and the combustion instability increases. Indicated work also decreases because of the retarded combustion phasing and the longer combustion duration during expansion stroke, but the exhaust temperature increases because the effective expansion ratio decreases after the combustion. The CO emission increases as the combustion stability deteriorates, but it has few NO_x emissions regardless of the given intake temperature variation, as the post-combustion temperature is overall low because of many inert gases and the low-load condition.

Consequently, the low-limit of the HCCI intake temperature is ~420°C considering its COV, and it is difficult to extract more thermal energy of the anode off-gas between the stack outlet and the engine intake than this point where the anode off-gas above ~600°C and fresh air are mixed. It is also undesirable in view of the combustion stability and controllability.

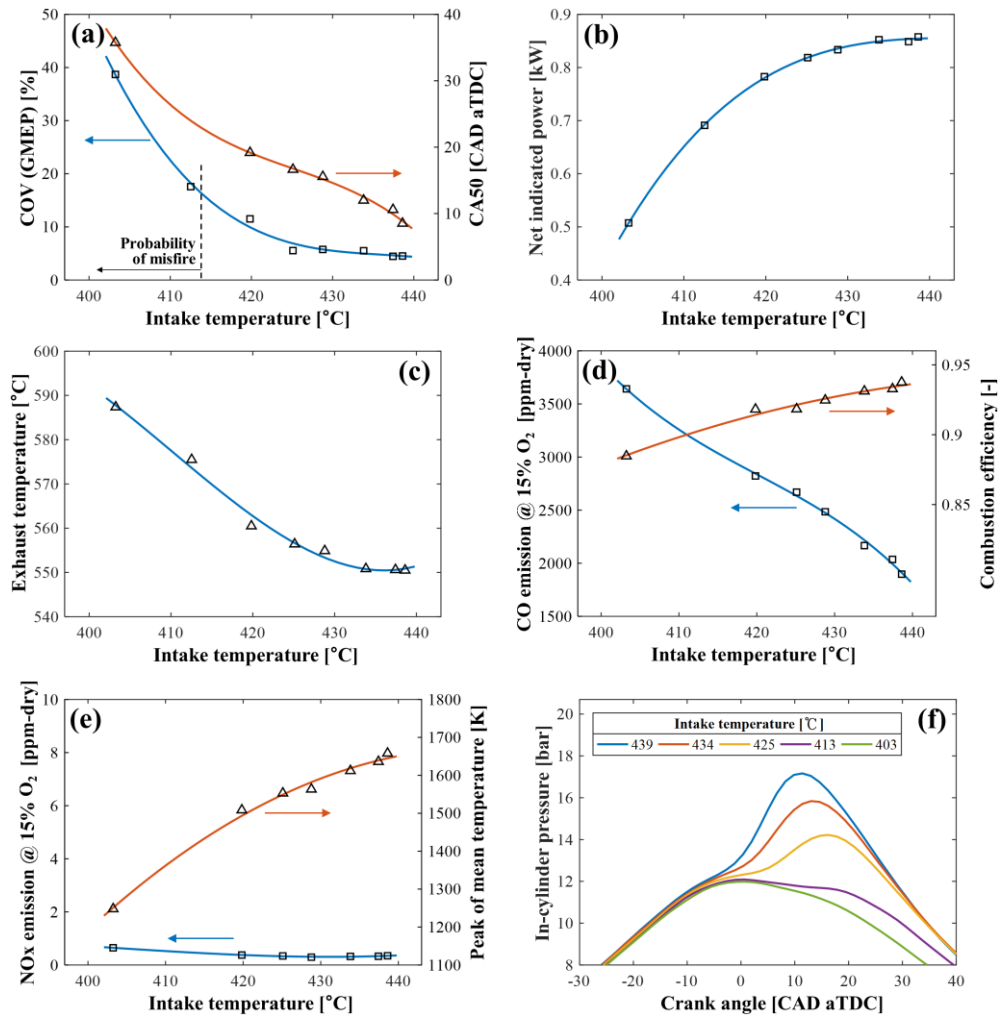


Figure 2.10 – HCCI averaged-cycle characteristics under intake temperature variation (400–440°C):

(a) combustion stability (COV) and combustion phasing (CA50) (b) net indicated power (c) exhaust temperature (d) CO emission and combustion efficiency (e) NO_x emission and peak of mean in-cylinder temperature (f) measured in-cylinder pressure;

estimated results from experimental data: CA50, combustion efficiency and peak temperature (red line in (a), (d), (e))

2.3.2. Spark-assisted ignition at the late-burn HCCI cycle condition

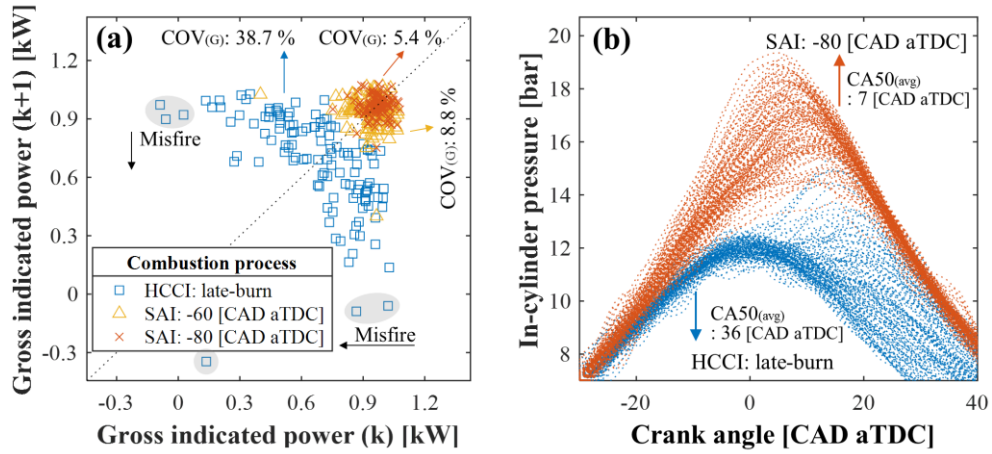


Figure 2.11 – Cycle-to-cycle variations of the HCCI and SAI cycles at the extremely late-burn condition of the HCCI described in Section 2.3.1:
 (a) return maps of gross indicated power (b) in-cylinder pressure profile for individual cycles and estimated CA50 from the pressure profile

At the extremely late-burn case of the HCCI when the intake temperature is $\sim 400^\circ\text{C}$ as described in Section 2.3.1, it has significant cycle-to-cycle variations, as shown in Figure 2.11. The power outputs of consecutive cycles are oscillating, i.e., if the indicated power of a certain cycle increases owing to temporarily advanced combustion phasing, the power decreases or misfire occurs at the following cycle, or vice versa. These are common behaviors of unstable combustion in an HCCI operation [19, 43-45], which are related to the in-cylinder temperature and residual charge at intake valve closing (IVC) influenced by the previous cycle. The present engine has low compression ratio, i.e., high clearance volume fraction, so that estimated residual mass fraction is, on average, approximately 10%. Hence, the residual effect on the following cycle is not negligible. If the combustion phasing is retarded, the exhaust gas temperature

increases. Thus, the temperature of residual gas is also increased, and then the combustion of the following cycle can be advanced by thermal effect of the such internal EGR. Furthermore, the internal EGR includes the unburned fuel by incomplete combustion as the combustion stability deteriorates. It might also enhance the combustion of the following cycle.

For stable operation in the same intake conditions, the combustion phasing can be controlled directly by using a spark, as shown in Figure 2.11. Especially at the spark timing such as -80 CAD aTDC, its COV and CA50 are almost comparable to those of the stable HCCI at the higher intake temperature. In general, the spark timing such as -80 CAD aTDC is considered extremely advanced, compared to that in typical stand-alone SI engine operation. In such general SI engines, too early spark timing results in higher negative work and heat loss, both of which are detrimental to engine efficiency. However, the engine in the hybrid system uses different characteristics of fuel from these stand-alone counterparts. The low-load condition and the highly diluted anode off-gas are unfavorable to initial flame development and the following flame propagation, despite the high intake temperature [35, 41]. Hence, sufficient time is required further for the initial flame development compared to general SI engines, e.g., ~ 70 CAD is required in this case, whereas $20\text{--}30$ CAD is required in general SI engines, based on the duration between spark timing and CA10 [46]. Nevertheless, the spark timing is not advanced more than -90 CAD aTDC in this study, preventing the possible overlap with intake valve closure and thus back-firing into the intake manifold [41]. More discussion on optimum spark timing will be presented in the next section.

In summary, it is confirmed that the unstable HCCI operation at sufficiently

low intake mixture temperature can be overcome by SAI with comparable combustion stability, indicated work and emissions to that of stable HCCI, as given in Table 2.4. Furthermore, it is also expected that thermal energy usage of the anode off-gas should be increased by lowering the intake temperature through the SAI, which leads to the following investigation.

Table 2.4 – Comparison of the averaged-cycle performance between the HCCI and SAI engine

Operating conditions		Combustion mode	HCCI	HCCI	SAI	SAI
		Intake temperature [°C]	440	403	403	403
		Spark timing [CAD aTDC]	-	-	-60	-80
Performance	Combustion	COV _(G) [%]	4.52	38.70	8.75	5.44
		CA50 _(avg) [CAD aTDC]	8.5	35.7	16.8	7.0
		Maximum pressure rise rate [MPa/ms]	0.56	0.24	0.26	0.34
	Power/Load	Gross indicated power [kW]	0.99	0.67	0.94	0.97
		Net indicated power [kW]	0.86	0.51	0.78	0.80
		NMEP [bar]	1.49	0.88	1.35	1.38
	Exhaust	CO @ 15% O ₂ [ppm-dry]	1897	3642	3095	2338
		NO _x @ 15% O ₂ [ppm-dry]	0.35	0.65	0.54	0.58
		Exhaust temperature [°C]	550	587	557	540

2.3.3. Spark-assisted ignition under intake temperature variation

2.3.3.1. Desirable spark timing for stable combustion and maximum indicated work

As mentioned earlier, combustion stability, power, and efficiency of the engine operation should be considered to find the feasible region of the SAI engine operation. In addition, with the introduction of spark ignition in the engine operation, the spark timing should be investigated to achieve the desirable operation for those metrics.

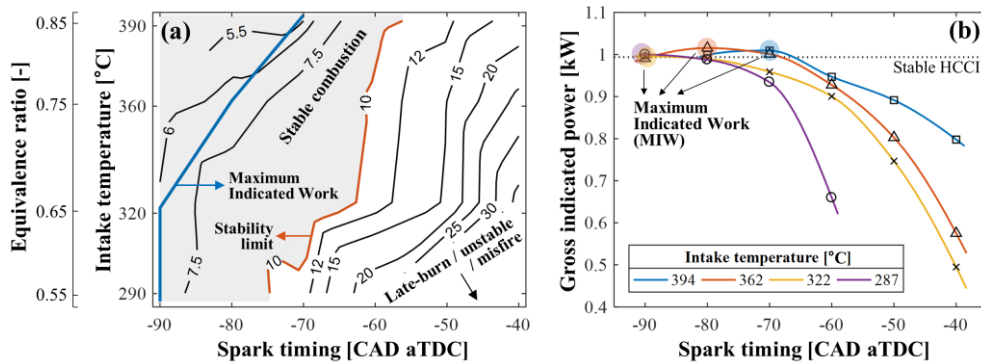


Figure 2.12 – Desirable spark timing region for stable combustion and maximum indicated work: (a) stable combustion region and MIW on the COV map [%] (b) gross indicated work under spark timing variation

Firstly, the combustion stability should be secured for stable power generation, because the instability of the engine can disturb the hybrid system. Figure 2.12(a) depicts the COV of GMEP in the spark timing and intake temperature map for the reference operation of the fuel cell stack. Again, the throttle valve for the engine intake air remains wide open to maintain near-atmospheric pressure throughout anode channels; therefore, the lowered intake temperature leads to lower volume flow rate for a given mass flow rate of the

anode off-gas and thus relatively higher intake air flow rate or leaner intake mixture in the end. The stable combustion region is a shaded area as shown in Figure 2.12(a). As the intake temperature decreases, the stability limit of the spark timing is advanced, because the low intake temperature and high-diluted lean-mixture are unfavorable to either the flame propagation or the auto-ignition of the unburned gas.

Secondly, it is important to maximize the engine work within the stable combustion region because the additional power is the main objective of the hybrid system. Figure 2.12(b) shows the spark timing for maximum indicated work (MIW). The resultant performance such as power and stability in the SAI engine are almost similar to that of the stable HCCI.

Consequently, the most desirable spark timing for the stable combustion and power can be approximated as a blue line shown in Figure 2.12(a), i.e., MIW region. In view of the MIW being already extremely advanced and the combustion stability, it is not desirable to lower the intake temperature further while maintaining the WOT condition because the equivalence ratio also decreases further at the same time [35, 41].

Figure 2.13 shows that both combustion stability and maximum power can be achieved by the control of combustion phasing, i.e., CA50, regardless of the intake temperature. In this study, the desirable combustion phasing, i.e., CA50, is within 0–15 CAD aTDC. This controllability of SAI is considerably significant for the stability of the system operation, since now the engine can operate somewhat independently to the intake temperature variation, which may occur either by the variation in the system operation or by unknown disturbance.

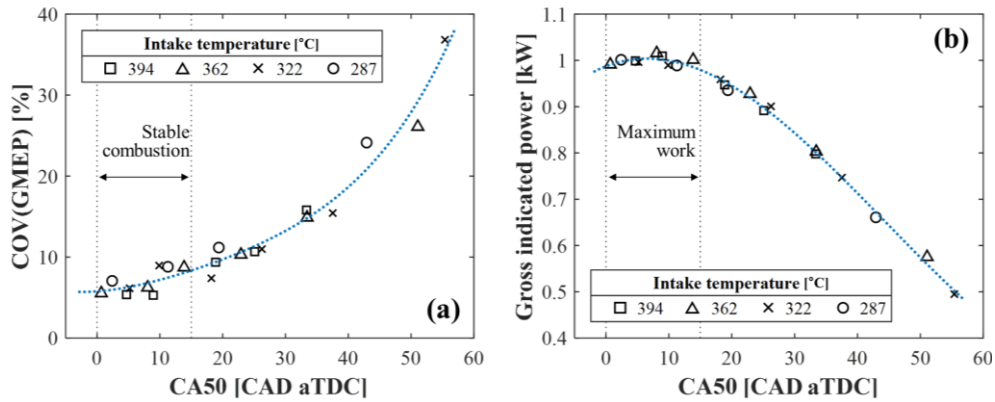


Figure 2.13 – Correlation of combustion stability and power with CA50 controlled by SAI: (a) COV(GMEP) under CA50 variation (b) gross indicated power under CA50 variation

2.3.3.2. Operating performance at the desirable spark timing

Figure 2.14 shows the operating characteristics of the SAI engine at the MIW region shown in Figure 2.12. Figure 2.14(a)–(b) shows emission characteristics. There are only few NO_x emissions, because the post-combustion peak temperature is low, although it increases slightly as the equivalence ratio decreases. As the intake temperature (and equivalence ratio) decreases, the CO emission increases mainly due to the aforementioned unstable engine operation, resulting in incomplete combustion cycles intermittently. If the intake temperature (and equivalence ratio) is higher than an optimum, the CO emission may slightly increase due to the local deficiency of oxygen by inhomogeneity in cylinder, which is similar to the emission characteristics of the typical SI engine [41]. The CO emission implies that the engine exhaust has combustion inefficiency and also has chemical energy left in the form of CO. For the calculation of the combustion efficiency shown in Figure 2.14(a), not only

measured CO emission but also H₂ emission estimated by CO and O₂ measurement values are used as discussed in Eqs. (2.12)–(2.15).

However, the engine exhaust temperature becomes overall lowered as the intake temperature decreases as shown in Figure 2.14(c), owing to lower in-cylinder temperature at the spark timing, lower post-combustion temperature by further lean-burn as well as lower combustion efficiency. Nevertheless, the available sensible energy of the exhaust in Figure 2.14(d), which is the enthalpy difference until cooling to the dew point, is almost at the same level as the stable HCCI, because of the increase in the mass flow by the equivalence ratio decrease.

Furthermore, the temperature and the available sensible energy of the exhaust can be increased by converting its remaining chemical energy to thermal energy through the catalytic oxidizer right after the engine (shown in Figure 2.1), which has high CO conversion efficiency even at a low equivalence ratio [41], while solving the CO emission issue. As a result, the increases in the available sensible energy of the exhaust can be achieved by the SAI and the catalytic oxidizer up to ~0.6 kW, as the intake temperature decreases. The available sensible energy of the anode off-gas is also increased by ~0.35 kW, which is the maximum enthalpy difference that can be used before mixing with the fresh air to satisfy the given intake temperature and equivalence ratio for each condition. Especially, considering that it is nearly at the highest temperature in the entire system, it can be used to supply thermal energy required for the high temperature BOPs, e.g., external reformer 2 as shown in Figure 2.1. At the lowest intake temperature (equivalence ratio) condition in Figure 2.14(d), the available sensible energy of the anode off-gas corresponds to ~7% of the system fuel LHV. It is a significant thermal energy which is capable of increase in external reforming rate up to

~20%p through the external reformer 2.

It should be noted that the SAI has overall lower combustion efficiency as compared to the HCCI counterpart, while the power output is almost at the similar level as shown in Figure 2.14(e). As the intake temperature (and equivalence ratio) decreases, the flame propagation speed and the combustion efficiency decrease. It is not favorable condition for work extraction in the engine. However, the overall in-cylinder temperature also decreases, and it leads to decrease in heat loss of the engine. It is favorable condition for work extraction in the engine. Hence, the power generation of the engine could be maintained at the similar level under intake temperature (equivalence ratio) variation as shown in Figure 2.14(e), since there is the trade-off effect. Overall, the engine has low indicated efficiency, i.e., net efficiency is ~23% and gross efficiency is ~27%, due to considerable heat loss by the small bore and air-cooled structure.

Figure 2.14(f) depicts the heat loss of the engine calculated using the first law of thermodynamics considering the power output from the engine and the states of intake/exhaust mixture. HCCI operation that requires high intake temperature for anode off-gas combustion has relatively large amount of heat loss compared to SAI operation. In addition, as the intake temperature and equivalence ratio decrease, the engine operates at even lower operating temperature leading to significant decrease in the heat losses, while achieving higher thermal efficiency with lean-burn condition. Consequently, SAI operation can improve the engine-related performance such as the increase of available sensible energy for the system operation, while generating the power and efficiency similar to HCCI.

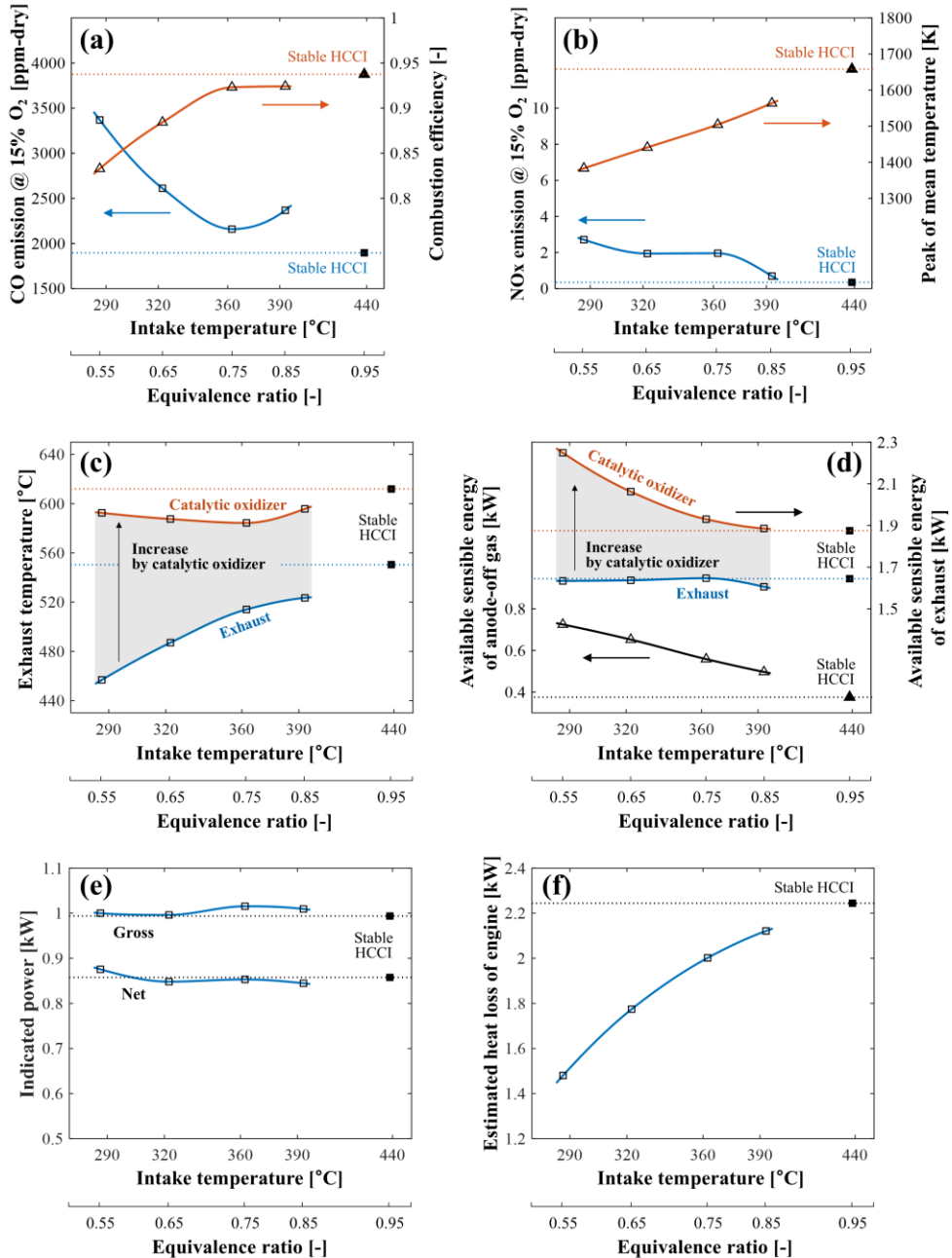


Figure 2.14 – Operating performance of the SAI at the MIW region:
 (a) CO emission and combustion efficiency (b) NO_x emission and peak of mean in-cylinder temperature (c) exhaust temperature (d) available sensible energy of anode off-gas and exhaust (e) indicated power (f) estimated heat loss of engine

2.3.4. Combustion mode under intake temperature variation

Historically, it has been considered that the highly-diluted gas, such as anode off-gas, is not appropriate for SI combustion due to its low laminar flame speed from significant dilution [14, 18, 35, 41]. In this subsection, more discussion will be given on the feasibility of the anode off-gas combustion by a spark and how it differs from general, non-diluted SI operation.

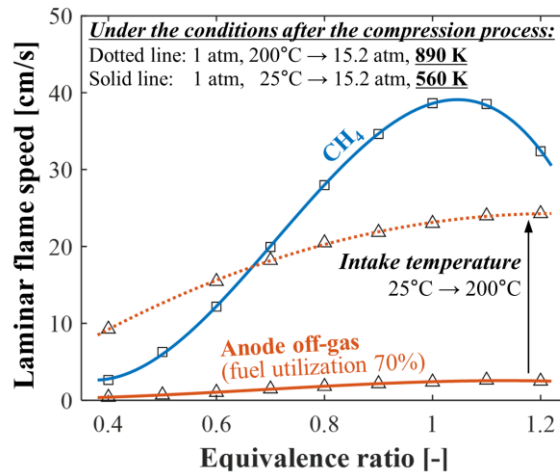


Figure 2.15 – Laminar flame speed of methane and anode off-gas under equivalence ratio variation calculated using Cantera toolbox and GRI 3.0 mechanism

Figure 2.15 shows laminar flame speed as a function of fuel-air equivalence ratio, which is calculated using Cantera toolbox [33] based on Python and GRI 3.0 mechanism [34], for methane and anode off-gas provided in Table 2.3. In Figure 2.15, the solid lines for both fuels represent the laminar flame speed under the temperature and pressure conditions after the ambient temperature mixture is compressed in the engine, calculated by polytropic process. The dotted line shows the laminar flame speed of the anode off-gas mixture at the post-compression condition when the intake mixture temperature increases to 200°C.

If the engine using anode off-gas as fuel operates at ambient temperature, the laminar flame speed is extremely lower than methane and it is clearly impossible to ignite the anode off-gas by a spark. However, when the intake temperature increases, the laminar flame speed increases at a level similar to methane, as shown in Figure 2.15. Hence, if a part of the thermal energy of the anode off-gas is used for engine operation, it can be sufficiently combusted with appropriate spark timing control. In Section 2.3.2 and 2.3.3, it is confirmed that it can be achieved to ignite the anode off-gas using a spark, although extremely advanced spark timing is required.

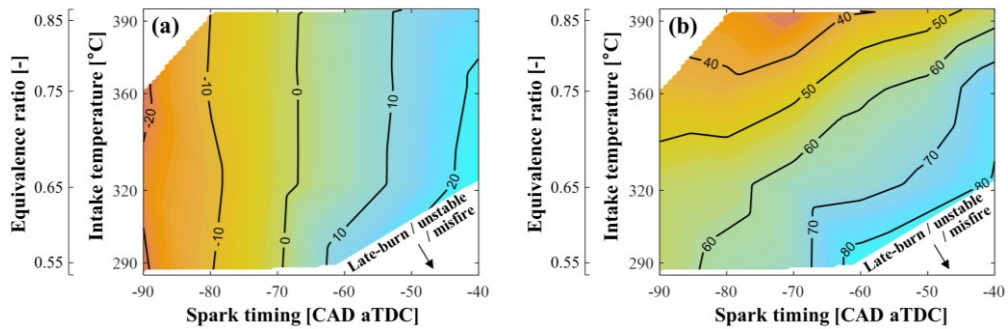


Figure 2.16 – Combustion phasing and duration under spark timing and intake temperature variation: (a) CA10 [CAD aTDC] (b) combustion duration from CA10 to CA90 [CAD]

Figure 2.16(a) shows CA10 (crank angle which is 10% of net heat release) which generally represents the start of the steady flame propagation [41]. It is noted that initial flame propagation timing is dominantly changed by the spark timing, but less by the intake temperature (or equivalence ratio). However, once the flame propagates, the combustion duration from CA10 to CA90 in Figure 2.16(b) shows strong dependency on intake temperature and equivalence ratio, where the duration reduces as the intake temperature increases. This result can

be partly explained by the aforementioned trend of the laminar flame speed, which bases the turbulent flame speed of such flame propagation.

There is an additional complication in the combustion phenomena of SAI with its high intake mixture temperature, which are different from the general SI operation with ambient temperature of intake fuel and air. Clearly, the combustion phenomena achieved in the operational map of Figure 2.16, are not pure HCCI because there is no combustion without a spark when the intake temperature is under $\sim 400^\circ\text{C}$ for a given anode off-gas. However, there is a probability of homogeneous auto-ignition in the unburned gas, which might be induced by raised temperature and pressure during flame propagation by SAI. Hence, a transition region of SI and HCCI may exist in the operating regime in Figure 2.16, and it is necessary to understand the thermodynamic state and chemical reaction kinetics of the unburned gas during the flame propagation, for clarifying whether it is pure SI or spark-assisted HCCI, i.e., spark-assisted compression ignition (SACI).

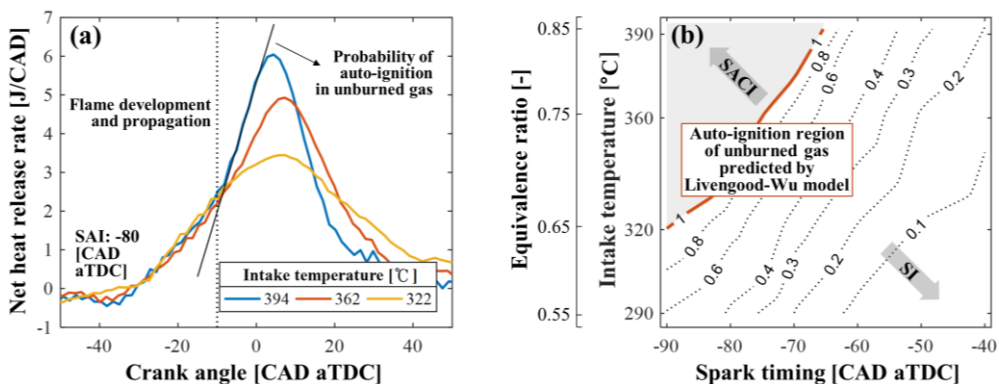


Figure 2.17 – SAI combustion characteristics predicted by Livengood–Wu correlation during combustion process:
 (a) net heat release rate profile (b) auto-ignition probability in the unburned gas on the Livengood–Wu integration map

The difference in combustion modes can be observed in the representative NHRR profiles in Figure 2.17(a), which is provided in Eq. (2.16). At the initial flame development and propagation, the slope is similar even under the intake temperature variation. However, the slopes of the NHRR differ evidently after the initial flame propagation with different intake temperature conditions; the higher the intake temperature, the higher the peak value of the NHRR. This finding qualitatively shows a transition of combustion mode from pure SI to SACI.

In previous studies, in-cylinder visualization and slope or second derivative of HRR are used to distinguish between SI and HCCI [47, 48]. Double Wiebe function is also used to investigate the SACI combustion mode [45]. However, it is difficult in this study to distinguish the combustion mode quantitatively and accurately by NHRR, because of relatively moderate combustion by the low-load and the high-diluted lean operation. Hence, the probability and tendency of the SACI are investigated quantitatively through the Livengood–Wu correlation in this study.

The Livengood–Wu correlation is used to predict the auto-ignition timing based on the ignition delay [49]. In particular, the correlation would be best suited for the synthesis gas combustion, because it is single-stage combustion in which there is no negative temperature coefficient (NTC) region and cool flame effect [50, 51]. The correlation is described in Eq. (2.21) as given in Ref. [49], where t_o is the start of combustion in this study, i.e., spark timing, and t_c is the auto-ignition timing.

$$\int_{t_o}^{t_c} \frac{1}{\tau_{id}(T, P, x)} dt = 1.0 \quad (2.21)$$

To calculate the ignition delay of the unburned gas at each crank angle, the mean temperature of the unburned gas during the flame propagation is estimated from the experimental data such as in-cylinder pressure by Eq. (2.22) as given in Ref. [41], under the assumption that the in-cylinder pressure is uniform, where T_u is the unburned gas temperature, P_c is the in-cylinder pressure, T_o and P_o are the unburned gas temperature and in-cylinder pressure at some reference crank angle, e.g., the start of combustion, and γ_u is specific heat ratio of the unburned gas. The change of specific heat ratio by temperature is also included in the calculation in evaluating Eq. (2.22). The ignition delay of the unburned gas at each crank angle is obtained through chemical kinetics calculation using Cantera toolbox [33] and GRI 3.0 mechanism [34], where the unburned gas temperature estimated by Eq. (2.22) is used. The details for the ignition delay calculation of the unburned gas at a given crank angle during the combustion are provided in Appendix B.

$$\frac{T_u}{T_o} = \left(\frac{P_c}{P_o} \right)^{(\gamma_u - 1)/\gamma_u} \quad (2.22)$$

Based on the above, auto-ignition probability is calculated by integrating the inverse of the ignition delay profile over time. If the integration value up to the end of the combustion is less than 1, there is no auto-ignition in the unburned gas, and it is considered as pure SI.

Figure 2.17(b) shows the integration results up to the end of the combustion. Firstly, as the spark timing is advanced, initial flame development and propagation speed is slow because of the low temperature at the timing. However, the in-cylinder pressure and the temperature are increased by the combustion during compression, and it makes the ignition delay decreased. Thus, the auto-

ignition in the unburned gas becomes more probable. Secondly, as the intake temperature and equivalence ratio decrease, the effect of the intake temperature is relatively dominant despite the specific heat ratio increase with leaner mixture. Therefore, with the decrease in intake temperature, in-cylinder temperature is overall lower throughout the compression and the combustion processes, which is unfavorable for the auto-ignition of the unburned mixture. As a result, the auto-ignition region of the unburned gas predicted by the Livengood–Wu correlation, i.e., SACI region, is a shaded area as shown in Figure 2.17(b). The MIW region, described in Section 2.3.3, is in the SACI region if the intake temperature is higher than $\sim 320^{\circ}\text{C}$; otherwise, it may be within the SI region. In other words, the MIW region is in the transition area between SI and HCCI.

It is also noted that the shaded area in Figure 2.17(b), coincides well with the stable combustion region, where COV is below 7.5% in Figure 2.12(a). Fast burning rate through the auto-ignition, i.e. SACI combustion, helps to stabilize the combustion behavior, as compared to relatively slower burning rate of pure flame propagation in SI, especially at this low-load (NMEP ~ 1.5 bar) and with highly-diluted fuel (anode off-gas) caused by high fuel utilization of the fuel cell.

2.4. System performance

In the previous section, the effects of the SAI on the combustion stability, power, emissions and available thermal energy for the system operation are analyzed from the perspective of the engine. Ultimately, it is important to investigate how the SAI engine affects the hybrid system as a whole, in terms of the system operability with system efficiency. Especially, the following discussion is based on the optimum engine operating condition in a given intake temperature, i.e. MIW region (in Figure 2.12), and further focused on the function and consequence of newly added components in the hybrid system, i.e., catalytic oxidizer in the engine exhaust and external reformer 2 for anode off-gas heat extraction.

2.4.1. Improvement in efficiency and thermal self-sustainability

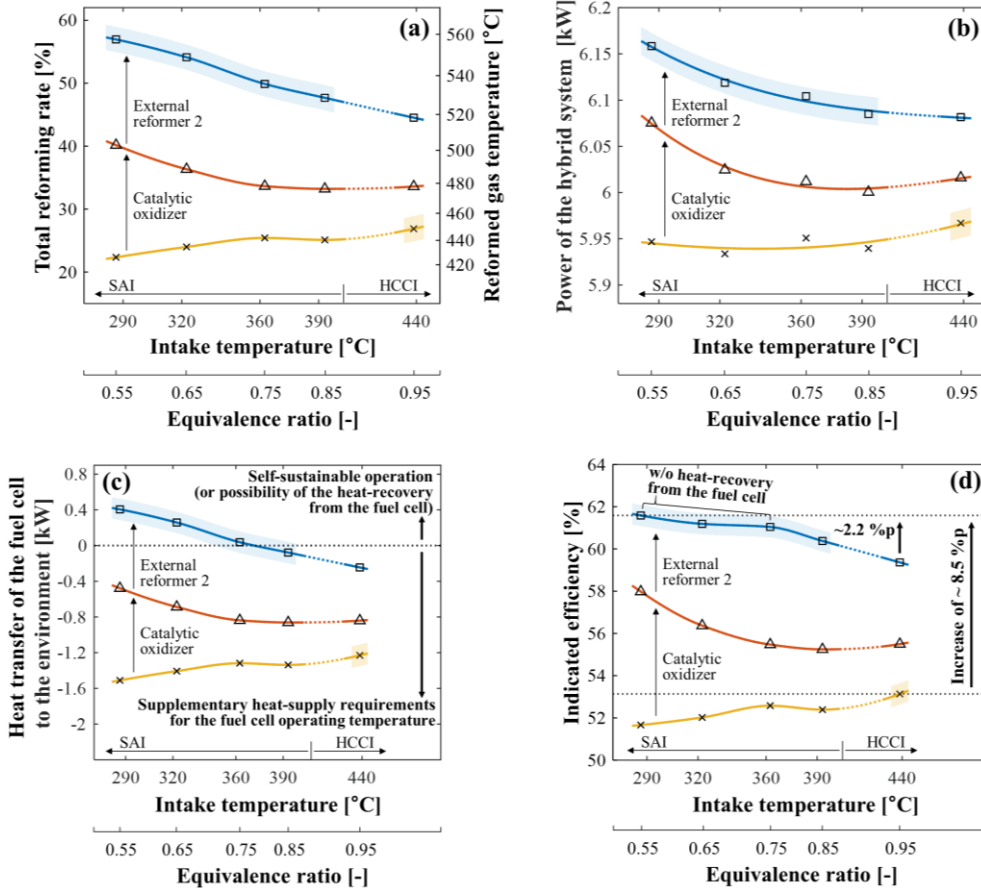


Figure 2.18 – Effect of the SAI engine on the hybrid system operation: (a) total reforming rate and reformed gas temperature (b) power of the hybrid system (c) heat transfer of the fuel cell to the environment to achieve the fuel cell operating temperature (750°C) (d) indicated efficiency of the hybrid system including the additional heat-supply requirements as represented in the negative values of Figure 2.18(c)

To operate the fuel cell more efficiently and self-sustainably and to reduce the thermal gradient and the carbon deposition in the fuel cell stack, it is necessary to increase the external reforming rate and the fuel cell inlet temperature [15, 27]. In this study, thermal energy supply for external reforming is a main factor affected by combustion strategy, because the engine exhaust and the anode off-gas used in the engine as fuel are heat sources for the external reforming.

Figure 2.18(a) shows the effect of combustion strategies and additional BOP components on the overall external reforming. Here, the additional BOP components refer to those newly added in the hybrid system, which are originally absent from the stand-alone SOFC system. These include the catalytic oxidizer in the engine exhaust, which is to fully combust the remainder of the fuel out of the engine, and the external reformer 2, which is adopted to directly use the thermal energy of the anode off-gas before it enters the engine. To increase the reforming rate, it is important to better exploit the thermal energy at the engine in/outlet, i.e., anode off-gas and engine exhaust, both of which are heat source supplied to external reformers. In the case of the system without the catalytic oxidizer and the external reformer 2, the reforming rate is decreased slightly as the intake temperature decreases, depicted as yellow line in Figure 2.18(a), because the engine exhaust temperature also decreases which is the only heat source for external reforming at external reformer 1, as discussed earlier in Figure 2.14(c). However, if there is a catalytic oxidizer which converts the residual chemical energy of the engine exhaust into thermal energy, i.e., combustion inefficiency in the engine corresponding 5–15% under the intake temperature variation, the more thermal energy is used at external reformer 1 and it leads to

increase of external reforming rate as the intake temperature decreases, depicted as red line in Figure 2.18(a), since temperature gradient for heat exchange becomes improved.

Furthermore, in the case that the thermal energy of anode off-gas is also used at the external reformer 2, the more additional external reforming is achieved as the intake temperature decreases, depicted as blue line in Figure 2.18(a), because the available thermal energy of anode off-gas for the operation of the external reformer 2 increases as shown earlier in Figure 2.14(d). However, when the intake temperature is below $\sim 360^{\circ}\text{C}$, the additional reforming rate in the external reformer 2 remains at almost consistent level, which is represented by difference between blue and red line in Figure 2.18(a). This is due to the effectiveness limit of the heat exchange in the reformer that we mentioned in Section 2.1. As the intake temperature decreases, the outlet temperature of the external reformer 1, i.e., the inlet temperature of the external reformer 2 increases as shown in red line of Figure 2.18(a), and it results in decrease of temperature gradient with anode off-gas in the external reformer 2. Thus, it is not possible to use all the available thermal energy of anode off-gas which is increased by the lowered intake temperature. Nevertheless, the total external reforming rate is improved by $\sim 30\%$ compared to the HCCI case without the additional BOP components, as shown in Figure 2.18(a). The reformed gas temperature (on the right axis) can be increased by $\sim 100^{\circ}\text{C}$.

Figure 2.18(b) shows that the power output of the hybrid system can be increased by ~ 0.2 kW (increase by $\sim 2\%$ on the fuel input LHV basis) over the given intake temperature variations. It results from the change in cell voltage of the fuel cell, which is affected by the inlet gas composition, since the engine

power is almost not changed under the intake temperature variation as shown in Figure 2.14(e). The increase of the external reforming rate with lowered intake temperature and the additional BOP components leads to high hydrogen yield, which corresponds to the change from ~26% to ~46% of mole fraction on a wet basis. It results in the increase of the Nernst voltage and the reduction of the activation and concentration losses in the fuel cell. Finally, the cell voltage rises from 0.7590 V to 0.7849 V.

To ensure whether the system is self-operable, supplementary heating requirement is separately evaluated to achieve the energy balance. As mentioned in the assumption in Section 2.1.4, only major heat losses (or transfers) occur either in the fuel cell stack or in the engine. Since the actual heat loss of the engine operation is calculated based on the experiment, the following discussion will be focused on the energy balance around the fuel cell stack. From the system-level modeling, the in/outlet thermodynamic states and the power output of the fuel cell stack are already known, and thus the heat transfer from/to the fuel cell stack can be calculated. Figure 2.18(c) shows the heat transfer from the stack to the environment, where the positive number implies that some amount of heat loss is allowed in the stack operation, while the negative number implies that supplementary heating is required to achieve the given in/out conditions of the fuel stack or that hybrid system as a whole may not be operable for itself. As discussed above, the increase in the external reforming rate can be achieved through the lowered intake temperature and the additional components. It means that anode inlet temperature (reformed gas temperature) also increases as confirmed in the right axis of Figure 2.18(a). Cathode inlet temperature also should be increased by the more efficient operation of HEX 3, since it is desirable

to reduce the temperature difference between the stack inlet gases, which is the assumption in Section 2.1.4. The increase in thermal energy of the stack inlet gases results in the improvement of thermal self-sustainability of the stack which includes the endothermic reforming reaction. Consequently, if the reformed gas temperature, shown in Figure 2.18(a), is lower than $\sim 530^{\circ}\text{C}$, it may not be possible to achieve the proper stack operation without the additional heat-supply, mainly due to the increased proportion of the endothermic internal reforming from decreased external reforming rate. In other words, the self-sustainability of the hybrid system is improved by the engine operation with lowered intake temperature and by those additional components, i.e., external reformer 2 and catalytic oxidizer. Even though several assumptions that we made in the modeling might not be applicable with different fuel cell stack, e.g., the proper SOFC working temperature at 750°C , the main conclusions made here are still qualitatively applicable.

Finally, Figure 2.18(d) shows indicated efficiency of the hybrid system considering the supplementary heat-supply, if any, as described in Eq. (2.18). The indicated efficiency can increase up to $\sim 8.5\%$ compared to the hybrid system with HCCI combustion in the engine, through the use of SAI in the engine with the external reformer 2, catalytic oxidizer and lowering the intake temperature. In terms of combustion strategies, i.e., comparison between SAI and HCCI, the hybrid system using the SAI engine is capable of achieving increase in the indicated efficiency by 2.2% through using the thermal energy of anode off-gas in the external reformer 2, which is secured by the lowered intake temperature.

In the perspective of economics, it is desirable to add some components, if the improvement of economic efficiency by increase in energy efficiency, i.e.,

decrease in fuel cost, is higher than the increase in the system cost such as investment and maintenance. In this hybrid system, the thermally self-sustainable operability, i.e., feasibility of the hybrid system, is also improved through the external reformer 2 as discussed in Figure 2.18(c), since it contributes to increase in the stack inlet temperature (reformed gas temperature). Consequently, both two external reformers should be adopted to use the available energy as much as possible, for the improvement of system efficiency and feasibility.

2.4.2. Improvement in exergy destruction

In this final section, the results of an exergy analysis on the hybrid system will be discussed. As already shown in Figure 2.18(c), only marginal operating conditions exist for self-sustainable operation of the hybrid system. The heat loss from the engine is one most dominant factor, but the system might be further optimized in the future, either by operating strategy or by configuration itself, if we could analyze the irreversible losses associated with its operating conditions discussed so far. In this study, exergy destruction is chosen as an indicator for such irreversible losses.

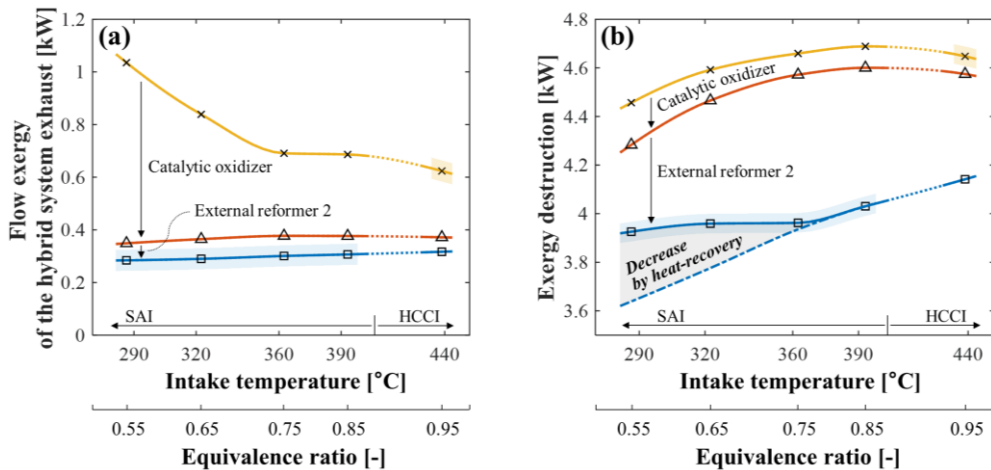


Figure 2.19 – Exergy analysis on the hybrid system: (a) flow exergy of the hybrid system exhaust (b) exergy destruction in the hybrid system

Figure 2.19 shows the results of the exergy analysis on the hybrid system. In a given amount of the system fuel and air input, it is obvious that the system power can be increased as the flow exergy in the exhaust stream is minimized. The flow exergy entering into the hybrid system is ~ 10.4 kW in our tested condition, and the SOFC–SAI engine hybrid system with the external reformer

2 and the catalytic oxidizer uses almost all flow exergy in the system as shown in Figure 2.19(a). In the range of tested intake temperature variation, the exhausting exergy remains almost the same throughout. In particular, residual chemical exergy by the combustion inefficiency of the engine is captured in the system through the catalytic oxidizer. Furthermore, the anode inlet temperature as well as the external reforming rate increases through the addition of the external reformer 2 as shown in Figure 2.18(a). Therefore, by the modeling assumption of the equality in the anode and cathode inlet temperatures of the fuel cell stack, the thermal energy of the cathode off-gas is further exploited in HEX 3 to adjust the cathode inlet temperature to the same level with the anode inlet temperature, but only up to the maximum effectiveness limit. Consequently, the thermal energy that exits the system is reduced and the flow exergy-out decreases.

Exergy destruction in the hybrid system is shown in Figure 2.19(b), considering the transfer of heat flow exergy at the fuel cell calculated by using the fuel cell operating temperature. The lower the exergy destruction, the better the exergy efficiency. Therefore, it means that the system exergy efficiency is improved by using the SAI engine, the external reformer 2, the catalytic oxidizer and lowering the intake temperature, especially through the external reformer 2. The solid line in Figure 2.19(b) represents the exergy destruction including the additional heat-supply represented in the negative values shown in Figure 2.18(c). On the other hand, the shaded area in the figure is to show the potential of recovering the destroyed exergy otherwise, if it is possible to exploit the exergy related with heat transfer from the fuel cell stack in other components, for the conditions with the positive values in Figure 2.18(c).

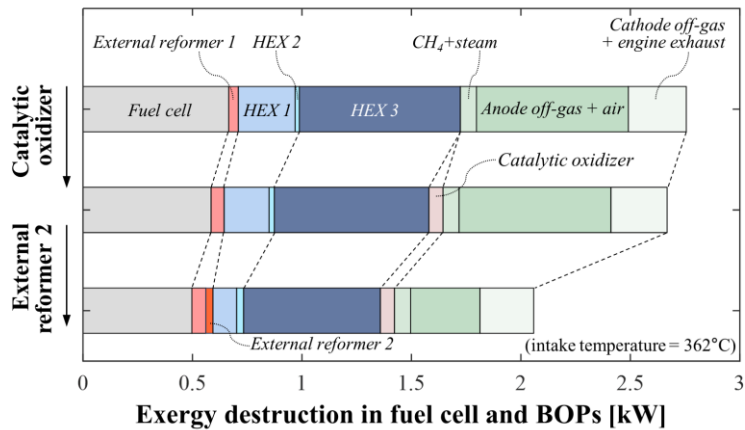


Figure 2.20 – Exergy destruction in fuel cell and BOPs by additional BOPs (intake temperature = 362°C)

Figure 2.20 shows the breakdown of exergy destruction in individual components at an engine intake temperature of 362°C. Firstly, in the case of using a catalytic oxidizer in the engine exhaust, it leads to the reduction of exergy destruction in the fuel cell and thus increased fuel cell power output, mainly due to the increase in external reforming, even though there is a similar amount of exergy destruction added in the catalytic oxidizer which has irreversible chemical reaction. In HEX 3, it is operated more efficiently, because cathode inlet temperature is increased to match the anode inlet temperature as described above. Therefore, the exergy destruction in HEX 3 decreases. In HEX 1, the inlet temperature (state 17) decreases as the cathode off-gas transfers more heat in HEX 3. Thus, the inlet temperature difference between the hot and cold gas in HEX 1 decreases, resulting in the decrease of exergy destruction. As a result, the overall exergy destruction slightly decreases when the catalytic oxidizer is applied to the hybrid system. Secondly, in the case of using the external reformer 2 with the catalytic oxidizer, there is further decrease of the exergy destruction

in the fuel cell, HEX 1 and HEX 3, for similar reasons as mentioned above. The significant decrease of exergy destruction results from the decrease in mixing process of anode off-gas and fresh air for the engine intake. If there is no external reformer 2, the thermal energy of anode off-gas which has the highest temperature in the system cannot be exploited and simply transferred to the environment for satisfying the given intake condition. It is a considerable exergy destruction as shown in Figure 2.20. It is noted that the anode off-gas temperature after external reformer 2 (state 6) is still sufficiently high to meet the requirement of engine intake condition, compared to fresh air temperature. In addition, the HEX 3 is still dominant for the exergy destruction among the heat exchangers as shown in Figure 2.20, owing to the highest temperature difference and flow rate between the inlet gases, i.e., cathode outlet gas and fresh air.

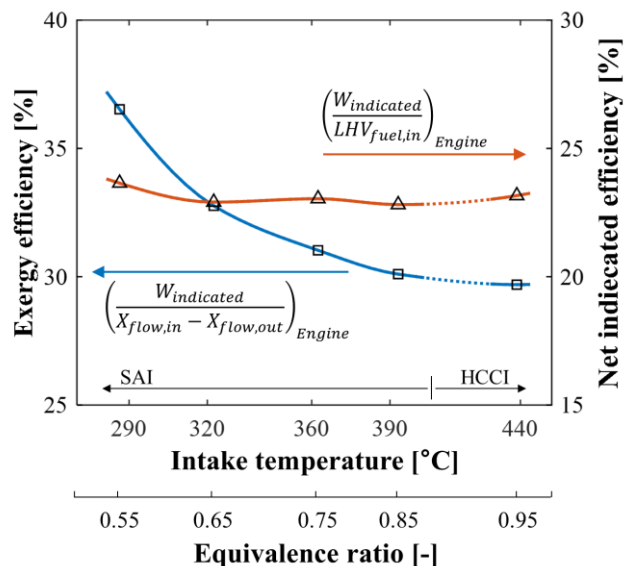


Figure 2.21 – Exergy and indicated efficiency of the engine under the intake temperature (equivalence ratio) variation

In the engine, as the intake temperature decreases, the exergy efficiency of the engine operation increases considerably as shown in Figure 2.21, mainly due to the reduced heat loss. As a result, the SAI operation reduces exergy-in required for stable combustion, reduces exergy destruction by heat loss, and ensures exergy-out while generating similar power, compared to the HCCI operation. The exergy-out increase leads to improved system efficiency, because it is transferred to the fuel cell through BOPs converting it into thermo-mechanical or chemical exergy. The transferred exergy may result in increase of cell voltage and thermal self-sustainability in fuel cell. Furthermore, it is important for the system efficiency to reduce the exergy destruction by the heat loss in the engine rather than the fuel cell, because it is difficult to recover the heat loss from the engine with relatively low temperature of surface, oil and coolant. Hence, it is important for the exergy destruction decrease and thermal self-sustainability to lower the intake temperature of the engine in the hybrid system, while exploiting the thermal energy of anode off-gas further.

2.5. Conclusions

In this chapter, the feasibility of spark-assisted ignition engine which is a new combustion strategy in the SOFC hybrid system was investigated through engine experiment. Furthermore, analysis on the operating performance of the novel SOFC–ICE hybrid system using spark-assisted ignition, the external reformer 2 and the catalytic oxidizer was conducted through integrating the engine experimental results with simulation model developed and validated in this study. The detailed findings are described below.

- 1) The spark-assisted ignition makes the combustion of the anode off-gas stable (COV: 5~7%) and controllable for combustion phasing, even while the intake temperature of the engine decreases by $\sim 150^{\circ}\text{C}$ compared to the HCCI operation that the combustion phasing is highly sensitive to the intake temperature. The exergy efficiency of the engine also increases by $\sim 7\%$. At this condition, the thermal energy of the anode off-gas can be used more up to ~ 0.35 kW for the hybrid system operation through the external reformer 2.
- 2) CO emission by the combustion inefficiency and insufficient exhaust temperature in the SAI engine can be resolved by the catalytic oxidizer. Its chemical energy can be converted to thermal energy and used for the hybrid system operation downstream of the engine. There is almost no NO_x emission, i.e., ~ 3 ppm corrected to 15% O_2 , as the post-combustion temperature is low due to low-load condition and highly-diluted fuel-lean mixture.
- 3) The SAI engine operates in the HCCI–SACI–SI transition region, which is investigated by using the Livengood–Wu correlation, within the combustion

limit of the intake temperature and equivalence ratio. In the MIW region, even though the SAI engine combusts the anode off-gas with considerable dilution, the engine power is maintained at the almost same level with stable HCCI operation, i.e., ~ 0.86 kW. Furthermore, by using the additional thermal energy in the system, the reforming rate and the inlet temperature of the fuel cell are increased. Hence, the fuel cell power is improved by ~ 0.2 kW, and the supplementary heat-supply required for the fuel cell operating temperature is decreased or eliminated.

- 4) Consequently, it is confirmed by energy and exergy analysis that the thermal self-sustainability of the hybrid system is improved, and the indicated efficiency increases by $\sim 8.5\%$ over the hybrid system with HCCI operation; through the SAI engine with the external reformer 2, the catalytic oxidizer and the intake temperature decrease. The SOFC-SAI engine hybrid system is expected to be able to achieve the indicated efficiency of $\sim 61.6\%$, through the analysis including the heat transfer of the engine and the fuel cell. The SAI engine is capable of generating $\sim 14.2\%$ of the hybrid system power.
- 5) Spark-assisted ignition, which is a new concept for the anode off-gas combustion, is capable of controlling the combustion stably coping with ever-varying anode off-gas from the fuel cell under widely operating variation in the hybrid system. Furthermore, it could contribute to improvement in operability of the hybrid system while reducing the exergy destruction in the engine. Hence, this combustion strategy is expected to be applicable for the practical development of SOFC-ICE hybrid system.

Chapter 3. Design of system configuration for the SOFC-SAI engine hybrid system

3.1. Considerations

3.1.1. Thermal energy distribution of anode/cathode off-gas

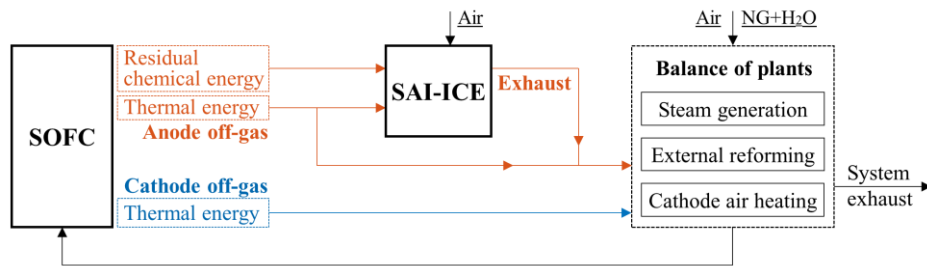


Figure 3.1 – Energy flow of anode/cathode off-gas in SOFC–SAI engine hybrid system

In SOFC system using natural gas as system fuel, thermal energy should be supplied to BOPs required for the fuel cell operation, as shown in Figure 3.1. For the operation in the anode, SMR is adopted, which is endothermic reaction, since it has high hydrogen yield [28]. Thus, steam should be supplied into the system for the SMR operation. For the fuel cell operation, the air supplied to the cathode should be pre-heated nearly to the fuel cell operating temperature. Sufficient thermal energy should be supplied to such BOP operation for the desirable SOFC operation. If not, sufficient SOFC operating temperature cannot be achieved, or supplementary heat-supply should be required, and it leads to the decrease in the system efficiency. Hence, when incorporating ICE into the fuel cell system as a bottoming cycle of the fuel cell stack, ICE should use residual chemical energy in the anode off-gas efficiently, while reducing the thermal energy required for

achieving the stable combustion in such ICE operation. It was confirmed in Chapter 2 that the requirements for ICE can be achieved through SAI with lowered intake temperature, which has higher combustion controllability and exergy efficiency than HCCI. Therefore, efficient thermal energy distribution for the BOP operation such as external reforming, steam generation and cathode air heating is considerably important for thermally self-sustainable operation of the SOFC-SAI engine hybrid system.

As shown in Figure 3.1, the hybrid system has two significant heat sources for the BOP operation which are anode/cathode off-gas with the highest temperature in the system, i.e., at the operating temperature of fuel cell. In the followings, all possible combinations are investigated to design new configuration for optimal thermal energy distribution of anode/cathode off-gas, while considering some practical constraints for the case reduction. Firstly, the anode off-gas is not used for cathode air heating, because the air supplied to the cathode generally has a significantly larger heat capacity due to its mass flow rate compared to the anode off-gas. Secondly, anode off-gas before entering into the ICE is only used for external reforming, not for steam generation, in order to increase anode inlet temperature by thermal energy of anode off-gas which has the highest temperature in the hybrid system. If the anode off-gas enters into the engine after being used for both external reforming and steam generation, it could be difficult to secure the appropriate thermal energy of the anode off-gas required for stable combustion in engine despite it is ignited by a spark. Hence, thermal energy of engine exhaust after anode off-gas combustion is considered for steam generation instead of directly using anode off-gas. Thirdly, one of engine exhaust and cathode off-gas should be supplied for each BOP configuration. As a result,

all the possible cases under the aforementioned considerations are defined as Table 3.1, and there are 9 cases in total as shown in Figure 3.2.

Table 3.1 – Case study for thermal energy distribution of anode/cathode off-gas for BOP operation

	Thermal energy of			Number
	anode off-gas	engine exhaust	cathode off-gas	of cases
External reforming	Use	Use or not	Use or not	3
Steam generation	Not	Use or not	Use or not	3
Cathode air heating	Not	not	Use	1

However, when considering some practical constraints, some cases provided in Figure 3.2 are not feasible. In the Case 4–6 that steam is generated by using only engine exhaust heat, the engine exhaust heat required for the steam generation may not be sufficient depending on the operating condition of engine. Thus, these cases are excluded from the case study. In the Case 7–8 that the engine exhaust heat is only used for external reforming, the residual heat of engine exhaust, which inevitably has a temperature higher than inlet temperature of steam-methane mixture at the external reformer, e.g., above $\sim 150^{\circ}\text{C}$ in general [40], is transferred to the environment. Since it is thermal energy loss, these cases are also excluded. In addition, the Case 9 is excluded since the engine exhaust heat is not used at all and wasted in the system exhaust. In the end, only Case 1–3 remain feasible for further consideration. In these cases, since both the engine exhaust and the cathode off-gas are used for steam generation, the key issue for the new configuration design is reduced to thermal energy distribution for external reforming, i.e., how to supply the thermal energy available in the system

for external reforming.

In this study, the mixing of anode/cathode off-gas before entering into the engine is not considered for the thermal energy distribution. If anode/cathode off-gas are mixed before the engine and used for the system, the intake gas of engine has more nitrogen fraction than fresh air, and its composition varies depending on air utilization in fuel cell. Hence, it is unfavorable for stable combustion. In addition, the thermal potential of cathode off-gas may decrease by the exergy destruction in the engine, e.g., heat loss by cooling. In order to reduce the complexity of structure and control within the hybrid system in real world operation, branching of thermal stream, e.g., anode/cathode off-gas, is also not considered for the thermal energy distribution.

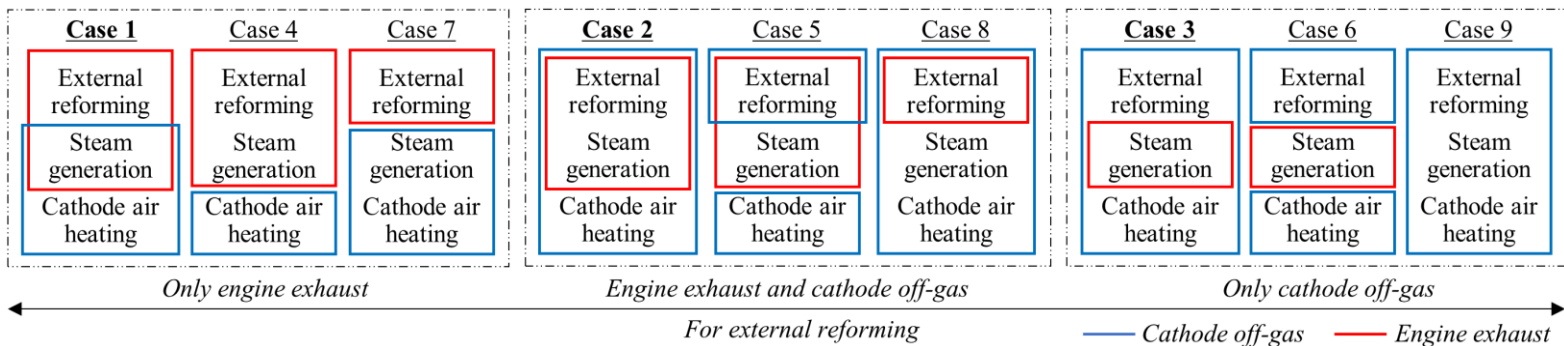


Figure 3.2 – All the possible cases for system configuration based on Table 3.1

3.1.2. Order of heat-supply for each BOP operation

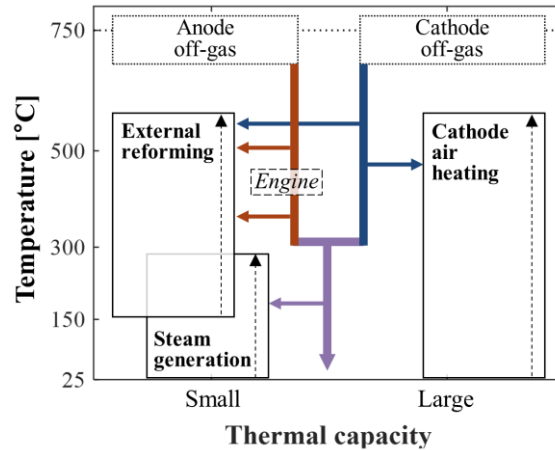


Figure 3.3 – Operating temperature range of BOPs and flow diagram for thermal energy of the anode/cathode off-gas in the Case 2 discussed in Figure 3.2

For the detailed design of new configuration, the order in which thermal energy is used should be determined. Since the thermal energy is supplied for the BOP operation through counter-flow heat exchanger in the hybrid system, temperature gradient and heat capacity are important factors to decide the order among BOPs. As an example, the order of thermal energy flow is determined based on the Case 2 which uses both engine exhaust and cathode off-gas for the external reforming, for consideration of all possibilities. Figure 3.3 shows the typical operating temperature range of BOPs and the heat flow diagram of the Case 2, considering the following.

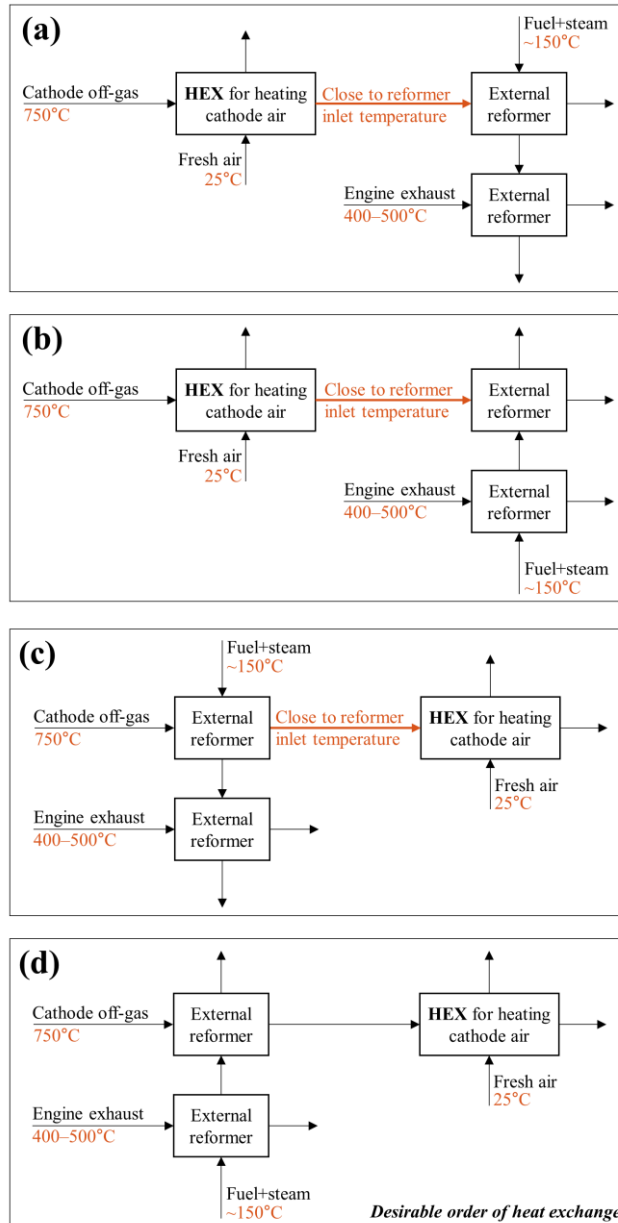


Figure 3.4 – All the possible configurations of heat exchange for external reforming and cathode air heating by using engine exhaust and cathode off-gas:
(a),(b) cathode off-gas → cathode air heating → external reforming
(c),(d) cathode off-gas → external reforming → cathode air heating
(a),(c) fuel-steam mixture → cathode off-gas → engine exhaust
(b),(d) fuel-steam mixture → engine exhaust → cathode off-gas

Firstly, thermal energy for steam generation is lastly supplied, since its operating temperature is the lowest in the system. Secondly, if the cathode off-gas is used for cathode air heating prior to external reforming as shown in Figure 3.4(a)–(b), it is not efficient or not feasible for the subsequent external reforming, because the temperature of the cathode off-gas could decrease considerably near to the reformer inlet gas temperature. Therefore, the cathode off-gas is used first for external reforming prior to cathode air heating. Thirdly, if the cathode off-gas is used first for external reforming prior to engine exhaust as shown in Figure 3.4(c), it is not efficient for the subsequent cathode air heating, since the temperature of the cathode off-gas decreases to around the inlet temperature of external reformer, e.g., $\sim 150^{\circ}\text{C}$ [40]. It is not desirable for cathode air which should be heated to $500\text{--}600^{\circ}\text{C}$. Thus, the engine exhaust is used first for external reforming as shown in Figure 3.4(d). Consequently, the order of the thermal energy flow is determined as shown in Figure 3.3.

3.2. Details in designed configuration

The detailed system configuration for Case 1-3 is shown as Figure 3.5. In this study, methane is used as surrogate fuel of natural gas. Steam-methane mixture is partially reformed in two steps in the Case 1 or 3. In the Case 2, the mixture is partially reformed in three steps by using anode/cathode off-gas and engine exhaust. The partially reformed gas is supplied to the anode and generates power by electrochemical reaction. The anode off-gas which has dilution such as H_2O and CO_2 is used as fuel for the SAI engine after heat-supply to external reformer 2. The engine exhaust heat after the catalytic oxidizer is supplied to external reformer 1 in the Case 1 and the Case 2, and it is then supplied to HEX 2 for steam generation. Here, the catalytic oxidizer is an after-treatment device for unburned fuel in the engine exhaust, if any. The system exhaust heat after HEX 1 is supplied to the fresh air (state 12) to capture the residual thermal energy. The cathode off-gas supplies heat to the external reformer 3 in the Case 2 and 3, and it is then supplied to the HEX 3 for the cathode air heating.

For the steam generation, two heat exchangers are used, since the engine exhaust after external reformer and cathode off-gas after cathode air heating have different qualities in heat exchange. The temperature of the engine exhaust after external reforming may be higher than that of the cathode off-gas after cathode air heating, because the inlet temperature of external reformer is higher than the environment temperature as shown in Figure 3.4(d). As a result, the engine exhaust is supplied to a heat exchanger (HEX 2) for generating super-heated vapor. The engine exhaust after HEX 2 and the cathode off-gas after cathode air heating are then mixed for heat-supply to another heat exchanger (HEX 1) to heat water. The mixed gas which has large heat capacity is appropriate for steam

generating with large latent heat.

However, the HEX 1 has a significant issue due to phase change of water, i.e., pinch limit. The heat capacity until the saturated state is relatively small compared to the latent heat capacity. It results in rapid temperature increase of water until the saturated state. As a result, it makes the efficiency of HEX 1 deteriorated and the unused thermal energy of the mixed gas is lost. To recover the system exhaust heat as much as possible, it is recovered through an additional heat exchanger (HEX 4) to fresh air supplied to the cathode. The HEX 4 is important for feasible thermal energy distribution in real-world operation.

In the following discussions, instead of analyzing each individual case above, the performance will be compared through the all-included configuration by investigating on the effectiveness change of external reformer 1 and 3 upon optimization of operating conditions. For example, if effectiveness of external reformer 1 is equal to zero in an optimal operating condition, it implies that there is little use of external reformer 1 in the system, i.e., the Case 3 is preferred. The most efficient design of system configuration is proposed in Section 4.4.1.

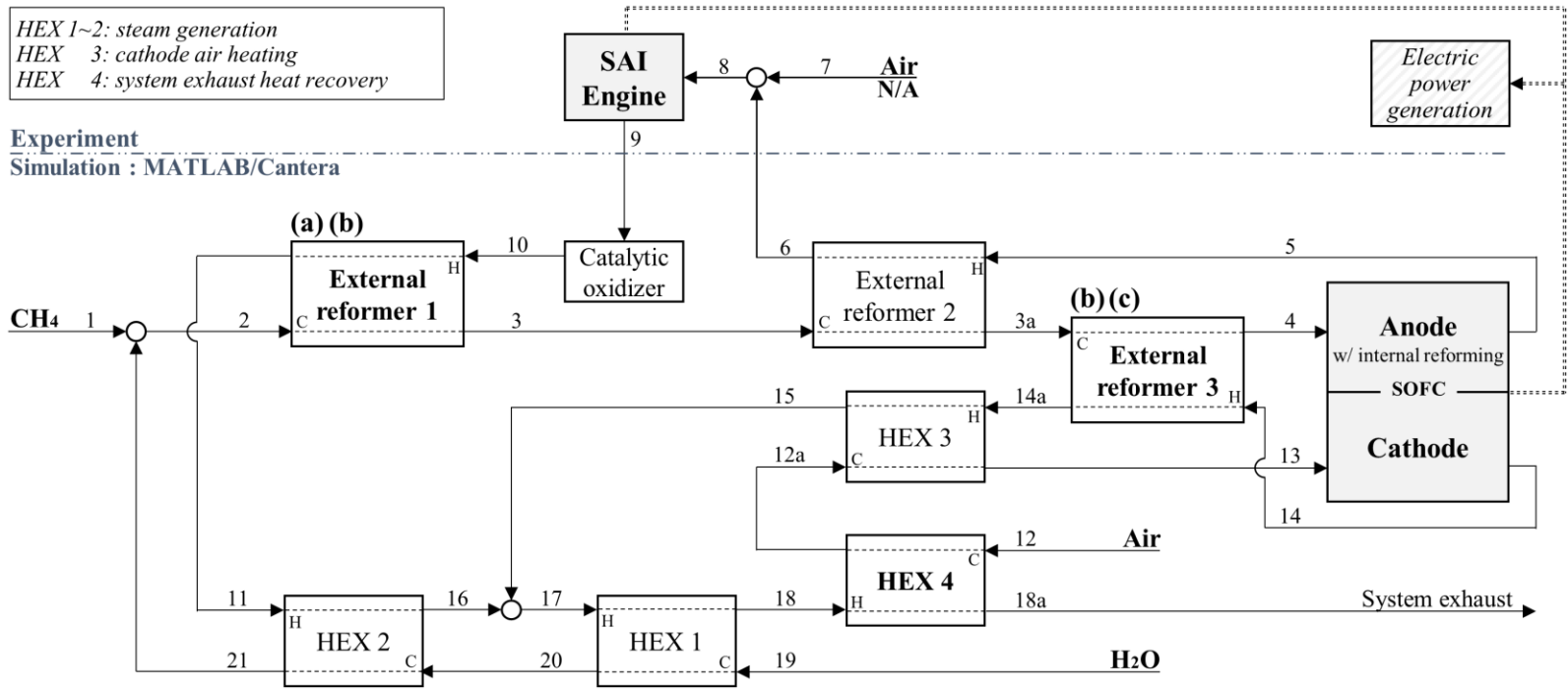


Figure 3.5 – System configuration for case study under variation of thermal energy supply for external reforming:
 (a) Case 1 (b) Case 2 (c) Case 3

Chapter 4. Parametric analysis on the SOFC-SAI engine hybrid system operation

4.1. Research methodology

In order to evaluate the designed configurations in Chapter 3 under variation of operating conditions, system-level analysis was conducted. The SAI engine performance was measured through actual engine experiments. For the fuel cell, physics-based model previously developed and validated with actual stack experimental data in Chapter 2 was used. The operating performance of the hybrid system was analyzed by integrating of the SAI engine experimental results and system modeling including fuel cell and BOPs. The integration algorithm of engine experiments and the simulation model was newly developed for the new system configuration as described in Section 4.1.2. The details are described in the following sub-sections.

4.1.1. Assumptions and feasible operating conditions

4.1.1.1. Assumptions for system-level analysis

Pressure in all flow paths is assumed 1 atm without pressure drop. In addition, heat losses are considered only for fuel cell stack and engine. The assumptions for the analysis on the system operation are introduced as follows and represented in Figure 4.1.

Fuel cell:

- (1) Design operating temperature of fuel cell is 750°C within the typical range for the SOFC [6]. Hence, heat transfer of fuel cell satisfying the temperature ($T_5=T_{14}=750^\circ\text{C}$) is calculated using the first law of thermodynamics.
- (2) BOP operation is adjusted (under constraints) to achieve the same anode and cathode temperature at the fuel cell inlet to reduce thermal gradient in fuel cell. ($T_4=T_{13}$)

Engine:

- (3) Spark timing is controlled to produce maximum work in a given intake conditions.
- (4) Engine operates at wide-open-throttle (WOT) condition to reduce pumping loss.
- (5) Intake temperature is kept higher than 100°C to prevent water condensation in the intake gas. ($T_8 > \sim 100^\circ\text{C}$)

Heat exchangers and external reformers:

The effectiveness of heat exchangers should be maximized as much as possible for efficient heat supply, but the upper limit is set at 0.85 considering the realistic operation.

- (6) HEX 1: Pinch limit is 10°C.
- (7) HEX 4: System exhaust including vapor water (state 18a) is not cooled down below its dew point.
- (8) External reformer 2 (ER 2): Effectiveness is adjusted to satisfy the engine intake condition requirement (state 8). It means that thermal energy should be supplied for ER 2 within the available thermal energy of anode off-gas, which is the maximum enthalpy difference that can be used before mixing with the fresh air while satisfying the given intake temperature and equivalence ratio.
- (9) HEX 3 and External reformer 3 (ER 3): Effectiveness is adjusted to satisfy the assumption (2).
- (10) HEX 2 and External reformer 1 (ER 1): Effectiveness is adjusted by the given reformer inlet temperature (T_2) in the assumption (11) below. If heat supply is not sufficient to generate steam satisfying the temperature, the effectiveness of ER 1 is lowered to increase the heat supply for steam generation instead of external reforming. In the opposite case, the effectiveness of HEX 2 is adjusted.
- (11) External reformer 1 (ER 1): Inlet temperature is fixed at 150°C, considering the feasible reformer inlet temperature [40]. ($T_2=150^\circ\text{C}$)

4.1.1.2. Feasible operating conditions

Feasible operating conditions (limitations on the feasible operation range) of the hybrid system are defined as follows and represented in Figure 4.1.

Fuel cell:

- (a) It should have thermally self-sustainable operation. It is not feasible operation, if it requires additional heat supply to maintain the design operating temperature.

Engine:

- (b) Combustion should be controlled stably [41].
(Coefficient of variation (COV) < 10%)
- (c) The maximum advanced spark timing is 110 CAD bTDC to prevent the possible overlap with general intake valve closing (IVC) [41].
(Spark timing < 110 CAD bTDC)

4.1.2. Integration of engine experimental results and simulation model for system-level analysis

4.1.2.1. Engine experimental setup

The experimental setup for the evaluation of the SAI engine performance under variation of operating conditions is shown in Figure 2.2. The basic structure of the engine experimental setup is the same as the study of Chapter 2. In brief, emulated anode off-gas, equivalence ratio, intake temperature and intake pressure of the SAI engine can be controlled as described in Chapter 2. The simulation model of the fuel cell and BOPs developed in Chapter 2 was also used for the study of this Chapter, and the intake gas conditions at given operating conditions were calculated using the fuel cell model. However, in this chapter, there are some changes or improvement of engine experimental setup as shown in Figure 4.2.

Firstly, Yamaha MZ 300 which is a single-cylinder engine was used for the experiments in this Chapter to increase the effective load in the engine, i.e., NMEP, with decreasing the displacement. Hence, it was expected that the combustion efficiency could be increased at each operating condition. The detailed specifications are provided in Table 4.1. Secondly, for the further accurate analysis on exhaust characteristics, an exhaust analyzer (MK 9000) was used to measure exhaust composition such as CO, H₂, O₂ and NO_x emissions, on a dry basis in real time. Especially, the fuel components of anode off-gas, i.e., CO and H₂, were measured. Thus, the burned fraction of CO and H₂ can be calculated directly from the measured results. In addition, for the data processing and analysis of each engine operating condition, ~450 consecutive cycles at steady-state were used. Data acquisition and equipment control were performed

based on the Simulink real-time.

Table 4.1 – Specifications of a single-cylinder engine: Yamaha MZ 300

Yamaha MZ 300	
Bore	78 mm
Stroke	63 mm
Compression ratio	8.1
Displacement	301 cc
Engine speed	1,800 RPM
Cooling system	air-cooled
Oil temperature	$90 \pm 5^{\circ}\text{C}$

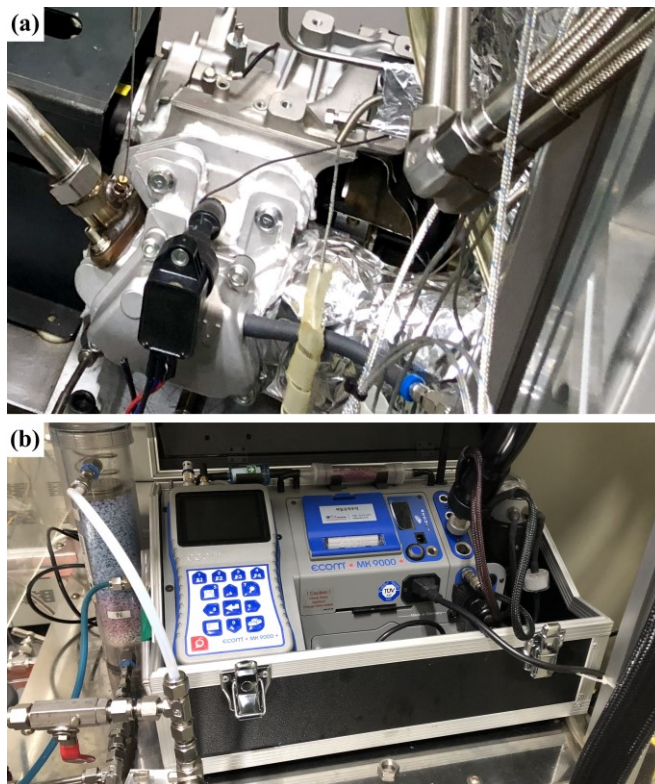


Figure 4.2 – Experimental apparatus: (a) Yamaha MZ 300 (b) Exhaust analyzer (MK 9000)

4.1.2.2. Simulation model descriptions

As described in Chapter 3, the performance of each case can be investigated through one configuration, i.e., the Case 2. The configuration of the Case 2 consists of a fuel cell, an engine, external reformers, heat exchangers, a catalytic oxidizer and mixers (13 components and 25 thermodynamic states). Hence, the simulation model developed in Chapter 2 is appropriate for the case study to investigate the optimal system design, and it was used in this Chapter. In order to calculate thermodynamic properties of methane and synthesis gas [35], Cantera toolbox [33], GRI 3.0 mechanism [34] were used in the simulation model based on MATLAB (Mathworks). Brief descriptions for the modeling are provided again as the following.

The fuel cell model includes major reactions in the anode such as electrochemical reaction, steam-methane reforming (SMR) and water-gas shift reaction (WSGR). The mole numbers of oxygen ion transfer per mole of fuel, i.e., H_2 and CO , are the same. Hence, the overall amount of oxygen ion transfer from cathode to anode can be determined by a given current demand, regardless of the extent of electrochemical reaction for each fuel. Since it is assumed that the fuel cell operates under equilibrium-state at isobaric, isothermal process, the anode off-gas state is calculated with the Gibbs free energy minimized including oxygen transfers by a given current demand. Consequently, the anode off-gas composition becomes a function of current demand, i.e., fuel utilization, at the given system operating conditions such as system fueling rate, S/C ratio, design operating temperature and pressure of the fuel cell. Cathode off-gas state is determined by current demand and the amount of air supplied to cathode, i.e., air utilization. After anode inlet gas state, i.e., partially reformed rate, is determined

by the engine and BOPs operation, cell voltage is calculated by considering Nernst voltage [6] and losses such as activation loss [52], ohmic loss [53] and concentration loss [54]. Finally, heat transfer for maintaining the design operating temperature is calculated by using energy balance around the stack operation. Detailed descriptions are provided in Appendix A.

BOPs such as heat exchangers, external reformers and a catalytic oxidizer are modeled under adiabatic process. Heat exchangers are developed based on counter-flow and effectiveness method [39]. Since heat required for external reforming is supplied by heat transfer, external reformers are also modeled as heat exchanger, while endothermic reforming reaction and compositional change under the equilibrium-state assumption are included for the energy balance in the external reformers. Catalytic oxidizer for after-treatment is modeled as oxidizing the engine exhaust under equilibrium-state at isobaric and adiabatic process, by using residual oxygen in the exhaust.

4.1.2.3. System-level analysis

As described in Chapter 2, the operating performance of the hybrid system is analyzed by integrating of the SAI engine experimental results and system modeling including fuel cell and BOPs. However, integration algorithm of engine experiments and the simulation model is newly developed and applied to system-level analysis, since the novel system configurations are developed through the case study described in Chapter 3. The algorithm for the integration of engine experimental result and simulation model is provided in Figure 4.3.

The anode off-gas state (state 5) such as composition, temperature and flow rate can be calculated first based on each operating condition of fuel cell such as system fueling rate, S/C ratio, fuel and air utilization and operating temperature, as mentioned in Section 4.1.2.2. The cathode in/outlet information (state 12 and 14) also can be calculated. Using the anode off-gas state, e.g., composition, the engine experiment is performed under variation in equivalence ratio, intake temperature and spark timing. The exhaust/intake data from the engine experiment is used for the system simulation.

Methane is fed to external reformer 1 after mixing with steam. Steam-methane mixture (state 2) and the engine exhaust after catalytic oxidizer (state 10) are used for calculation of external reformer 1. In the next step, the partially reformed gas (state 3 in the Case 1–2) or steam-methane mixture (state 3 in the Case 3) and the anode off-gas (state 5) are used for calculation of external reformer 2. Thus, the anode off-gas into the engine (state 6) and partially reformed gas after external reformer 2 (state 3a) are determined, considering the available thermal energy of anode off-gas satisfying the give intake condition of the engine (state 8). If the calculated temperature (state 8) is lower or higher than

the intake temperature from the engine experiment result at a given operating condition, the external reformer 2 operation should be re-calculated.

In the Case 2 and 3, external reformer 3 operation is calculated using the partially reformed gas (state 3a) and cathode off-gas (state 14), under the related assumptions provided in Section 4.1.1. However, pre-heated air information (state 12a) which is obtained from HEX 4 calculation is required for the HEX 3 calculation. Furthermore, system exhaust information after HEX 1 (state 18) which is determined by using cathode off-gas after HEX 3 (state 15) is required for the HEX 4 calculation. Hence, iteration process should be performed after setting the initial value for system exhaust after HEX 1 (state 18) for the calculation of external reformer 3, HEX 3, HEX 4 and HEX 1. The iteration process excluding the external reformer 3 is also necessary in the Case 1.

From the initial state 18, it is possible to calculate the operation of HEX 4 and external reformer 3 (in the Case 2–3). HEX 3 operation is then calculated, and the cathode off-gas after HEX 3 (state 15) and anode/cathode inlet gas (state 4 and 13) can be determined. However, if HEX 3 is operated over the effectiveness limit, effectiveness of external reformer 3 is adjusted in the Case 2 and 3, since the external reformer 3 affects the anode/cathode inlet temperature.

However, another iteration is required, because HEX 1 and HEX 2 affect each other. After setting the initial value of the water state (state 20), the HEX 2 operation is calculated using the engine exhaust after external reformer 1 (state 11) determined previously, and the super-heated vapor (state 21) is then determined. In the next step, the HEX 1 operation is calculated using the cathode off-gas after HEX 3 (state 15) determined previously, and the water state (state 20) is newly determined. If the water state converges, the iteration process

finishes and the operation of HEX 1 and HEX 2 is determined. Since the state 18 is updated in this calculation, the operation of HEX 1 and HEX 2 is also included in the iteration procedure for the state 18.

After convergence of the state 18, if the updated steam-methane mixture (state 2) is not equal to initial value which is a given operating condition, additional iteration process is required for the convergence of the steam-methane mixture state. If the updated value is higher than the given operating condition, the effectiveness of HEX 2 is adjusted in a direction to reduce the heat-supply for steam generation. In the opposite case, the effectiveness of external reformer 1 is adjusted in a direction to reduce the heat-supply for external reforming, to secure enough thermal energy for steam generation. When all the iteration process finishes, fuel cell performance is calculated using the anode in/outlet gas (state 4,5) and the cathode in/outlet gas (state 13,14). Finally, operating performance of the hybrid system and all thermodynamic states are determined.

Operating conditions

Fuel cell: fuel flow rate, S/C ratio, fuel and air utilization , operating temperature
Engine: equivalence ratio (intake temperature), load, intake pressure, spark timing , speed, compression ratio, displacement
BOP: inlet temperature of external reforming, reforming proportion of each external reformer

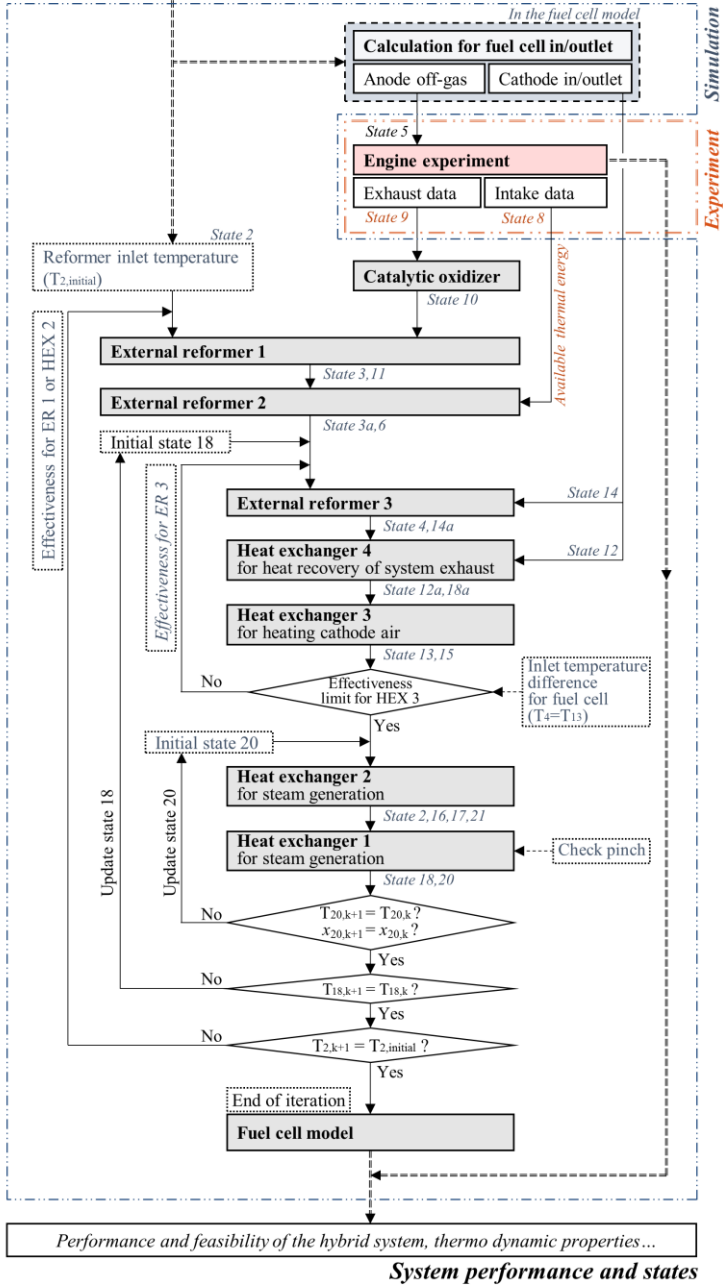


Figure 4.3 – Algorithm for the integration of engine experimental result and simulation model of fuel cell and BOPs

4.2. Details in the hybrid system operation

4.2.1. Parameter selection

The hybrid system has a lot of operating parameters as shown in Figure 4.4. For the fuel cell, fueling rate, S/C ratio (steam supply rate), fuel utilization and air utilization are controllable parameter. For the engine, equivalence ratio, intake pressure, intake temperature, load, spark timing and engine speed are controllable parameters. For the new configuration design, the reforming proportion of each external reformer is an important parameter as described in Chapter 3.

For the optimal load distribution in the hybrid system, it is focused on the fuel cell and the engine which are the power generation device in the system. Furthermore, air supply for each power generation device is also significant, since both electrochemical reaction in the fuel cell and combustion reaction in the engine that produce power are affected by the air supply. In terms of the system operation, effectiveness of each external reformer is an important parameter for the hybrid system design, since the given heat source, i.e., thermal energy of anode/cathode off-gas, should be distributed efficiently for each BOP operation.

Consequently, the parametric study is performed under variation in fuel and air utilization in fuel cell, equivalence ratio of engine and effectiveness of each external reformer. In this study, the hybrid system is developed at a 5-kW power generation level. Thus, the fuel supply rate into the system and the specification of fuel cell and engine are fixed considering the power capacity. In addition, the engine operates at WOT condition and 1,800 RPM. The steam is fed into the

system at S/C ratio of 2.5 considering the coking issue [29-31]. The detailed operating condition for the system analysis is listed in Table 4.2.

Table 4.2 – Parameter variation range and reference condition

	Parameter	Range	Reference condition
Fuel cell	Fuel supply rate [kW]	-	8.311
	S/C ratio	-	2.5
	Fuel utilization [%]	55–80	70
	Air utilization [%]	20–60	40
	Operating temperature [°C]	-	750
Engine	Equivalence ratio	0.45–0.95	0.65
	Intake pressure [bar]	-	0.97±0.01 (WOT)
	Spark timing [CAD aTDC]	-	maximum work timing
	Engine speed [RPM]	-	1800
System design	Reforming proportion of each external reformer [ε]	0–0.85	to be determined in Section 4.4.1

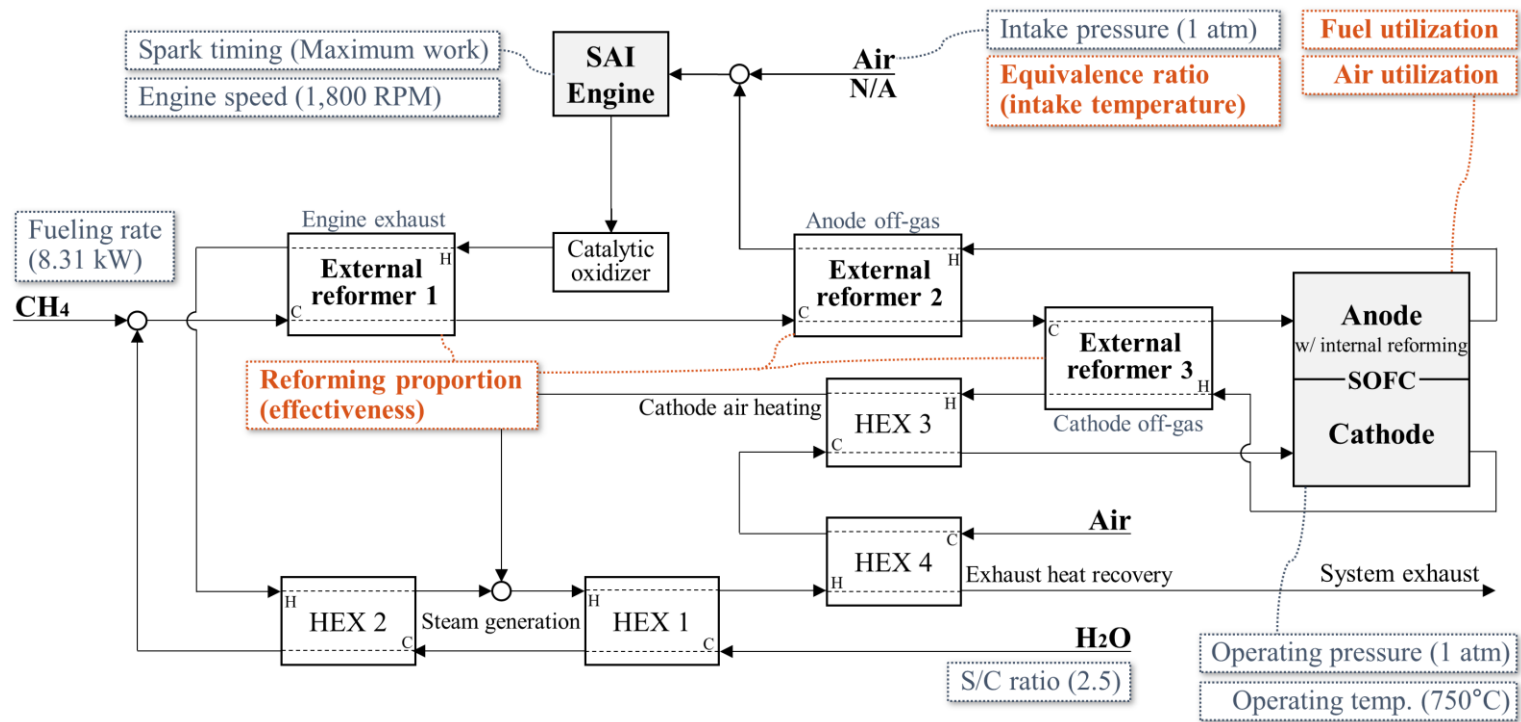


Figure 4.4 – Operating parameters of the SOFC-SAI engine hybrid system designed in Chapter 3

4.2.2. Engine experimental conditions

Figure 4.5 shows that the anode off-gas is a function of fuel supply rate, S/C ratio, operating temperature and fuel utilization in fuel cell, as described in Section 4.1.2.2. The anode off-gas state is independent of the external reforming, since the internal reforming occurs in the fuel cell which is assumed to operate at the equilibrium-state under isobaric and isothermal process. Thus, the anode off-gas is independent of the parameters related to the thermal energy distribution such as reforming proportion of each external reformer. Furthermore, air utilization in fuel cell is not related to the anode off-gas state, because the oxygen ions move into the anode as much as the current demand, regardless of the amount of air supplied to cathode. In addition, the fuel supply rate, S/C ratio and operating temperature of fuel cell are fixed at design conditions of the 5-kW class hybrid system. Consequently, the engine intake gas state is a function of the fuel utilization in fuel cell and equivalence ratio of engine and is independent of air utilization in fuel cell and reforming proportion of each external reformer. Hence, the engine performance in the hybrid system can be investigated in the 2-dimensional space that consists of fuel utilization in fuel cell and equivalence ratio of engine.

Here, it is noted that the intake temperature and the equivalence ratio of the ICE are dependent, as discussed in Figure 2.9. When the equivalence ratio is lowered, requiring more intake air in a given anode off-gas, intake temperature should decrease to satisfy the given intake pressure by the assumption (4) described in Section 4.1.1, since the flow rate of the intake gas into the engine is determined on a volume basis by the engine displacement and engine speed. Thus, the specific volume of anode off-gas should be reduced through heat transfer in

order to introduce more fresh air, which results in overall lower intake mixture temperature.

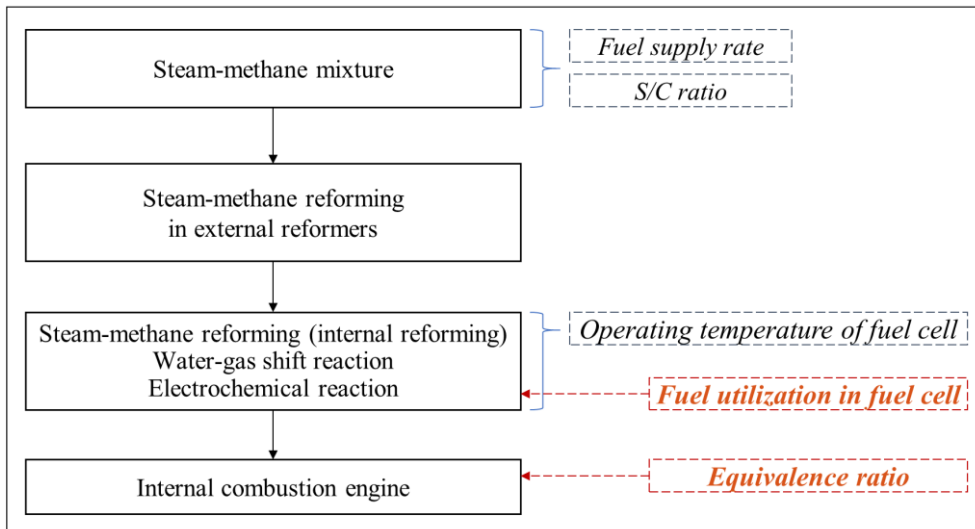


Figure 4.5 – Parameters affecting the engine intake condition

4.3. Engine experimental results under variation of fuel utilization and equivalence ratio

4.3.1. Intake gas

As described in Section 4.2, the engine experiments are performed in 2-dimensional space that consists of fuel utilization in fuel cell and equivalence ratio of engine. Figure 4.6(a) shows the anode off-gas composition calculated by fuel cell model described in Section 4.1. As the fuel utilization decreases, fuel fraction increases, and inert gas fraction decreases in anode off-gas. Thus, it is advantageous for the combustion in the engine in terms of load and composition. In the engine experiment, the flow rate of the estimated anode off-gas is controlled based on the calculation. Figure 4.6(b) shows the intake temperature which is measured at intake port. As described in Section 4.2, the intake temperature decreases when equivalence ratio decreases. Furthermore, as the fuel utilization decreases, the intake temperature decreases to satisfy the given intake pressure (~1 bar), because the more oxygen is required even at the same equivalence ratio due to fuel fraction increase. In the perspective of the system operation, it is important that the thermal energy which can be supplied from the anode off-gas increases if the engine can operate at the lower intake temperature as much as possible, as shown in Figure 4.6(c). Furthermore, it is likely to reduce heat loss during the engine operation. As noted by the white area in Figure 4.6(b) and Figure 4.6(c), some conditions are excluded from the experiment by the assumption (5) and the limitation (c), related to intake temperature and spark timing as described in Section 4.1.1.

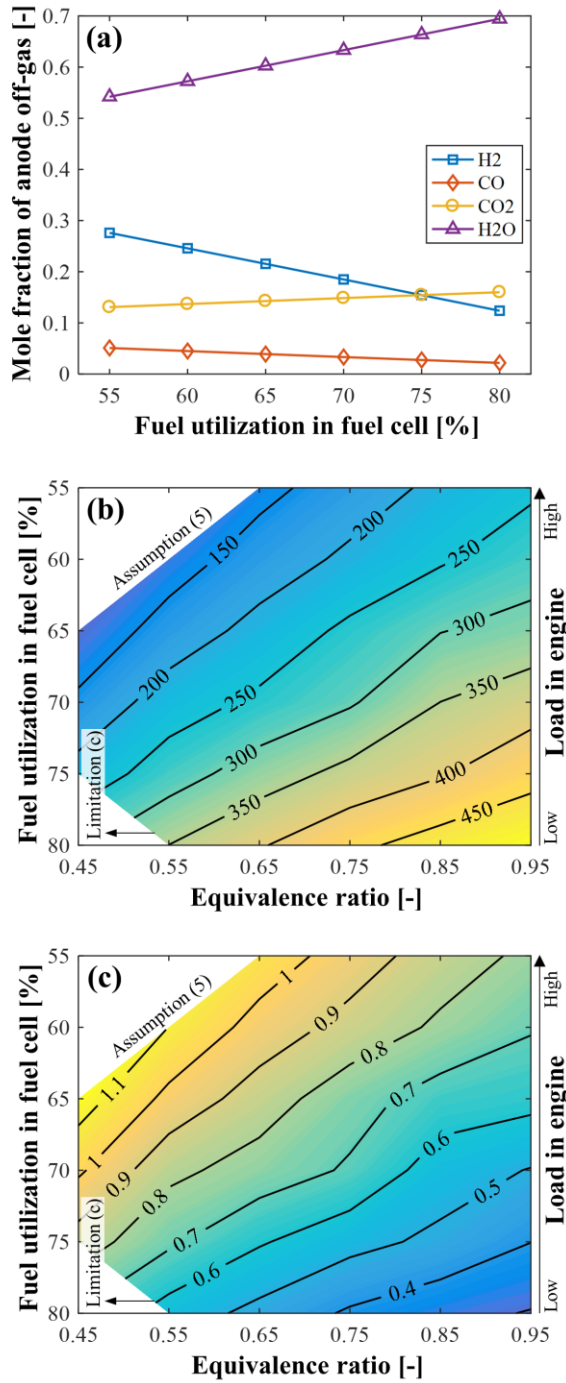


Figure 4.6 – Engine intake condition in experiment:
 (a) anode off-gas composition under variation of fuel utilization
 (b) intake temperature [°C] (c) available thermal energy of anode off-gas [kW]

4.3.2. Combustion characteristics

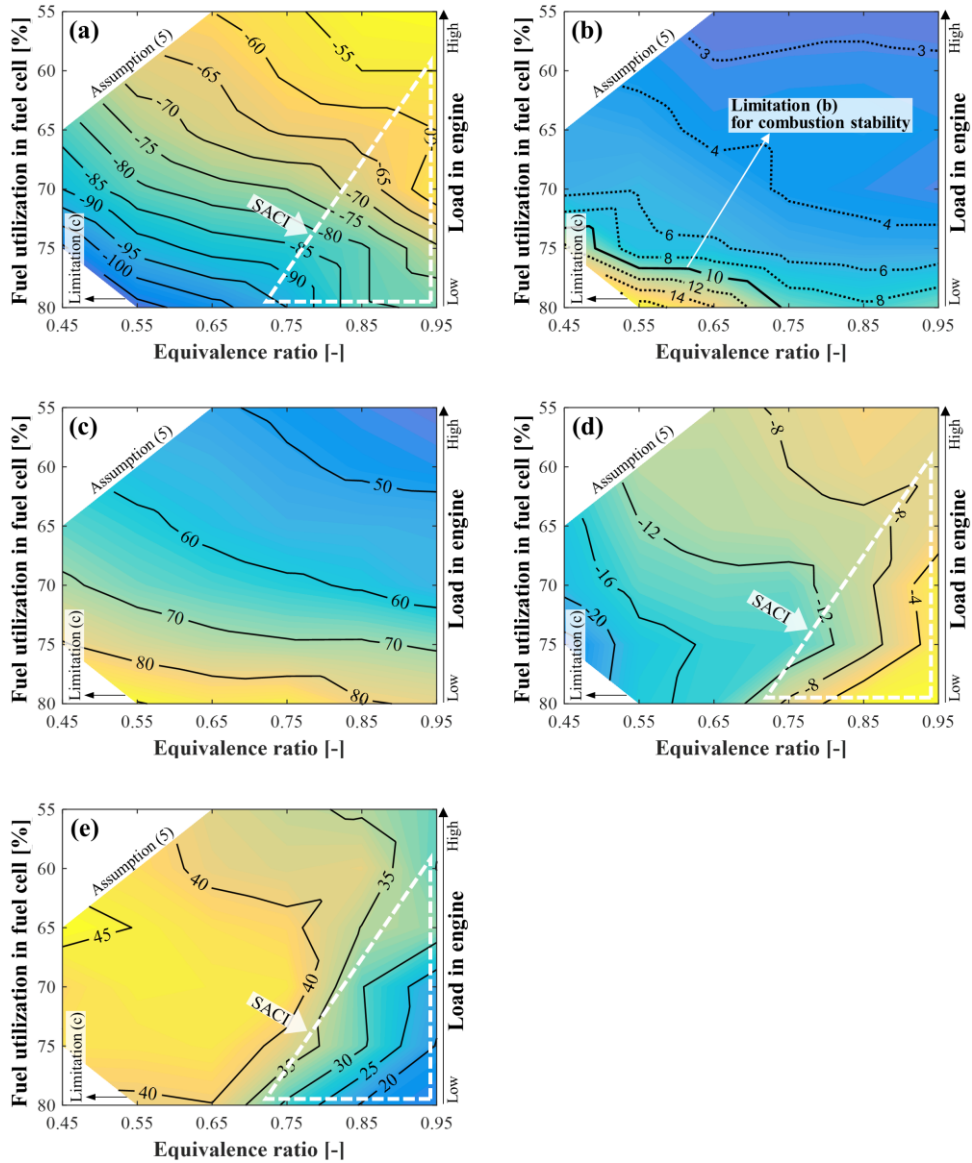


Figure 4.7 – Combustion characteristics:

(a) spark timing for maximum work [CAD aTDC] (b) COV(NMEP) [%] (c) time required for initial flame development (CA10–spark timing) [CAD] (d) CA10 [CAD aTDC] (e) combustion duration (CA90–CA10) [CAD]

Figure 4.7 represents the combustion characteristics of the intake gas ignited by a spark, i.e., spark-assisted ignition. The engine operates under low-load (low fuel fraction) and highly-diluted lean condition as the fuel utilization increases and the equivalence ratio decreases (lower left corner in the figure). It is an unfavorable direction for the flame propagation [35, 41]. Hence, spark timing for maximum work is advanced as shown in Figure 4.7(a). Furthermore, as it is close to flammability limit, the combustion stability represented by COV(NMEP) deteriorates as shown in Figure 4.7(b). Consequently, infeasible operating area of the engine is determined based on the limitation (b) described in Section 4.1.1.

In most operating area, the predictable effect of highly-diluted and fuel-lean condition on the initial flame development and the flame propagation is confirmed as shown in Figure 4.7(c)–(e). Especially, Figure 4.7(e) shows that combustion duration slightly decreases when the fuel utilization decreases and equivalence ratio increases. It is general behavior of the flame propagation. As fuel utilization decreases, inert gas fraction in anode off-gas decreases. Furthermore, as equivalence ratio increases, flame speed increases [35, 41]. Consequently, it leads to slightly reduced combustion duration.

It is noted that there is an area showing rather peculiar behavior than the aforementioned. In Figure 4.7(a), the trend of the spark timing changes in an area indicated by the triangular dotted line. In the area, the spark timing for maximum work is retarded rapidly. Although there is no significant difference in the tendency of the initial flame development as shown in Figure 4.7(c), the combustion duration is considerably reduced in the area as shown in Figure 4.7(e). It implies that the mean burning rate increases significantly during the main combustion, which may differ from flame propagation behavior of general SI at

the highly-diluted condition, as in the other operating conditions. It should be reminded that as shown in Figure 4.6(b), the intake temperature increases into this triangular region. This behavior is the characteristics of spark-assisted compression ignition (SACI) previously confirmed in Chapter 2 (Section 2.3.4) through using Livengood-Wu integral method.

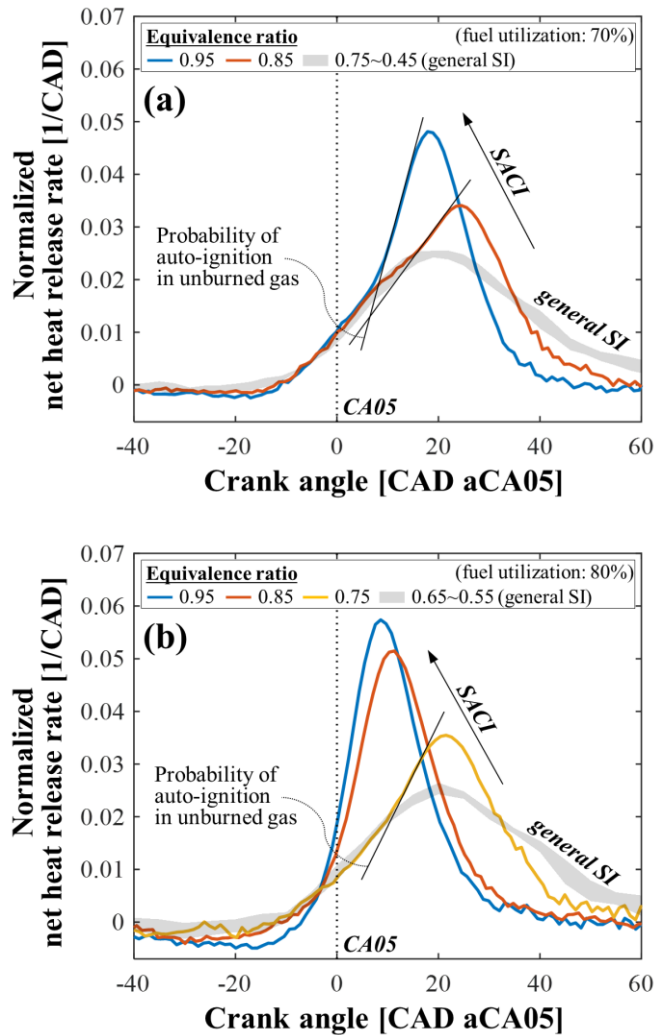


Figure 4.8 – Normalized net heat release rate profile from experimental data:
 (a) in the case that fuel utilization in fuel cell is 70%
 (b) in the case that fuel utilization in fuel cell is 80%

Figure 4.8 shows the SACI operating characteristics under variation of both fuel utilization and equivalence ratio through normalized NHRR profile of each operating condition, which can be interpreted as the relative burning speed [41]. In the case of 70% fuel utilization (left), the burning speed is rapidly increased when the equivalence ratio is over 0.75, since the auto-ignition occurs in unburned gas following initial flame propagation, mainly due to the overall higher in-cylinder temperature by the intake temperature increase. In SACI combustion, such auto-ignition behavior is known to be sensitive to the in-cylinder temperature [19]. Hence, as the intake temperature increases with increase in equivalence ratio (as shown in Figure 4.6(b)), the maximum and the slope of the normalized NHRR increase, and the timing of maximum normalized NHRR is advanced. If the intake temperature is lower than certain temperature, the combustion in engine has a common behavior of pure SI as shown in Figure 4.8, even with equivalence ratio and thus intake temperature variation. In the case of 80% fuel utilization in fuel cell, the auto-ignition timing in unburned gas is advanced and the equivalence ratio range where auto-ignition occurs increases compared to the case of 70% fuel utilization, because the intake temperature is overall higher than the 70% fuel utilization cases although it has more inert gas in anode off-gas. However, the anode off-gas at the lower fuel utilization is more favorable for auto-ignition under the same intake temperature, since it has less inert fraction and more fuel fraction. Hence, the minimum intake temperature required for SACI may decrease as the fuel utilization decreases.

In this hybrid system, the SACI area corresponds to the high fuel utilization or low-load engine operation. Thus, it is not as strong SACI as in typical standalone ICE operation. However, it is meaningful to expand the stable

operating area of the hybrid system with relatively faster burn rate than by pure flame propagation. Furthermore, it is confirmed that the engine operates without abnormal combustion such as knocking in all the engine operating condition of this study including the low fuel utilization (relatively high-load in engine) and SACI area, although the anode off-gas has H₂ as fuel composition and the intake gas temperature is higher than general gasoline-SI operation. It results from overall low-load and highly-diluted fuel-lean condition. For all the experimental condition, maximum pressure rise rate (MPRR) is under 0.6 MPa/ms, and ringing intensity is under 0.1 MW/m², i.e., moderate combustion behavior. In general, ringing intensity limit is ~4 MW/m² [48].

4.3.3. Power

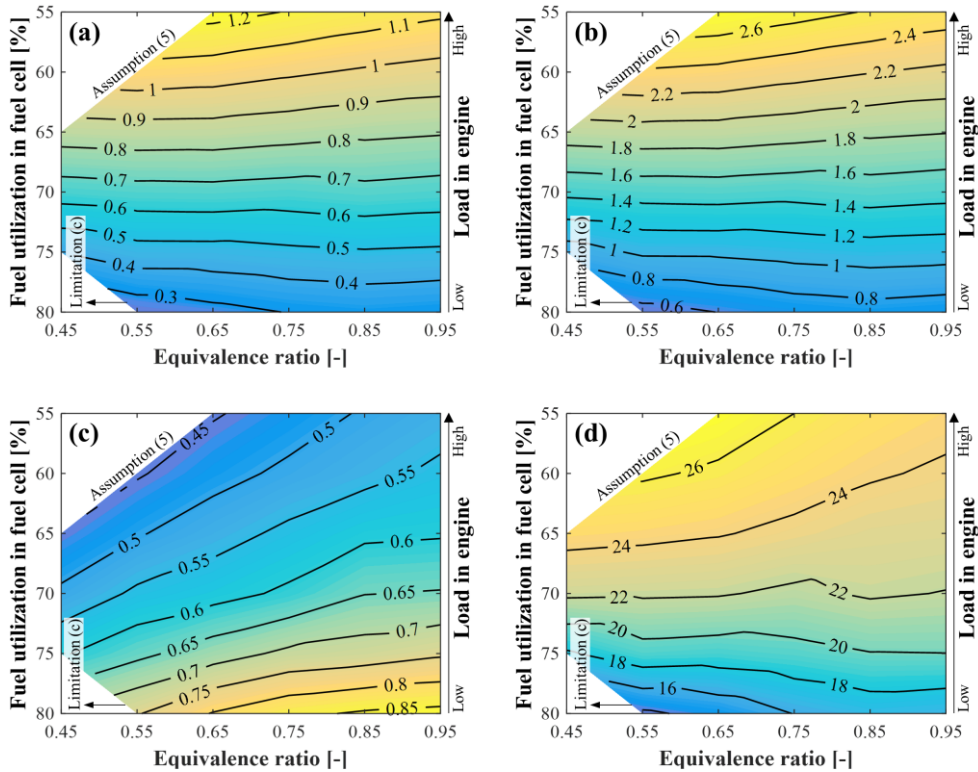


Figure 4.9 – Performance of engine:
 (a) net indicated work [kW] (b) NMEP [bar] (c) heat loss fraction based on LHV of anode off-gas [-] (d) thermal efficiency [%]

Figure 4.9 shows the engine performance. It operates in low-load condition that maximum NMEP is below ~ 2.7 bar in the tested area, since the anode off-gas is residual fuel after being used in fuel cell and, at the same time, the engine has low volumetric efficiency due to overall higher intake temperature than ambient.

The engine power is almost inversely proportional to the fuel utilization in fuel cell. However, in the case of high equivalence ratio, the tendency changes slightly under variation of the fuel utilization. It is mainly related to heat loss and

combustion mode. When the equivalence ratio increases at the low fuel utilization, heat loss fraction of the engine increases as shown in Figure 4.9(c), owing to high post-combustion temperature by high equivalence ratio and high intake temperature. It leads to loss of the engine power. On the other hand, when the equivalence ratio increases at the high fuel utilization, flame propagation speed increases or the combustion mode changes from SI to SACI as discussed in Figure 4.7. Furthermore, the change of heat loss fraction in engine is relatively small compared to that at the low fuel utilization conditions. As a result, the more power is produced.

However, increase in heat loss fraction means that the chemical energy of the fuel is not converted sufficiently into the power. Hence, as the fuel utilization increases, the thermal efficiency of the engine decreases as shown in Figure 4.9(d).

4.3.4. Exhaust gas

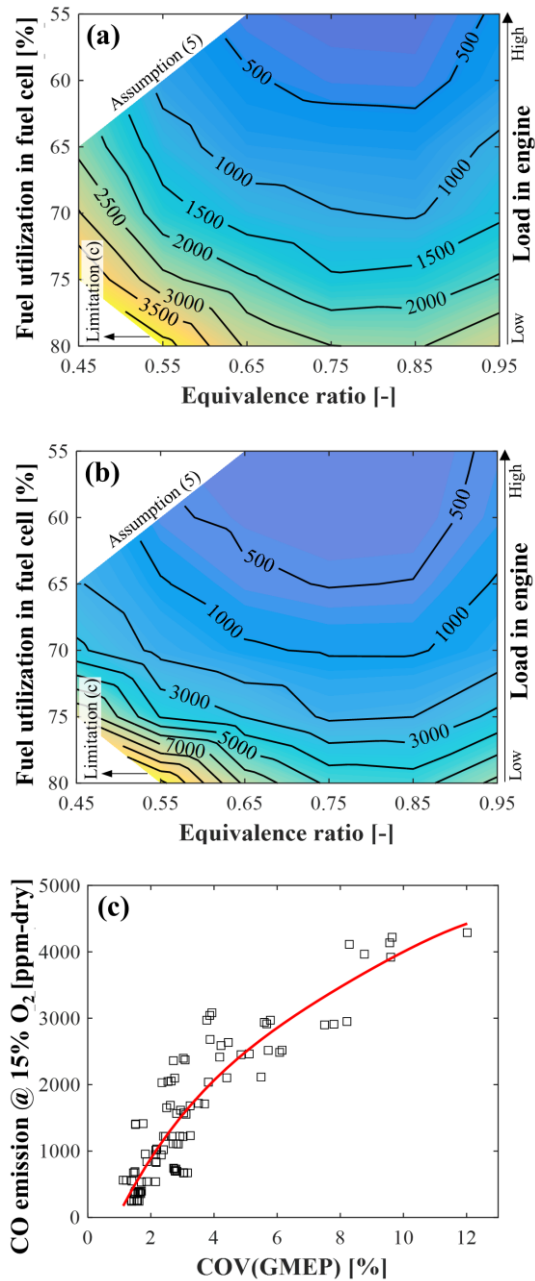


Figure 4.10 – Emissions:

(a) CO emission corrected to 15% O₂ [ppm-dry] (b) H₂ emission corrected to 15% O₂ [ppm-dry] (c) CO emissions and combustion stability (COV)

CO and H₂ emissions, corrected to 15% O₂ level, are shown in Figure 4.10(a)–(b). The emissions generally increase as the fuel utilization increases owing to low-load and highly-diluted condition. In the case that the equivalence ratio is lower than 0.75, the emissions increases since it is an unfavorable direction for the flame propagation [35, 41]. In the case that the equivalence ratio is higher than 0.75, the emissions may increase slightly due to local oxygen deficiency by inhomogeneity. The emission behavior under the equivalence ratio variation is similar to typical SI operation [41]. In general, it is likely that the emission behavior is related to the combustion stability as shown in Figure 4.10(c), since emissions and combustion instability have almost the same causes. NO_x emission is almost close to zero (< ~4 ppm corrected to 15% O₂ level) even in the region that the load and equivalence ratio are relatively high, since the maximum mean in-cylinder temperature (estimated) is lower than ~1700 K by highly-diluted mixture.

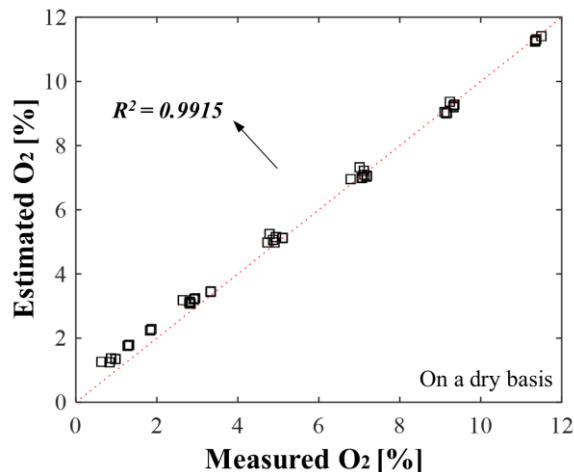


Figure 4.11 – Estimation accuracy of exhaust gas composition using emission measurement (CO and H₂)

The burned fraction of CO and H₂ is estimated using 3 species from the exhaust measurement data, i.e., CO, H₂ and O₂, and the following equations in Eqs. (4.1)–(4.3). There are two unknown quantities in Eqs. (4.2)–(4.3) derived from Eq. (4.1), i.e., burned fraction. As a result, the burned fraction of CO and H₂ can be estimated through finding the solution that satisfies both equations. Furthermore, the exhaust composition can be estimated using the solution for Eq. (4.1). In the next step, the measured O₂ fraction in the exhaust is used to confirm the estimation accuracy of the exhaust composition, through comparison with the estimated O₂ fraction by Eqs. (4.1)–(4.3). As shown in Figure 4.11, the exhaust composition is reliably estimated.

$$\begin{aligned}
& n_{H_2}H_2 + n_{CO}CO + n_{CO_2}CO_2 + n_{H_2O}H_2O + n_{O_2}(O_2 + 3.7619N_2) \rightarrow \\
& \quad n_{H_2}(1 - \eta_{burn,H_2})H_2 \quad + n_{CO}(1 - \eta_{burn,CO})CO \\
& \quad + (\eta_{burn,CO}n_{CO} + n_{CO_2})CO_2 + (\eta_{burn,H_2}n_{H_2} + n_{H_2O})H_2O \\
& \quad + (n_{O_2} - (\eta_{burn,H_2}n_{H_2} + \eta_{burn,CO}n_{CO})/2)O_2 \\
& \quad + 3.7619n_{O_2}N_2
\end{aligned} \tag{4.1}$$

$$\begin{aligned}
& x_{exhaust,CO,measured,dry} \\
& = \frac{n_{CO}(1 - \eta_{burn,CO})}{n_{H_2} + n_{CO} + n_{CO_2} + 4.7619n_{O_2} - \left(\frac{3\eta_{burn,H_2}n_{H_2} + \eta_{burn,CO}n_{CO}}{2}\right)}
\end{aligned} \tag{4.2}$$

$$\begin{aligned}
& x_{exhaust,H_2,measured,dry} \\
& = \frac{n_{H_2}(1 - \eta_{burn,H_2})}{n_{H_2} + n_{CO} + n_{CO_2} + 4.7619n_{O_2} - \left(\frac{3\eta_{burn,H_2}n_{H_2} + \eta_{burn,CO}n_{CO}}{2}\right)}
\end{aligned} \tag{4.3}$$

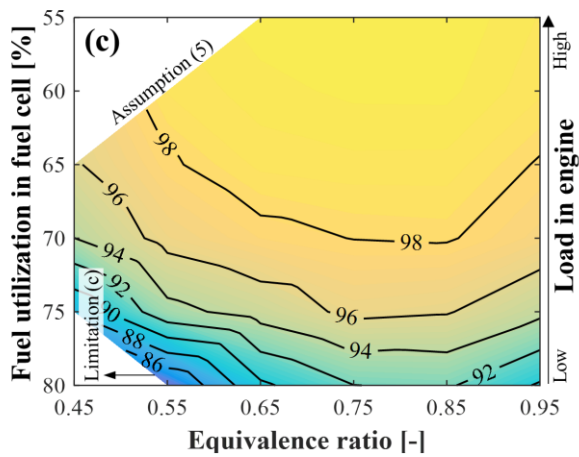
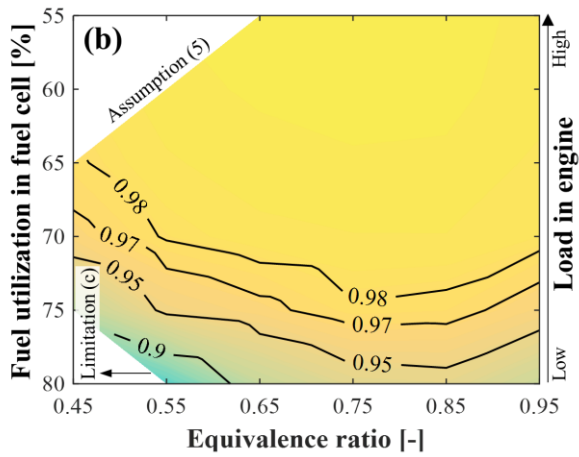
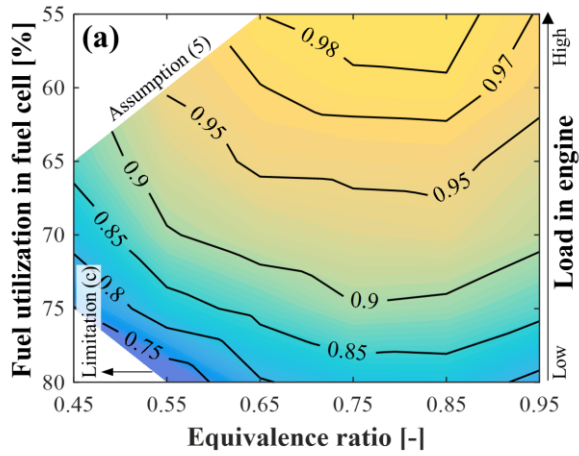


Figure 4.12 – Combustion efficiency estimated by exhaust measurement: (a) CO burned fraction [-] (b) H₂ burned fraction [-] (c) combustion efficiency [%]

Figure 4.12(a)–(b) shows the burned fraction of CO and H₂. H₂ has overall higher burned fraction than CO, because the H₂ has generally the higher oxidation rate than CO [55]. The combustion efficiency based on the LHV of intake gas controlled by MFC and estimated exhaust composition is shown in Figure 4.12(c). Despite of the anode off-gas combustion with a lot of dilution, it is confirmed that the combustion efficiency can be achieved over ~90% with sufficient thermal energy of intake gas, even at the high fuel utilization of 80% near the equivalence ratio of ~0.75.

In this study, a catalytic oxidizer is adopted for the after-treatment of the CO and H₂ emissions, i.e., combustion inefficiency. Since there is almost no NO_x emission, it is not necessary to operate at stoichiometric equivalence ratio for the after-treatment, unlike in a three-way catalytic converter of conventional SI engine. Furthermore, the conversion efficiency of CO emission is high when the equivalence ratio is below 1 [41]. Hence, the SAI engine in the hybrid system can be operated at lean-burn (air-rich) condition which has theoretically high efficiency. Furthermore, the available thermal energy of the anode off-gas increases as the equivalence ratio decreases as shown in Figure 4.6(c).

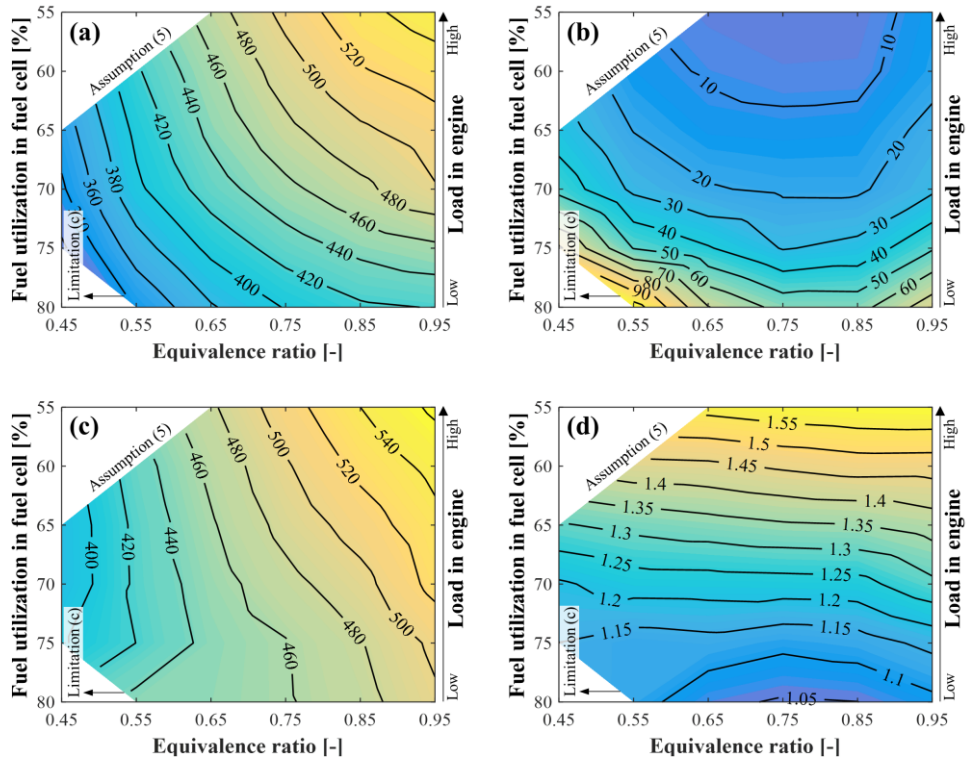


Figure 4.13 – Heat transfer quality of exhaust gas:
 (a) exhaust temperature [°C] (b) temperature increase through catalytic oxidizer [°C] (c) temperature after catalytic oxidizer [°C] (d) available thermal energy of exhaust [kW]

Figure 4.13(a) shows the exhaust temperature map which is an important information due to its effects on the system operation such as external reforming and steam generation. The exhaust temperature increases, as the post-combustion temperature rises by increase in load and equivalence ratio. Although intake temperature increases with higher fuel utilization, it is not reflected on the trend of exhaust temperature, mainly due to overall higher heat loss fraction.

The catalytic oxidizer converts the residual chemical energy, i.e., combustion inefficiency, into thermal energy while reducing the emission. Figure 4.13(b) shows the amount of temperature increase through the catalytic oxidizer. It is

proportional to the combustion inefficiency. Figure 4.13(c) shows the exhaust temperature after being increased through the catalytic oxidizer. Finally, since the mass flow rate of the exhaust increases as the equivalence ratio decreases, decrease in the exhaust temperature may be compensated. As a result, Figure 4.13(d) shows the available thermal energy of the exhaust satisfying the assumption (7) described in Section 4.1.1, which is almost a function of fuel utilization.

4.4. Effect of parameter variation on the system performance

4.4.1. Effectiveness of external reformers

In order to understand the optimal configuration for the best heat distribution, i.e., Case 1-3, the hybrid system performance is investigated under variation in reforming proportion of external reformer 1 and 3, as discussed in Section 3.2. Thus, in this section, operating conditions of the fuel cell and engine such as fuel utilization, air utilization and equivalence ratio are fixed at reference condition listed in Table 4.2.

As represented in Figure 4.14(a), it is clearly confirmed that both external reformer 1 and 3 should be used for the improved system efficiency. It means that the Case 2 proposed in Chapter 3 has the most efficient structure for heat distribution supplied to the external reforming.

If Case 3 is adopted where the external reformer 1 is not used (with effectiveness of external reformer 1 as zero), engine exhaust heat is only used for steam generation and its thermal energy is partially used, since the engine exhaust has more thermal energy than heat-supply required for the given steam state. It is confirmed in Figure 4.14(b), which shows that the effectiveness of HEX 2 decreases as the effectiveness of external reformer 1 is close to zero. If the effectiveness of external reformer 3 increases above certain level, anode inlet temperature becomes so high that the cathode inlet temperature cannot be matched to it due to the performance limit of HEX 3, or ‘cathode air heating limit’.

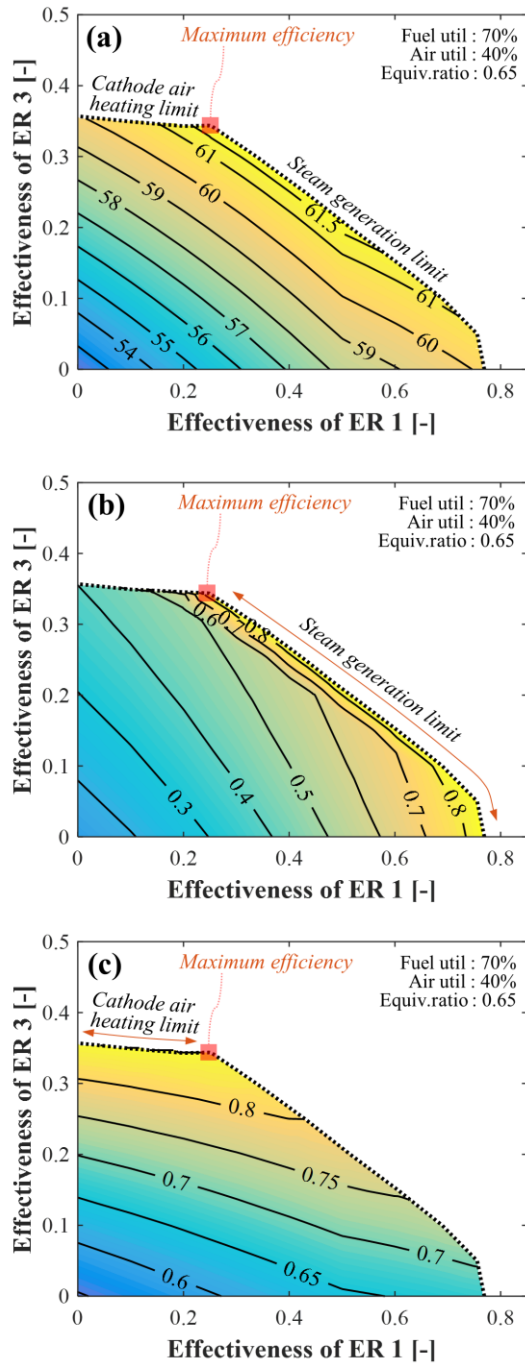


Figure 4.14 – System efficiency under effectiveness variation of external reformer 1 and 3:

(a) system efficiency [%] (b) effectiveness of HEX 2 for steam generation [-]

(c) effectiveness of HEX 3 for cathode air heating [-]

On the other hand, if Case 1 is adopted where the external reformer 3 is not used (with effectiveness of external reformer 3 as zero), the cathode off-gas heat is used inefficiently in HEX 3 as shown in Figure 4.14(c). When the effectiveness of the external reformer 1 increases in this configuration, there is certain highest limit or ‘steam generation limit’, where it is not possible to generate the desired steam at the HEX 2, since too much portion of engine exhaust gas enthalpy is already exploited in the external reformer 1.

Consequently, the hybrid system should be designed in the direction where thermal energy for the cathode air heating and the steam generation is supplied efficiently as much as possible. Furthermore, both external reformers should be adopted to use all the available thermal energy in the system.

In this regard, the Case 2 configuration demonstrates several advantages as follows. Firstly, the overall external reforming rate increases by ~5%p compared to the Case 1 and 3 as shown in Figure 4.15(a). The H₂ mole fraction of ~41% is achieved on a wet basis. Hence, it leads to reduction of voltage losses such as activation loss and concentration loss and increase of the Nernst voltage. As a result, the cell voltage increases over ~0.8 V as shown in Figure 4.15(b), and it results in the power increase. Secondly, the requirement for an additional heat-supply to satisfy the design operating temperature of fuel cell is reduced or eliminated, since the inlet temperature of fuel cell is increased as shown in Figure 4.15(c).

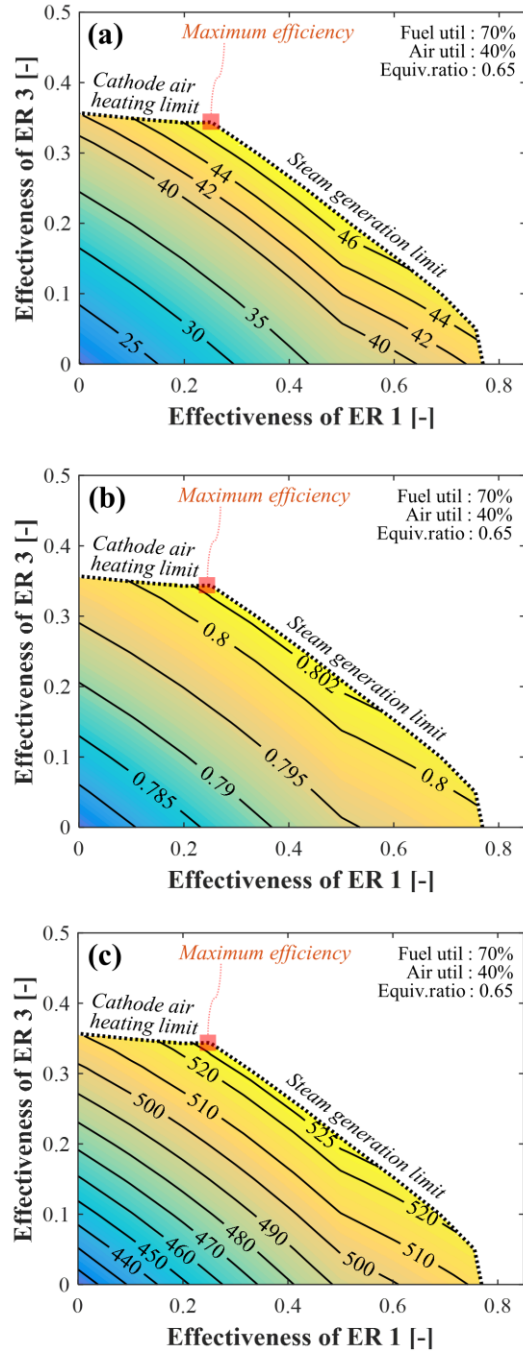


Figure 4.15 – Fuel cell operation under effectiveness variation of external reformer 1 and 3:

- (a) overall external reforming rate (methane conversion rate) [%]
- (b) cell voltage [V] (c) inlet temperature of fuel cell [°C]

4.4.2. Fuel utilization and equivalence ratio

As describe in Section 4.4.1, the Case 2 is selected as a new configuration design for the optimal thermal energy distribution in the hybrid system. Thus, the parametric study for operating conditions such as fuel and air utilization in fuel cell and equivalence ratio of engine is conducted based on the configuration of the Case 2. In this subsection, the system operating characteristics will be presented under variation of fuel utilization and equivalence ratio while other conditions are fixed at the reference condition listed in Table 4.2.

4.4.2.1. External reforming

The engine exhaust has enough thermal energy for the steam generation, when the fuel utilization decreases as shown in Figure 4.13(d). Hence, the reforming rate at external reformer 1 is increased as the fuel utilization is reduced in Figure 4.16(a). Its reforming rate is overall lower than that of the external reformer 2, because the engine exhaust heat should also be used for steam generation. Since the available thermal energy of anode off-gas is increased as the fuel utilization and the equivalence ratio are both decreased as shown in Figure 4.6(c), the reforming rate of external reformer 2 is also increased Figure 4.16(b). However, at the low fuel utilization, a part of the anode off-gas heat is not transferred to the cold gas reformed partially in external reformer 1, due to the decreased temperature difference and performance limit of heat exchanger. The reforming rate of external reformer 3 increases as the fuel utilization increases, owing to the increase in the cathode off-gas heat caused by the increase in mass flow rate even at the same air utilization. As a result, the heat-supply for the external reforming is high at the low fuel utilization and low equivalence ratio.

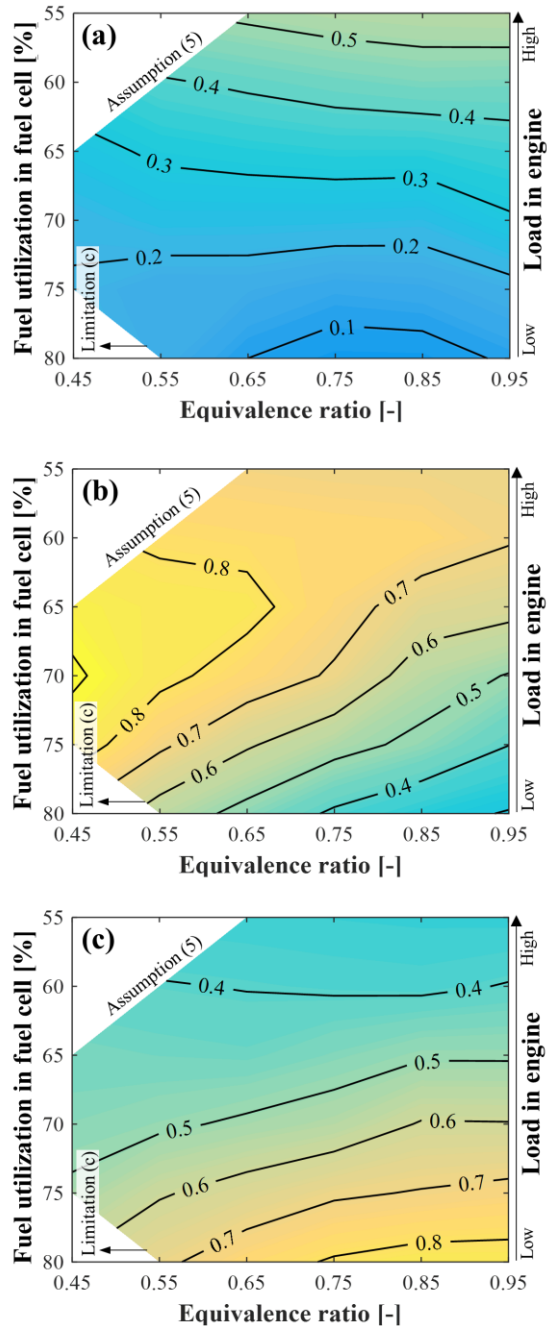


Figure 4.16 – Heat-supply used for external reforming under variation of fuel utilization and equivalence ratio: (a) external reformer 1 using engine exhaust heat [kW] (b) external reformer 2 using anode off-gas heat [kW] (c) external reformer 3 using cathode off-gas heat [kW]

4.4.2.2. Fuel cell operation

Although external reforming rate, i.e., H_2 yields, is affected by both fuel utilization and equivalence ratio as shown in Figure 4.17(a), the change under the variation of equivalence ratio is relatively small. As the fuel utilization decreases, the cell voltage increases due to increase of H_2 fraction in the anode inlet gas and decrease in ohmic loss by decreased current density. Since it is mainly caused by decrease in ohmic loss, the cell voltage would be less sensitive to the equivalence ratio of engine as compared to the fuel utilization in fuel cell, as shown in Figure 4.17(b). In terms of thermally self-sustainable operation, there is an infeasible region that the additional heat is required for maintaining the design operating temperature of fuel cell as represented in Figure 4.17(c). Although the available thermal energy of anode off-gas and engine exhaust is increased when the equivalence ratio and fuel utilization are both decreased as shown in Figure 4.6(c) and Figure 4.13(d), more heat is produced in the stack when the fuel utilization increases, since the electrochemical reaction is exothermic reaction. Furthermore, the amount of cathode off-gas heat to be supplied for the BOP operation increases due to increase in flow rate even at the same air utilization. As a result, as the fuel utilization increases and the equivalence ratio decreases, it is favorable for the thermally self-sustainable operation. The feasible area is represented as the limitation (a), or positive heat transfer values in Figure 4.17(c), which operates at the design operating temperature without additional heat-supply.

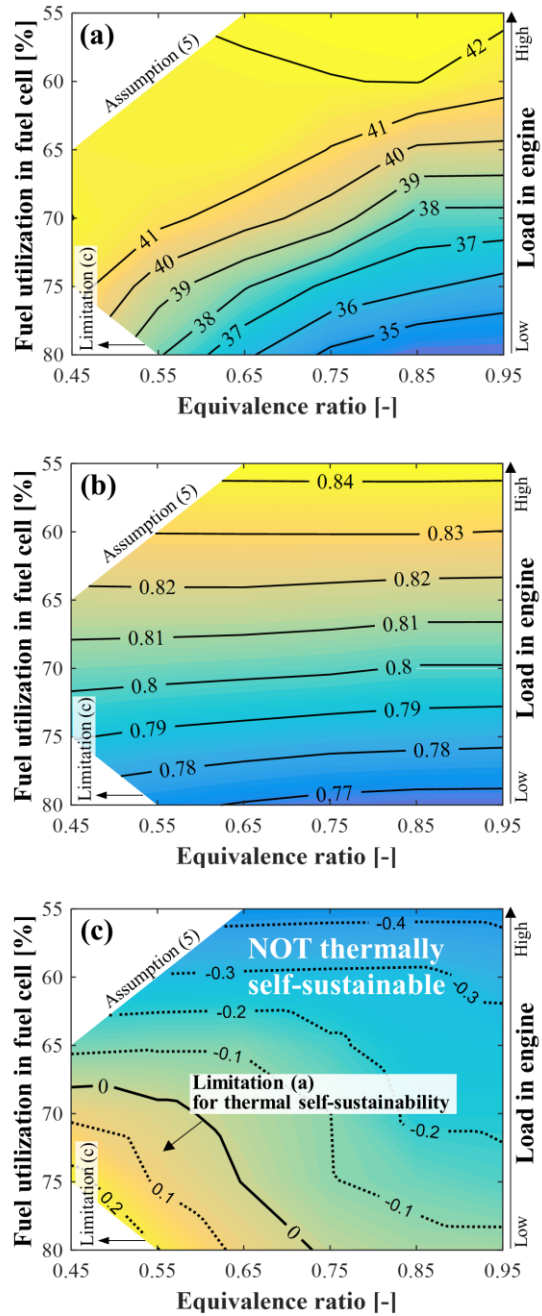


Figure 4.17 – Fuel cell performance under variation of fuel utilization and equivalence ratio: (a) H₂ mole fraction in the anode inlet gas on a wet basis [%] (b) cell voltage [V] (c) heat transfer from fuel cell to the environment for satisfying the operating temperature [kW]

4.4.2.3. System performance

The fuel cell power is predominantly a function of fuel utilization as shown in Figure 4.18(a), since the cell voltage is less sensitive to the variation of equivalence ratio as described above. Figure 4.18(b) shows that the fuel cell efficiency decreases as the fuel utilization increases, due to increase in the voltage losses, e.g., ohmic loss by current density increase. Furthermore, the efficiency decreases if the additional heat-supply is required for the operating temperature. Here, the fuel cell efficiency is calculated including the additional heat-supply when it is required, which is defined as Eq. (4.4) considering the amount of LHV in/outlet at the fuel cell.

$$\eta_{Fuelcell} = \frac{W_{indicated,Fuelcell}}{(LHV_{an,in} - LHV_{an,out}) + Q_{heat,in}} \quad (4.4)$$

Unlike the fuel cell power, the engine power is slightly affected by the equivalence ratio as described in Section 4.3.3. Thus, the system power slightly increases as equivalence ratio decreases under the low fuel utilization. In the case of high fuel utilization, the system power decreases as equivalence ratio decreases, as shown in Figure 4.18(c). In terms of fuel utilization, the system power increases as the fuel utilization increases, since the fuel cell efficiency is overall higher than the efficiency of engine. However, the system power may have an optimum of fuel utilization, because the efficiency of the fuel cell and engine are both reduced as the fuel utilization increases, as shown in Figure 4.9(d) and Figure 4.18(b). Finally, the system efficiency is depicted in Figure 4.18(d). Even if the fuel cell is operated at the lower temperature for reducing the additional heat-supply, the fuel cell efficiency is decreased due to increase in losses by the lower operating temperature.

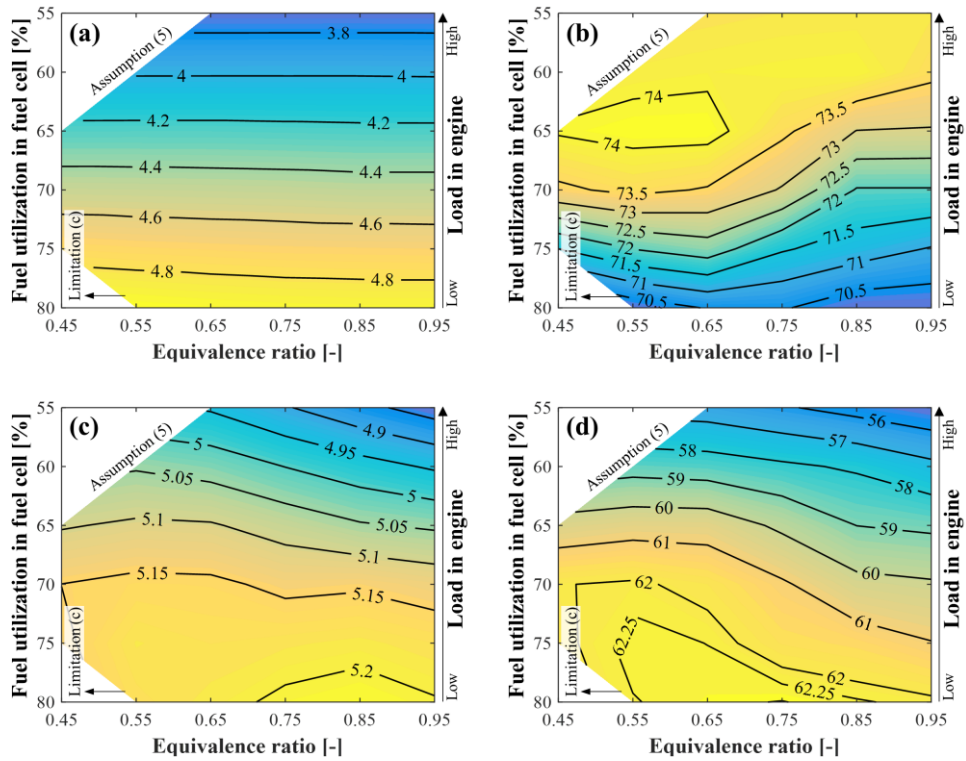


Figure 4.18 – System performance under variation of fuel utilization and equivalence ratio: (a) fuel cell power [kW] (b) thermal efficiency of fuel cell [%] (c) hybrid system power [kW] (d) hybrid system efficiency [%]

4.4.3. Fuel utilization and air utilization

In this section, the system operating characteristics will be presented under the variation of fuel and air utilization of the fuel cell stack, while the other conditions are fixed at the reference condition listed in Table 4.2.

4.4.3.1. External reforming

The available thermal energy of the engine exhaust increases as the fuel utilization reduces, while it should be used both for external reforming and steam generation. In the meantime, when the mass flow rate of cathode off-gas is increased under low air utilization, the capability of cathode off-gas for steam generation is increased. This latter fact helps to increase the engine exhaust heat supplied to the external reformer 1. Thus, the reforming rate at the external reformer 1 increases as the air utilization and the fuel utilization are both decreased. However, as the reforming rate at the external reformer 1 increases, the temperature difference (state 3 and 5) for heat exchange in external reformer 2 decreases. It results in losses of available thermal energy of anode off-gas. Hence, the reforming rate at the external reformer 2 is almost saturated as both fuel utilization and air utilization decrease, although available thermal energy of anode off-gas is independent from air utilization. In the external reformer 3, the reforming rate is increased as the fuel utilization increases and air utilization decreases, due to increase in the mass flow rate of cathode off-gas. As a result, the effect of the air utilization on the total reforming rate is significant, and the total reforming rate is high at the low air utilization.

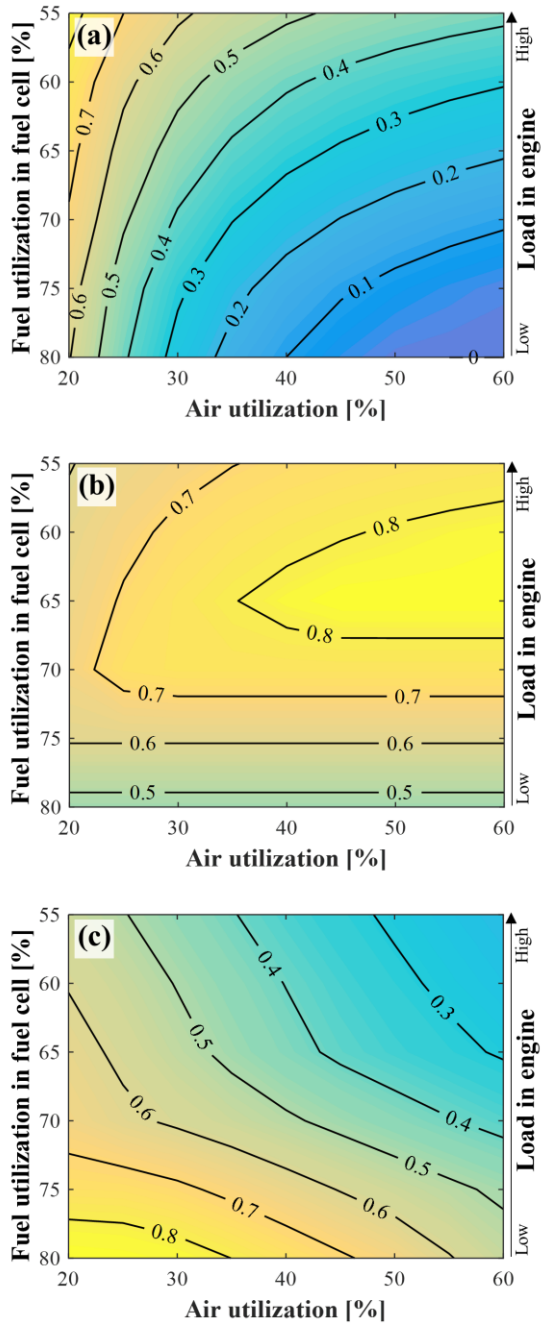


Figure 4.19 – Heat-supply used for external reforming under variation of fuel utilization and air utilization: (a) external reformer 1 using engine exhaust heat [kW] (b) external reformer 2 using anode off-gas heat [kW] (c) external reformer 3 using cathode off-gas heat [kW]

4.4.3.2. Fuel cell operation

Figure 4.20(a) shows the H₂ yields by external reforming. It is the lowest at the high fuel utilization and high air utilization due to insufficient thermal energy for the steam generation as described above. Since the air utilization has the considerable effect on the external reforming, there is a meaningful difference in H₂ fraction under the variation of air utilization. Furthermore, the O₂ fraction in cathode off-gas increases from ~10% to ~18% as the air utilization reduces from 60% to 20%. It leads to decrease in voltage losses in the fuel cell. Furthermore, since the current density is relatively low at low fuel utilization, the cell voltage increases with fuel utilization, as shown in Figure 4.20(b). In terms of the thermally self-sustainable operation, it also has an infeasible operating region under the variation of air utilization. In this region, the additional heat is required for satisfying the design operating temperature of fuel cell, which is represented as the negative value in Figure 4.20(c). Although the anode/cathode inlet temperature which is equivalent with the overall reforming rate is increased when the air utilization decreases as confirmed in Figure 4.20(a), the cooling effect of the cathode air is increased due to increase in the mass flow rate. Hence, decrease in the air utilization makes it difficult to satisfy the design operating temperature of fuel cell. In addition, when the fuel utilization decreases, it is also difficult because the exothermic electrochemical reaction is reduced. Consequently, it is not feasible to operate the fuel cell self-sustainably at the given design operating temperature under low fuel utilization and low air utilization.

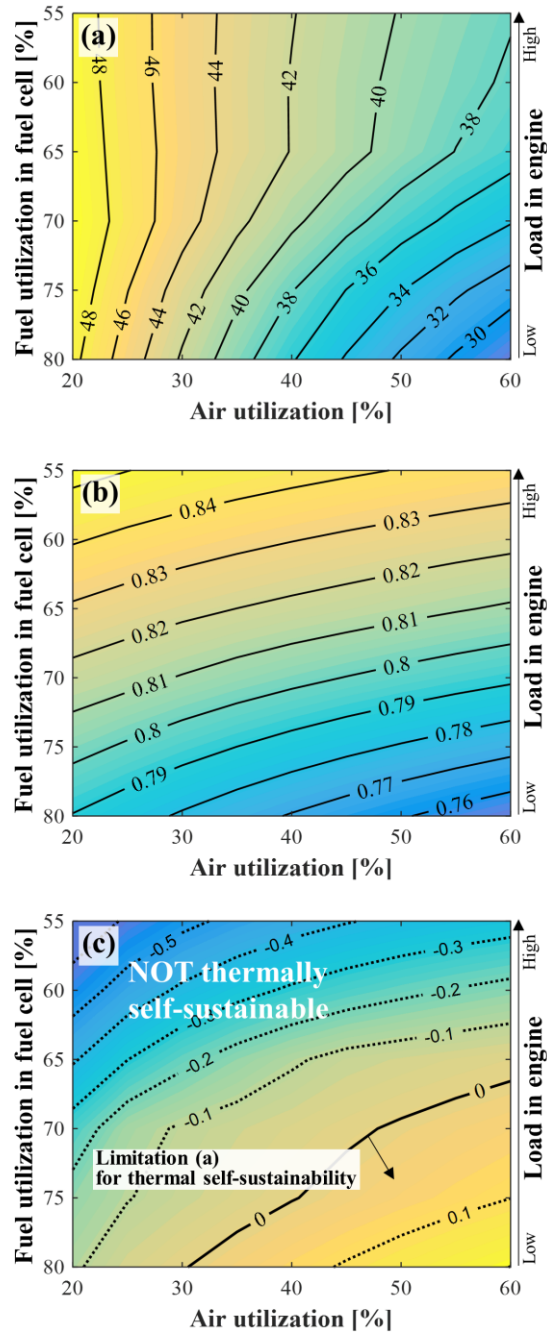


Figure 4.20 – Fuel cell performance under variation of fuel utilization and air utilization: (a) H₂ mole fraction in the anode inlet gas on a wet basis [%] (b) cell voltage [V] (c) heat transfer from fuel cell to the environment for satisfying the operating temperature [kW]

4.4.3.3. System performance

Figure 4.21(a) shows the fuel cell power, which is essentially a function of the fuel utilization. However, the increase in cell voltage by reduced air utilization results in the fuel cell power increase, especially at the high fuel utilization.

Figure 4.21(b) shows the fuel cell efficiency which has different tendency from that of the cell voltage. Under the same current density condition, i.e., same fuel utilization, as air utilization increases, decrease in the cell voltage by the reduced external reforming rate and oxygen fraction leads to a decrease in the absolute power. However, if the fuel cell is capable of generating power by using more available energy than the incoming energy through internal reforming while maintaining the operating temperature without additional heat-supply, the fuel cell efficiency defined as Eq. (4.4) can be better even though the absolute power is lower. It is considerably important to maintain the operating temperature, because the internal reforming is an endothermic reaction. If not, the fuel cell efficiency decreases, due to additional heat required for the design operating temperature or decrease in the operating temperature. Furthermore, especially at the low air utilization, the fuel cell efficiency is decreased rapidly due to the cooling effect of cathode air which has large mass flow rate. Consequently, it is important that select the appropriate air utilization for the fuel cell operation.

Figure 4.21(c) shows the overall system power. The thermal efficiency of engine decreases, as the fuel utilization increases. It results in the tendency of the system power different from that of the fuel cell power at the high fuel utilization. As a result, the system efficiency is calculated as Figure 4.21(d) considering the additional heat-supply required for the design operating temperature represented

in Figure 4.20(c).

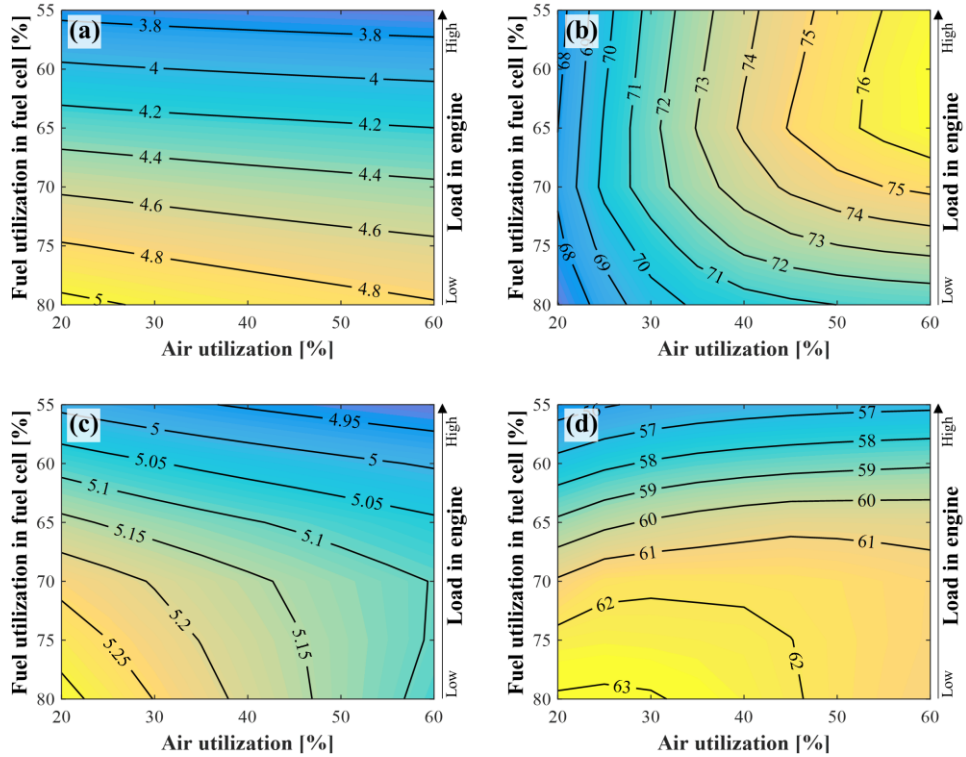


Figure 4.21 – System performance under variation of fuel utilization and air utilization: (a) fuel cell power [kW] (b) thermal efficiency of fuel cell [%] (c) hybrid system power [kW] (d) hybrid system efficiency [%]

Chapter 5. Optimization of operating conditions for SOFC-SAI engine hybrid system

5.1. Methodology for optimization

5.1.1. Design of experiment

Since the hybrid system is affected by a number of operating parameters as shown in Figure 4.4, it could show complicated non-linear behavior along parametric variations. Hence, a design of experiment (DOE) is performed to analyze the operating characteristics and to optimize the operating conditions for improved system efficiency. For the DOE, n-level full factorial design is used to understand the hybrid system behavior clearly and to obtain the accurate response surface on multi-dimensional space. In this study, the observation data for the DOE are the system performance results calculated by the system-level analysis described in Section 4.1.2.

5.1.2. Response surface method

Response surface is a fitted model based on the observation data, and represents the system behavior. In this study, multiple linear regression model is used for the response surface as provided in Eq. (5.1) [56]. The variable y represents the observation data. β is called the regression coefficients which represents the slope with respect to x on the response surface. The variable x is the regressor variable, not the operating parameter of the system. Thus, k represents the number of regressor variables in the model, not the number of operating parameters of the system. For example, newly defined x_1x_2 represents

an interaction behavior between x_1 and x_2 which are operating parameters. The variable ε represents error or residual. In addition, coded variable which spanning from -1 to 1 is used for each regressor variable x .

$$y = \beta_0 + \sum_{j=1}^k \beta_j x_j + \varepsilon \quad (5.1)$$

$$\begin{aligned} y &= \beta_0 + \beta_1 x_1 + \beta_2 x_2 + \beta_{11} x_1^2 + \beta_{22} x_2^2 + \beta_{12} x_1 x_2 + \varepsilon \\ &= \beta_0 + \beta_1 x_1 + \beta_2 x_2 + \beta_3 x_3 + \beta_4 x_4 + \beta_5 x_5 + \varepsilon \end{aligned} \quad (5.2)$$

In general, least squares method (LSM) is used to determine the regression coefficients that minimize the sum of the square of the errors [56]. By the LSM, the least squares estimator of β , i.e., b , is described in Eq. (5.3).

$$b = [X'X]^{-1}X'y \quad (5.3)$$

As a result, the response surface for the system is obtained as Eq. (5.4).

$$\hat{y} = Xb \quad (5.4)$$

In this study, the response surface is used for optimization of operating conditions in multi-dimensional space by MATLAB built-in function.

5.2. Optimization results

5.2.1. Design of experiment and response surface

5.2.1.1. Variables of DOE

As described in Section 4.2, there are a lot of operating parameters in the hybrid system. However, it is confirmed in Section 4.4 that the reforming proportion of each reformer clearly has one direction for improving the system efficiency, i.e., all the external reformers are necessary. Hence, the optimization for the fuel utilization, air utilization in fuel cell and equivalence ratio of engine is performed in the configuration of the Case 2 discussed in Chapter 3.

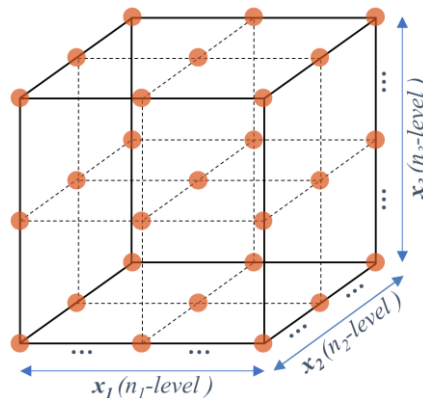


Figure 5.1 – Multi-level and full factorial design

Since the dynamics of the hybrid system is considerably complicated and is predicted to have a non-linear behavior than second-order as confirmed in Section 4.4, the response surface is developed based on full cubic form with interaction term considering the complicated behavior, and n-level full factorial design is used for the DOE to improve the model accuracy. A total of 288 DOE cases from the system-level simulation based on 32 engine experimental data performed under variation of fuel utilization and equivalence ratio are used for

the development of the response surface, as listed in Table 5.1.

Table 5.1 – Variable selection for response surface and optimization

	Variable	Range	Step	Coded variable
Fuel cell	Fuel utilization [%]	55–80	5	x_2
	Air utilization [%]	20–60	5	x_3
Engine	Equivalence ratio [-]	0.45–0.95	0.1	x_1

5.2.1.2. Response surface and constraint surfaces

The hybrid system efficiency, which is a main objective function of the response surface, is predicted accurately as shown in Figure 5.2(a). Thus, the response surface is used for the optimization in 3-dimensional space. However, the feasible region is limited by two constraint surfaces as shown in Figure 5.2(b), which are related to the engine combustion stability and thermally self-sustainable operation described in Section 4.3 and Section 4.4. Hence, the constraint surfaces should be considered for the optimization problem. The form of non-linear inequality constraints is provided in the following equation. The constraint for combustion stability is represented as Eq. (5.5). The air utilization is excluded in Eq. (5.5), since it does not affect the engine operation. The inequality equation is fitted in a cubic form based on the engine experimental data. Another constraint for the thermal self-sustainability is represented as Eq. (5.6) which is fitted in 4th-order form based on the observation data by MATLAB built-in function.

$$x_2 - f(x_1) < 0 \quad (5.5)$$

$$f(x_1, x_2) - x_3 < 0 \quad (5.6)$$

Figure 5.2(c) shows the response surface and the constraint surfaces on 2-dimensional space with fuel utilization fixed at 75%, which is developed through the process described above. The detailed equation of the response surface is provided in Appendix D. In order to find the optimal operating point, MATLAB built-in function (fmincon) and the response surface equation are used with considering the non-linear inequality constraints.

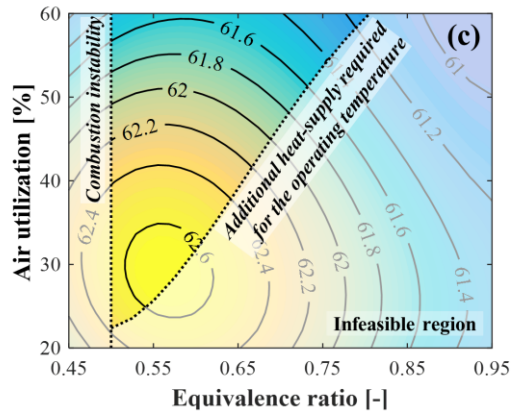
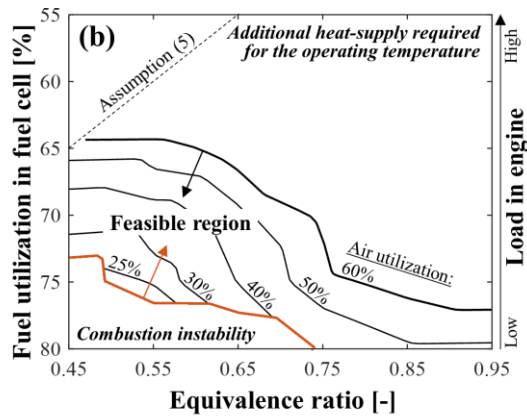
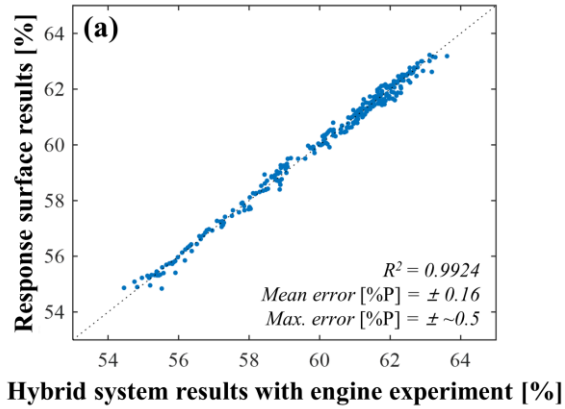


Figure 5.2 – Response surface and constraint surfaces of the hybrid system:
(a) accuracy of the response surface for hybrid system efficiency
(b) feasible region from the observation data for the combustion stability and thermal self-sustainable operation maintaining the design operating temperature
(c) response surface and constraint surfaces in the case that fuel utilization is 75%

5.2.2. Performance at design/off-design operation

5.2.2.1. Fuel cell and engine operation

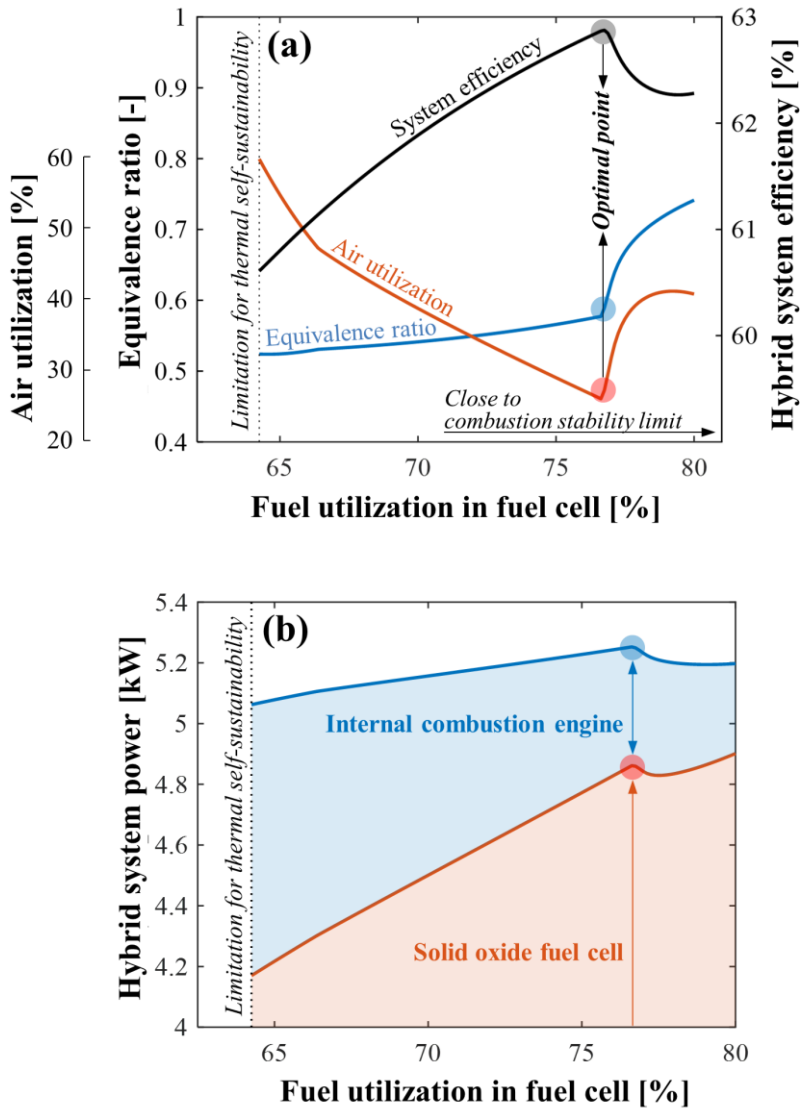


Figure 5.3 – Optimization results under the variation of fuel utilization:
(a) optimal operating condition of air utilization and equivalence ratio
(b) power generation of the fuel cell and the engine at optimal condition

The optimal air supply for the fuel cell and the engine under the variation of fuel utilization, is presented in Figure 5.3(a). As the fuel utilization increases, exothermic electrochemical reaction is increased. Thus, more air can be or should be supplied to the cathode for maintaining the design operating temperature as shown in Figure 5.3(a), because the cathode air has a cooling effect. This also leads to the increase in cell voltage due to the oxygen fraction increase in the cathode. Furthermore, the increase in the thermal energy of cathode off-gas, i.e., increase in mass flow rate, results in the inlet temperature increase and high H_2 yields by increase in overall external reforming rate as discussed in Figure 4.20(a). Since these all positively affect the system efficiency, air utilization should be decreased for the optimal operation as fuel utilization increases, up to the point where it doesn't affect thermally self-sustainable operation. In terms of the equivalence ratio of the engine intake, the overall low equivalence ratio is favorable for the system operation, since the engine intake temperature requirement reduces and thus available thermal energy of anode off-gas increases. The heat loss of engine also decreases as the intake temperature decreases. However, the combustion efficiency is deteriorated at the extremely low equivalence ratio as fuel utilization increases. Hence, the optimal equivalence ratio slightly rises as the fuel utilization increases, which is in a direction to improved thermal efficiency of the engine as discussed in Figure 4.9(d).

If the fuel utilization is further increased above ~77% (optimal point), the equivalence ratio should rapidly increase to prevent combustion instability. It is unfavorable conditions for the thermally self-sustainable operation, as mentioned in Figure 4.17(c). Therefore, the air utilization should be increased to reduce the cooling effect by the unused air. These are the reasons for the decrease in the

hybrid system efficiency at high fuel utilization, since it leads to decrease in O_2 fraction at cathode and available thermal energy of anode/cathode off-gas which results in decrease in overall external reforming rate.

Finally, as shown in Figure 5.3(b), it is confirmed that the system efficiency is increased through the addition of the SAI engine by 4–11%p on a LHV basis of system fuel, and power generation share of the SAI engine is 6–18%, under variation of the fuel utilization tested.

5.2.2.2. BOP operation

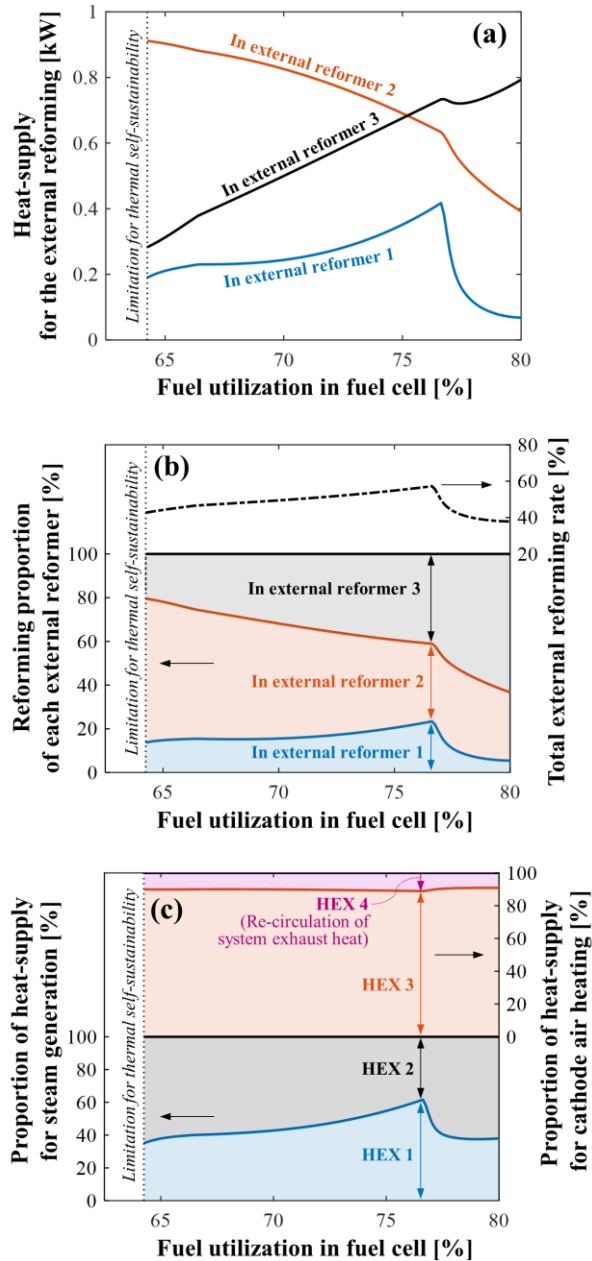


Figure 5.4 – BOP operation under optimal operating conditions: (a) heat-supply for the external reforming (b) reforming proportion of each external reformer and external reforming rate (c) heat-supply proportion of each BOP for the steam generation and the cathode air heating

Figure 5.4 indicates the BOP operation for the optimal operating conditions provided in Figure 5.3, which is investigated by substituting the optimal operating conditions into the response surface. Since the optimal equivalence ratio has no significant change in the range where the fuel utilization is lower than its optimal value, BOP operation is mainly affected by the fuel utilization and air utilization. As the fuel utilization increases with decrease in the air utilization, the amount of the cathode off-gas heat supplied to generate steam is increased due to increase in the mass flow rate of cathode off-gas. It enables more engine exhaust heat that can be supplied to the external reformer 1, although the overall exhaust heat is reduced with higher fuel utilization in the fuel cell, as shown in Figure 4.13(d). In the external reformer 2, the reforming rate is decreased, due to the decrease in the available thermal energy of anode off-gas with increase in the fuel utilization, as discussed in Figure 4.6(c). In addition, the reforming rate is affected by the air utilization, especially at the low fuel utilization as shown in Figure 4.19(b). Hence, the reforming proportion of external reformer 2 is reduced as the fuel utilization increases. In the external reformer 3, the increase in thermal capacity of cathode off-gas by increased mass flow rate leads to increase in the reforming rate as shown in Figure 4.19(c). Thus, its reforming proportion is also increased.

If the fuel utilization is higher than the optimum value, the equivalence ratio and the air utilization should be both increased. It implies that the heat of the engine exhaust and the cathode off-gas is insufficient for the external reforming and steam generation, as described in Figure 4.13(d) and Figure 4.19(a). Hence, the reforming proportion of the external reformer 1 is decreased rapidly with the increase of the air utilization as shown in Figure 4.19(a) for sufficient heat-supply

for steam generation. In the external reformer 2, it has large temperature gradient between state 3 and state 5, for the available thermal energy of anode off-gas to be fully used, since the reforming rate in the external reformer 1 is considerably low. However, now the limiting factor for the available thermal energy of anode off-gas is the high engine intake temperature required for the operation with increased equivalence ratio and fuel utilization. In the end, it leads to the decrease in reforming rate of the external reformer 2. In the external reformer 3, the cathode off-gas heat supplied for the external reforming is also decreased slightly due to rapid increase of the air utilization. However, after the air utilization is settled near ~40%, the heat-supply into the external reformer 3 increases again due to the increased cathode flow rate with the increase in fuel utilization.

Consequently, as the air utilization is decreased with the increase of fuel utilization under the optimal point, the total external reforming rate is increased, as shown in Figure 5.4(b). As explained in the previous paragraphs, it results from the reforming rate increase in the external reformer 1 and 3 with the air utilization decrease. However, under the operating conditions that the fuel utilization is over the optimal point, as the air utilization and the equivalence ratio are both increased, the total external reforming rate is decreased. It is mainly caused by the insufficient engine exhaust heat and available thermal energy of anode off-gas to be supplied to the external reformer 1 and 2.

For steam generation through HEX 1 and HEX 2, the proportion of heat supply in HEX 1 is directly related to the change of the air utilization. As the air utilization decreases, the cathode off-gas can be used more for steam generation in HEX 1 due to increase in thermal energy by increase in mass flow rate. It leads to the decrease in the required engine exhaust heat supplied to the HEX 2. Hence,

the proportion of heat-supply for steam generation in HEX 1 is larger than HEX 2 at optimal point. However, it should be noted that both HEX 1 and 2 are significant component for steam generation as shown in Figure 5.4(c). HEX 1 and 2 should be designed to operate at the similar level of heat supply for steam generation.

For cathode air heating, the HEX 4 is responsible for heat-supply of ~10%, recovering the residual heat of system exhaust caused by pinch limit in the HEX 1. Still, the quantity of heat recovered from the HEX 4 is comparable to that of heat-supply in the external reformer 1, since overall heat which should be supplied for the cathode air heating is considerably high, e.g., 4~5 kW at the optimal condition. Hence, if there is no HEX 4, the unused system exhaust heat is lost, and the system efficiency is expected to decrease.

In conclusion, all the BOPs in the system configuration discussed in Figure 3.5 are significant for the system operation as shown in Figure 5.4, regardless of the design fuel utilization for the hybrid system. It is noted that optimization for thermal energy distribution of anode/cathode off-gas and engine exhaust is important issue in the SOFC-SAI engine hybrid system. Hence, it is re-confirmed that the Case 2 is the most desirable configuration design for the SOFC-SAI engine hybrid system in terms of thermal energy distribution and the improved system efficiency.

5.2.2.3. Optimal operation (design point)

The detailed information on the optimal point presented in Figure 5.3(a), is listed in Table 5.2 and Table 5.3. The approximate optimum listed in Table 5.2 is the DOE point closest to the optimum value obtained by the response surface. The efficiency of ~63.2% is achieved in the hybrid system at the approximate optimum, when it is operated at the fuel utilization of 75%, the air utilization of 25% and the equivalence ratio of 0.55. The detailed performance at the optimal point is provided in Table 5.3, and the stream properties at the design point is described in Appendix E.

Table 5.2 – Optimization result: design point for the hybrid system

	Variable	Optimization result	Approximate optimum
Fuel cell	Fuel utilization [%]	76.73	75
	Air utilization [%]	26.93	25
Engine	Equivalence ratio [-]	0.586	0.55
Hybrid system	Efficiency [%]	62.88	63.2

**Table 5.3 – Performance of the hybrid system at the design point
(optimal operation)**

Operating conditions	System	Fuel (CH ₄) LHV [kW]	8.311
		S/C ratio	2.5
	Fuel cell	Fuel utilization [%]	75
		Air utilization [%]	25
		Operating temperature [°C]	750
	Engine (experiment)	Equivalence ratio [-]	0.55
		Intake temperature [°C]	276
		Intake pressure [bar]	0.97
		Speed [RPM]	1,800
	Performance	Fuel cell	Cell voltage [V]
Power [kW]			4.794
Efficiency [%]			70
Engine		Power [kW]	0.462
		Efficiency [%]	19.3
		Power generation share [%]	8.8
		Combustion efficiency [%]	93.4
		Operation stability (COV _{NMEP} / COV _{GMEP}) [%]	6.4 / 4.2
		Combustion phasing (CA50) [CAD aTDC]	0.6
BOP		Total external reforming rate [%]	59.7
		Heat-supply proportion of each external reformer	1:1.6:1.5
		Effectiveness	
		External reformer 1	0.569
		External reformer 2	0.785
		External reformer 3	0.347
		HEX 1 (pinch limit = 10°C)	0.683
		HEX 2	0.850
Hybrid system		Power [kW]	5.26
		Efficiency [%]	63.2

5.3. Conclusions

In this study, a novel system configuration for SOFC-SAI engine hybrid system based on natural gas is designed for efficient heat distribution to BOP operation. Furthermore, the operating conditions are optimized through response surface for the most efficient power generation in the system. In this regard, system-level analysis integrating actual engine experimental results and simulation modeling for BOPs and fuel cell was performed to provide the understanding of the hybrid system operating characteristics as well as the DOE data points for optimization study. The detailed findings are summarized below.

- 1) A novel system configuration for SOFC-SAI engine hybrid system based on natural gas is developed through comparative analysis on three feasible cases out of nine total combinational cases, considering the operating characteristics of counter-flow heat exchanger and the heat transfer quality between heat source (anode/cathode off-gas) and heat sink (BOPs which require heat-supply).
- 2) The key issue for the system design is summarized as efficient thermal energy distribution of anode/cathode off-gas for the external reforming related to the fuel cell operation. As a result, the best configuration which includes three external reformers using thermal energy of anode/cathode off-gas is suggested (Case 2). Furthermore, to efficiently recover the remaining heat in the system exhaust due to the pinch limit at a heat exchanger for steam generation (HEX 1), a heat exchanger (HEX 4) is introduced in the hybrid system, which could recover 3–4% of fuel LHV in the system.
- 3) Performance of SAI engine using anode off-gas as fuel is investigated

through experiments under variation of operating parameters, i.e., fuel utilization in fuel cell and equivalence ratio of engine. It is demonstrated that the combustion mode varies from pure SI to SACI, mostly depending on the engine intake temperature, all of which satisfactorily achieves over 90% combustion efficiency in the feasible region.

- 4) In optimization process, major operating conditions, i.e., fuel utilization, air utilization and equivalence ratio, affecting the electrochemical reaction in the fuel cell and combustion reaction in the engine are used as variables. Non-linear inequality constraints for stable operation of the hybrid system, i.e., stable combustion and thermal self-sustainability, are considered for the optimization.
- 5) DOE and RSM are used for the optimization. The observation data by the DOE adopt the system performance result by the system-level modeling, combining the engine experimental results and the fuel cell and BOP simulation model results. Response surface, which represents the hybrid system behavior, is a multiple linear regression model obtained by LSM. It is confirmed through parametric study that the hybrid system could have complicated non-linear behavior. Hence, the response surface is developed based on full cubic form with interaction term, and n-level full factorial design is adopted for the DOE to improve the model accuracy. The response surface has reliable accuracy, i.e., the error is within $\sim 0.16\%$ of system efficiency.
- 6) At the optimal operation, i.e., fuel utilization of $\sim 75\%$, air utilization of $\sim 25\%$ and equivalence ratio of ~ 0.55 , the efficiency of $\sim 63.2\%$ can be achieved in the novel SOFC-SAI engine hybrid system. The power generation is ~ 5.26

kW, and the power share of the engine is ~9%. Overall external reforming rate (methane conversion ratio) is ~60%.

5.4. Discussions

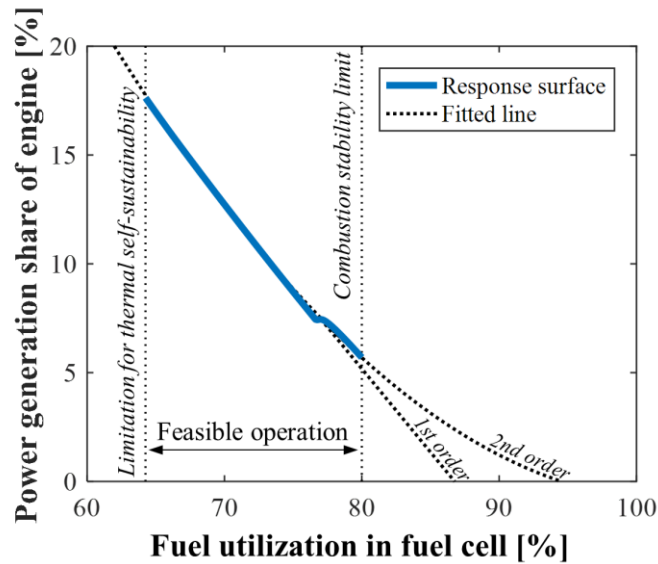


Figure 5.5 – Power generation share of engine in the hybrid system

The hybrid system operation is limited by the combustion stability of engine and thermal self-sustainability of fuel cell. The engine power generated in the hybrid system is responsible for 6–18% of the system power in the feasible operation range, i.e., fuel utilization of 64–80%. Even if the combustion occurs stable at the condition that the fuel utilization is over 80%, the hybrid operation is not meaningful at the condition that the fuel utilization is over ~90%, as shown in Figure 5.5. In fact, it is difficult to operate the fuel cell at the high fuel utilization due to several issues such as losses and durability related to thermal stress [7, 15, 27]. Hence, in terms of the hybrid operation, it is important to

improve the combustion stability and the engine efficiency for increase in the hybrid system power. Furthermore, it is expected that the hybrid system operates efficiently at the lower fuel utilization.

There are several ways to increase the engine efficiency in the hybrid system operation. Firstly, the improved efficiency can be achieved through increase in compression ratio. Since the anode off-gas has a lot of inert gas, knock which is a general issue in SI engine, may be not occurred. In addition, the intake temperature can be lowered further, since the higher post-compression temperature and pressure at the higher compression ratio are favorable for the combustion. It leads to increase in the available thermal energy of anode off-gas supplied for the external reforming. Secondly, the combustion behavior is improved through reducing S/C ratio under coking limit [29-31], since the inert gases in the anode off-gas such as H₂O are decreased. It is also favorable for the system operation due to reducing heat-supply for the steam generation.

Consequently, it is necessary to investigate the effect of engine compression ratio and S/C ratio on the hybrid system operation. It is expected that the engine and the fuel cell are able to operate efficiently under the lower fuel utilization by the improved engine efficiency.

Chapter 6. Summary and Conclusions

In this study, a novel SOFC-ICE hybrid system is proposed to increase system efficiency by using residual fuel of anode off-gas from a SOFC in an ICE. For the stability and controllability of combustion, SAI is adopted for the ICE operation in the hybrid system. Furthermore, it is expected to reduce the thermal energy use of anode off-gas required for the stable combustion. Since it is the first attempt to use such a new combustion concept in the hybrid system, feasibility of SAI and its effect on the system operation are investigated in this study. The feasibility of SAI operation is confirmed through actual engine experiments.

Furthermore, the most desirable system configuration using SAI operation for the improved system efficiency is investigated through case study. Considering the operating characteristics of heat exchanger and heat transfer quality between heat source (anode/cathode off-gas) and heat sink (BOPs which require heat-supply for operation), comparative analysis is performed for the three feasible cases out of nine total combinational cases. The key issue for the system design is summarized as efficient thermal energy distribution of anode/cathode off-gas for the external reforming related to the fuel cell operation. As a result, the novel configuration (Case 2) which includes three external reformers using thermal energy of both anode/cathode off-gas and a heat exchanger recovering the residual heat from the system exhaust for cathode air pre-heating is developed in this study.

Finally, the operation of SOFC-SAI engine hybrid system is optimized by using design of experiment (DOE) and response surface method (RSM). In this study, optimization of fuel utilization, air utilization and equivalence ratio is

performed, since these parameters are directly related to the electrochemical reaction in the fuel cell and combustion reaction in the engine, which produce power in the hybrid system. However, the hybrid system has some constraints such as combustion stability of the engine and thermal self-sustainable operation of the fuel cell, since operating stability as well as efficiency is an important factor for the power generation. Hence, the optimal solution is obtained considering the non-linear inequality constraints. As a result, it is expected that the system efficiency of ~63.2% can be achieved in the SOFC-SAI engine hybrid system at the optimal operating condition such as fuel utilization of 75%, the air utilization of 25% and the equivalence ratio of 0.55. The detailed findings are summarized below.

6.1. Modeling for system-level analysis

- 1) Physics-based model for fuel cell and BOPs are developed based on zero-dimension, steady-state and equilibrium-state, using MATLAB. Thermodynamic properties are calculated by using Cantera toolbox [33] and GRI 3.0 mechanism [34].
- 2) The fuel cell model is validated with stack experimental data [32] under variation of load, air supply, system fuel composition and external reforming rate. The validation results represent reliable prediction of anode off-gas composition and power.
- 3) System-level analysis is performed by integrating of actual engine experimental results and simulation modeling for fuel cell and BOPs. In this study, system fuel, S/C ratio and operating temperature/pressure of

fuel cell are fixed. Anode off-gas state is determined by the fuel utilization. Hence, the engine experiments can be performed prior to the entire hybrid system calculation.

6.2. Feasibility of SAI operation in engine

- 1) In the case discussed in Chapter 2, the spark-assisted ignition makes the combustion of the anode off-gas stable (COV: 5–7%) and controllable for combustion phasing, even while the intake temperature of the engine decreases by $\sim 150^{\circ}\text{C}$ compared to the HCCI operation that the combustion phasing is highly sensitive to the intake temperature. The SAI engine power is maintained at the almost same level with stable HCCI operation, i.e., ~ 0.86 kW, due to decrease in heat loss by the lowered intake temperature.
- 2) CO and H₂ emissions by the combustion inefficiency and insufficient exhaust temperature in the SAI engine can be resolved by the catalytic oxidizer, which has high conversion efficiency at lean-burn condition. There is almost no NO_x emission, i.e., ~ 3 ppm corrected to 15% O₂, as the post-combustion temperature is low due to low-load condition and highly-diluted fuel-lean mixture.
- 3) The SAI engine operates in the HCCI–SACI–SI transition region, which is investigated by using the Livengood–Wu correlation and NHRR analysis.
- 4) In the case discussed in Chapter 2, the engine exergy efficiency of $\sim 37\%$ is achieved, and it is capable of better using the thermal energy of anode

off-gas. It is confirmed by energy and exergy analysis that the thermal self-sustainability of the hybrid system is improved. The indicated efficiency increases by $\sim 8.5\%$ over the hybrid system with HCCI operation; through the SAI engine with the external reformer 2, the catalytic oxidizer and the intake temperature decrease.

- 5) It is expected that the SAI engine is able to cover transient operation such as start-up, e.g., power generation and exhaust heat-supply during pre-heating process through combustion of natural gas or partially reformed gas.
- 6) Spark-assisted ignition, which is a new concept for the anode off-gas combustion, is capable of controlling the combustion stably coping with ever-varying anode off-gas from the fuel cell under widely operating variation in the hybrid system. Furthermore, it could contribute to improvement in operability of the hybrid system while reducing the exergy destruction in the engine. Hence, this combustion strategy is expected to be applicable for the practical development of SOFC-ICE hybrid system.

6.3. System design

- 1) In the hybrid system based on natural gas (or other hydrocarbon fuel), thermal energy is required for external reforming, steam generation, cathode air heating and stable combustion. The thermal energy required for achieving stable combustion is reduced by SAI operation.
- 2) It is important to distribute the thermal energy of anode/cathode off-gas for external reforming, steam generation and cathode air heating. Thus, case study for the efficient thermal energy distribution is performed. Considering all the possible cases for system configuration design, comparative analysis on three feasible cases out of nine total combinational cases is conducted for the detailed investigation. The key issue for the system design is summarized as efficient thermal energy distribution of anode/cathode off-gas for the external reforming related to the fuel cell operation.
- 3) The detailed configuration with counter-flow heat exchanger is designed considering heat transfer quality. The best configuration which includes three external reformers using thermal energy of anode/cathode off-gas is suggested (Case 2).
- 4) In order to recover the heat loss of system exhaust due to pinch limit at a heat exchanger for steam generation (HEX 1), a heat exchanger (HEX 4) is introduced in the hybrid system.
- 5) For the efficient heat distribution, the extent of each BOP significance such as external reformer, heat exchanger for steam and cathode air is analyzed through parametric study.

6.4. Optimal operation

- 1) Performance of SAI engine using anode off-gas as fuel is investigated through experiments under variation of operating parameters, i.e., fuel utilization in fuel cell and equivalence ratio of engine. It is demonstrated that the combustion mode varies from pure SI to SACI, mostly depending on the engine intake temperature, all of which satisfactorily achieves over 90% combustion efficiency in the feasible region.
- 2) Operating conditions, i.e., fuel utilization, air utilization and equivalence ratio, affecting the electrochemical reaction in the fuel cell and combustion reaction in the engine are optimized. Non-linear inequality constraints for stable operation of the hybrid system, i.e., stable combustion and thermal self-sustainability, are considered for the optimization.
- 3) DOE and RSM are used for the optimization. The observation data by the DOE adopt the system performance result by the system-level modeling, combining the engine experimental results and the simulation model results (fuel cell and BOPs). Response surface, which represents the hybrid system behavior, is a multiple linear regression model obtained by LSM.
- 4) It is confirmed through parametric study that the hybrid system could have complicated non-linear behavior. Hence, the response surface is developed based on full cubic form with interaction term, and n-level full factorial design is adopted for the DOE to improve the model accuracy. The response surface has reliable accuracy, i.e., the mean error is within

~0.16%p of system efficiency.

- 5) At the optimal operation, i.e., fuel utilization of ~75%, air utilization of ~25% and equivalence ratio of 0.55, the efficiency of ~63.2% can be achieved in the novel SOFC-SAI engine hybrid system. The power generation is ~5.26 kW, and the power share of the engine is ~9%. Overall external reforming rate (methane conversion ratio) is ~60%.
- 6) In order to increase the engine efficiency, it is noted that it is necessary to investigate the effect of engine compression ratio and S/C ratio on the SOFC-SAI engine hybrid system in future work. It is expected that the engine and the fuel cell are able to operate efficiently at the lower fuel utilization in fuel cell. It may result in the improved hybrid system efficiency.

Appendix A. Fuel cell modeling based on steady-state and zero-dimensional equation

A.1. Specifications of the fuel cell model

Specifications of the fuel cell, which is anode-supported, are described in Table A.1.

Table A.1 – Specifications of the fuel cell model

Parameter		Value
Activation energy [J/mol]	$E_{act,an}$	$120 \cdot 10^3$
	$E_{act,ca}$	$120 \cdot 10^3$
Coefficients for exchange current density [A/m ²]	γ_{an}	$1 \cdot 10^{11}$
	γ_{ca}	$2 \cdot 10^{10}$
Thickness [μm]	δ_{an}	500
	δ_{ca}	40
	δ_{el}	10
	δ_{int}	180
Pore radius [μm]	r_{an}, r_{ca}	0.5
Porosity [%]	$\varepsilon_{an}, \varepsilon_{ca}$	70
Tortuosity [-]	τ_{an}, τ_{ca}	6

A.2. Thermodynamic states in anode and cathode

The outlet gas states are calculated by Cantera toolbox and GRI 3.0 mechanism under the given operating conditions, i.e., fuel utilization, air utilization, operating temperature and pressure, system fuel rate and S/C ratio, including electrochemical reaction, internal reforming (SMR) and water-gas shift reaction (WGSR). The inlet gas information (composition and flow rate) is determined by the system model as described in Section 2.1. The operating

temperature is defined as described in Eq. (A.1). The mean mole fraction in the fuel cell, e.g., anode, is defined as Eq. (A.2). The partial pressure of each species in the following equations is calculated using the mean mole fraction.

$$T_{Fuelcell} = \frac{T_{an,out} + T_{ca,out}}{2} \quad (A.1)$$

$$x_{an} = \frac{x_{an,in}\dot{N}_{an,in} + x_{an,out}\dot{N}_{an,out}}{\dot{N}_{an,in} + \dot{N}_{an,out}} \quad (A.2)$$

A.3. Current, voltage and heat transfer of the fuel cell

The **current density** is described as Eq. (A.3).

$$j_{Fuelcell} = \frac{\dot{N}_{ca \rightarrow an, O_2} (2n_e) F}{n_{cell} A_{cell}} \quad (A.3)$$

The voltage is calculated considering Nernst voltage, activation loss, ohmic loss and concentration loss, based on hydrogen [36-38]. The **Nernst voltage** is described in Eq. (A.4) [6].

$$V_{Nernst} = V_T - \frac{R_u T_{Fuelcell}}{n_e F} \ln \left(\frac{p_{an, H_2 O} / P_{atm}}{(p_{an, H_2} / P_{atm})(p_{ca, O_2} / P_{atm})^{0.5}} \right) \quad (A.4)$$

The **activation loss** is described in Eqs. (A.5)–(A.8) [6, 52].

$$j_{0,an} = \gamma_{an} (p_{an, H_2} / P_{atm}) (p_{an, H_2 O} / P_{atm}) \exp \left(\frac{-E_{act, an}}{R_u T_{Fuelcell}} \right) \quad (A.5)$$

$$j_{0,ca} = \gamma_{ca} (p_{ca,O_2}/P_{atm})^{0.25} \exp\left(\frac{-E_{act,ca}}{R_u T_{Fuelcell}}\right) \quad (A.6)$$

$$V_{act,an} = \frac{2R_u T_{Fuelcell}}{n_e F} \sinh^{-1}\left(\frac{j_{Fuelcell}}{2j_{0,an}}\right) \quad (A.7)$$

$$V_{act,ca} = \frac{2R_u T_{Fuelcell}}{n_e F} \sinh^{-1}\left(\frac{j_{Fuelcell}}{2j_{0,ca}}\right) \quad (A.8)$$

The **ohmic loss** is described in Eqs. (A.9)–(A.13) [53].

$$\rho_{an} = 2.980 \cdot 10^{-5} \exp(-1392/T_{Fuelcell}) \quad (A.9)$$

$$\rho_{ca} = 8.114 \cdot 10^{-5} \exp(600/T_{Fuelcell}) \quad (A.10)$$

$$\rho_{el} = 2.940 \cdot 10^{-5} \exp(10350/T_{Fuelcell}) \quad (A.11)$$

$$\rho_{int} = 1.256 \cdot 10^{-3} \exp(4690/T_{Fuelcell}) \quad (A.12)$$

$$V_{ohm} = j_{Fuelcell} (\rho_{an} \delta_{an} + \rho_{ca} \delta_{ca} + \rho_{el} \delta_{el} + \rho_{int} \delta_{int}) \quad (A.13)$$

The **concentration loss** is calculated considering Knudsen diffusion coefficient (Eqs. (A.14)–(A.16)) and nominal diffusivity (Eqs. (A.17)–(A.18)) [6, 54].

$$D_{H_2,K} = 97 r_{an} \sqrt{T_{Fuelcell}/MW_{H_2}} \quad (A.14)$$

$$D_{H_2O,K} = 97 r_{an} \sqrt{T_{Fuelcell}/MW_{H_2O}} \quad (A.15)$$

$$D_{O_2,K} = 97 r_{ca} \sqrt{T_{Fuelcell}/MW_{O_2}} \quad (A.16)$$

$$D_{H_2,H_2O} = \frac{3.640 \cdot 10^{-8}}{P_{an}/P_{atm}} \left(\frac{T_{Fuelcell}}{\sqrt{T_{c,H_2} T_{c,H_2O}}} \right)^{2.334} \left(\frac{(P_{c,H_2} P_{c,H_2O})^{\frac{1}{3}}}{(T_{c,H_2} T_{c,H_2O})^{-\frac{5}{12}}} \right) \left(\frac{1}{MW_{H_2}} + \frac{1}{MW_{H_2O}} \right)^{\frac{1}{2}} \quad (A.17)$$

$$D_{O_2,N_2} = \frac{2.745 \cdot 10^{-8}}{P_{ca}/P_{atm}} \left(\frac{T_{Fuelcell}}{\sqrt{T_{c,N_2} T_{c,O_2}}} \right)^{1.823} \left(\frac{(P_{c,N_2} P_{c,O_2})^{\frac{1}{3}}}{(T_{c,N_2} T_{c,O_2})^{-\frac{5}{12}}} \right) \left(\frac{1}{MW_{N_2}} + \frac{1}{MW_{O_2}} \right)^{\frac{1}{2}} \quad (A.18)$$

Effective diffusivity is calculated considering porosity and tortuosity as described in Eq. (A.19).

$$D_{ij}^{eff} = D_{ij} \frac{\varepsilon}{\tau} \quad (A.19)$$

Therefore, the overall effective diffusivity is described in Eqs. (A.20)–(A.22).

$$D_{H_2}^{eff} = \left(\frac{1}{D_{H_2,K}^{eff}} + \frac{1}{D_{H_2,H_2O}^{eff}} \right)^{-1} \quad (A.20)$$

$$D_{H_2O}^{eff} = \left(\frac{1}{D_{H_2O,K}^{eff}} + \frac{1}{D_{H_2,H_2O}^{eff}} \right)^{-1} \quad (A.21)$$

$$D_{O_2}^{eff} = \left(\frac{1}{D_{O_2,K}^{eff}} + \frac{1}{D_{O_2,N_2}^{eff}} \right)^{-1} \quad (A.22)$$

The effective diffusivities for the anode and cathode are calculated as Eqs. (A.23)–(A.24), and α_{O_2} is calculated as Eq. (A.25).

$$D_{an}^{eff} = \left(\frac{p_{an,H_2O}}{P_{an}} \right) D_{H_2}^{eff} + \left(\frac{p_{an,H_2}}{P_{an}} \right) D_{H_2O}^{eff} \quad (A.23)$$

$$D_{ca}^{eff} = D_{O_2}^{eff} \quad (A.24)$$

$$\alpha_{O_2} = \frac{D_{O_2,K}^{eff}}{D_{O_2,K}^{eff} + D_{O_2,N_2}^{eff}} \quad (A.25)$$

Finally, the concentration loss equation is obtained as Eqs. (A.26)–(A.27).

$$V_{con,an} = \frac{-R_u T_{Fuelcell}}{n_e F} \ln \left[\frac{1 - j_{Fuelcell} \left(\frac{R_u T_{Fuelcell}}{n_e F} \right) \frac{\delta_{an}}{D_{an}^{eff} p_{an,H_2}}}{1 + j_{Fuelcell} \left(\frac{R_u T_{Fuelcell}}{n_e F} \right) \frac{\delta_{an}}{D_{an}^{eff} p_{an,H_2O}}} \right] \quad (A.26)$$

$$V_{con,ca} = \frac{-R_u T_{Fuelcell}}{2n_e F} \ln \left[\frac{\frac{P_{ca}}{\alpha_{O_2}} - \left(\frac{P_{ca}}{\alpha_{O_2}} - p_{ca,O_2} \right) \exp \left(\frac{R_u T_{Fuelcell}}{2n_e F} \left(\frac{\alpha_{O_2} \delta_{ca}}{D_{ca}^{eff} P_{ca}} \right) j_{Fuelcell} \right)}{p_{ca,O_2}} \right] \quad (A.27)$$

Consequently, the **cell voltage** considering the losses described above is calculated as Eq. (A.28).

$$V_{Fuelcell} = V_{Nernst} - V_{act,an} - V_{act,ca} - V_{ohm} - V_{con,an} - V_{con,ca} \quad (A.28)$$

In the end, the **heat transfer of the fuel cell** is calculated using the first law of thermodynamics as shown in Figure A.1 and Eq. (A.29).

$$\begin{aligned} & h_{an,in} \dot{m}_{an,in} + h_{ca,in} \dot{m}_{ca,in} \\ & = h_{an,out} \dot{m}_{an,out} + h_{ca,out} \dot{m}_{ca,out} + W_{Fuelcell} + Q_{Fuelcell} \end{aligned} \quad (A.29)$$

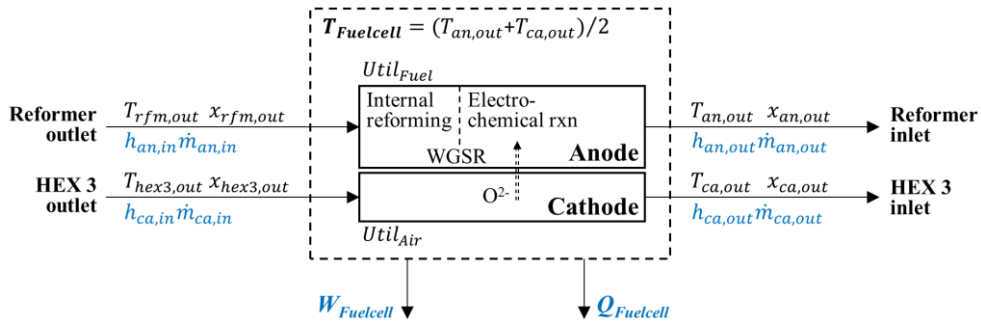


Figure A.1 – Configuration of the fuel cell model

For the system-level analysis in Section 2.4, the design operating temperature of the fuel cell model is fixed at 750°C which is average temperature of anode/cathode outlet temperature from the stack experimental data. It means that the anode/cathode outlet temperatures are also fixed at 750°C in the fuel cell model. Although the temperature of partially reformed gas after external reformers does not rise up to 750°C, the heat emitted by exothermic electrochemical reaction in the stack is capable of increasing the temperature of the partially reformed gas, i.e., stack inlet gas, inside the stack or hot box to insulate the stack. Furthermore, the heat, i.e., exothermicity, is also distributed for the endothermic internal reforming in the stack while maintaining the design operating temperature. If the additional heat supply is required to maintain the design operating temperature, it is calculated in the fuel cell model using energy balance equation, as shown in Figure A.1, Figure A.2 and Eq. (A.29). The heat transfer for maintaining the design operating temperature provided in Figure 2.18(c) was used as an indicator of the feasibility of the hybrid system, i.e., the thermally self-sustainable operability, as described in Section 2.4.1. If the fuel cell needs additional heat supply for the design operating temperature, it is

considered as infeasible operation in terms of thermal self-sustainability or considered as decrease in the system efficiency due to additional heat supply.

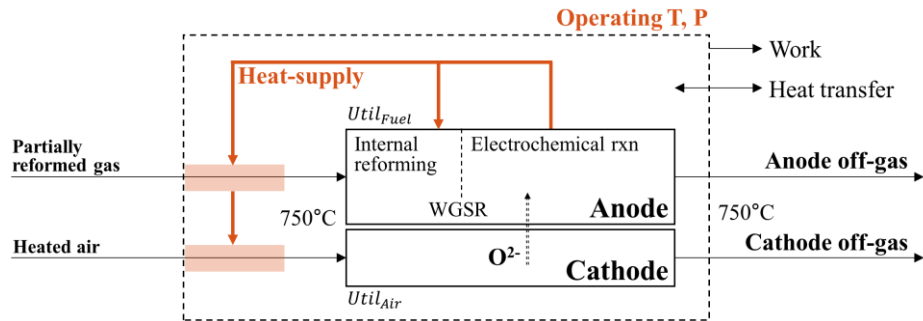


Figure A.2 – Calculation of heat distribution in the fuel cell

Appendix B. Ignition delay calculation

In general, the first law of thermodynamics at the given control volume (CV), i.e., energy equation, is described as Eqs. (B.1)–(B.2).

$$\dot{U} = \dot{H} - \dot{Q} - \dot{W} \quad (B.1)$$

$$\begin{aligned} m_{cv}c_{v,cv}\dot{T}_{cv} + \sum_i u_{cv,i}\dot{m}_{cv,i} \\ = h_{transfer}\dot{m}_{transfer} - \dot{Q}_{transfer} - P_{cv}\dot{V}_{cv} \end{aligned} \quad (B.2)$$

Thus, the instantaneous temperature of the control volume can be solved by Eq. (B.3).

$$\dot{T}_{cv} = \frac{1}{m_{cv}c_{v,cv}} \left(-\dot{Q}_{transfer} - P_{cv}\dot{V}_{cv} + h_{transfer}\dot{m}_{transfer} - \sum_i u_{cv,i}\dot{m}_{cv,i} \right) \quad (B.3)$$

In this study, a reactor model under adiabatic process which is closed system and has a constant-volume was adopted for the ignition delay calculation [22]. Thus transfer-related terms are not necessary as described in Eq. (B.4). The numerator of Eq. (B.4) represents the net production rate of each species in the reactor model, which is determined by calculation of chemical kinetics through Cantera toolbox [33].

$$\dot{T}_{cv} = \frac{-\sum_i u_{cv,i}\dot{m}_{cv,i}}{m_{cv}c_{v,cv}} \quad (B.4)$$

Mass balance equation for each species only includes the chemical kinetics, i.e., net production rate, because there is no mass transfer. Thus, the instantaneous pressure of the reactor model can be solved by the ideal gas law described in Eq. (B.5).

$$P = \frac{nR_u T}{V} \quad (B.5)$$

The unburned gas conditions in cylinder at a given crank angle such of temperature, pressure and composition as shown in Figure B.1 are set as the initial state for the reactor model. The state over time in the reactor model is obtained by solving the ordinary differential equations related to energy and mass balance. Consequently, the ignition delay at the given initial state is calculated, based on the maximum pressure rise rate due to the chemical reaction in the reactor model. Ignition delay calculation of synthesis gas (mixture of H₂ and CO) through the modeling and GRI 3.0 mechanism is validated with experimental results of previous studies as shown in Figure B.2.

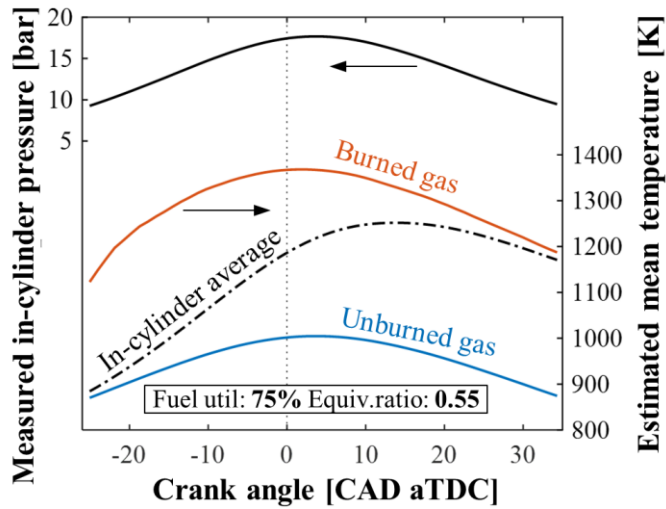


Figure B.1 – In-cylinder pressure and temperature profile over crank angle; in the case of the experimental results in Section 4.3

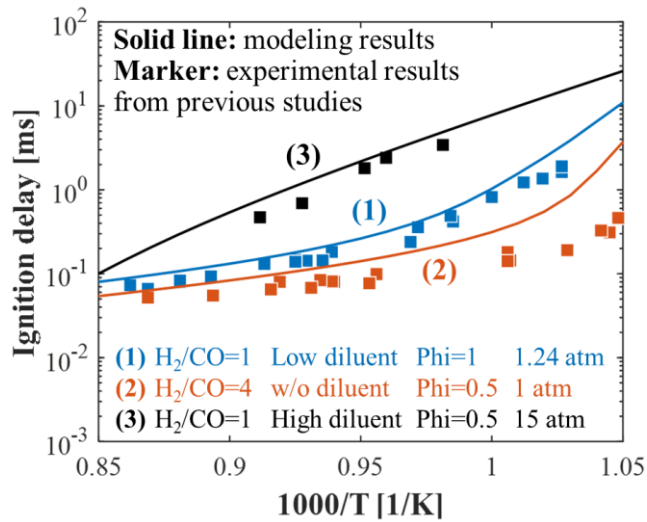


Figure B.2 – Validation result of the modeling for synthesis gas ignition delay calculation; with experimental results from previous studies ((1):[57] (2):[58] (3):[59])

Appendix C. Stream properties of SOFC-SAI engine hybrid system (in Chapter 2)

The detailed stream properties of the SOFC–SAI engine hybrid system are described in Table C.1, at the operating condition achieving the efficiency of ~61.6% that the intake temperature is ~287°C.

Table C.1 – Stream properties of the SOFC–SAI engine hybrid system at the operating condition achieving the efficiency of ~61.6% (in Chapter 2)

State	Temp. [°C]	Mass flow [kg/hr]	Mole fraction on a wet basis [%]							
			CH ₄	H ₂	CO	CO ₂	H ₂ O	O ₂	N ₂	
Anode fuel	1	25	0.72	100.0	-	-	-	-	-	-
	2	150	2.74	28.57	-	-	-	71.43	-	-
	3	500	2.74	14.13	35.43	1.32	7.86	41.25	-	-
	4	558	2.74	9.28	45.58	3.53	8.75	32.86	-	-
Engine intake	5	750	4.75	-	18.50	3.32	14.86	63.32	-	-
	6	539	4.75	-	18.50	3.32	14.86	63.32	-	-
	7	25	6.72	-	-	-	-	-	21.00	79.00
	8	287	11.47	-	9.50	1.71	7.63	32.53	10.21	38.42
Engine exhaust	9	457	11.47	-	1.60	0.35	9.47	42.51	5.81	40.26
	10	593	11.47	-	-	-	9.92	44.55	4.88	40.66
	11	245	11.47	-	-	-	9.92	44.55	4.88	40.66
Cathode air	12	25	24.65	-	-	-	-	-	21.00	79.00
	13	558	24.65	-	-	-	-	-	21.00	79.00
	14	750	22.64	-	-	-	-	-	14.73	85.27
System exhaust	15	193	22.64	-	-	-	-	-	14.73	85.27
	16	186	11.47	-	-	-	9.92	44.55	4.88	40.66
	17	190	34.11	-	-	-	3.61	16.21	11.15	69.03
	18	66	34.11	-	-	-	3.61	16.21	11.15	69.03
Steam	19	25	2.02	-	-	-	-	100.0	-	-
	20	100	2.02	-	-	-	-	100.0	-	-
	21	206	2.02	-	-	-	-	100.0	-	-

Appendix D. Equation of the response surface

Table D.1 – Response surface model by multiple linear regression through least squares method

Term	Coded variable	The least squares estimator of β	#	Combination
Intercept	1	60.8460	1	–
Linear	x_1	-1.3959	2	(1)
	x_2	3.0006	3	(2)
	x_3	0.0241	4	(3)
Quadratic	x_1^2	-0.5667	5	(1,1)
	x_1x_2	0.1422	6	(1,2)
	x_1x_3	-0.2040	7	(1,3)
	x_2^2	-1.4775	8	(2,2)
	x_2x_3	-0.9205	9	(2,3)
	x_3^2	-0.3698	10	(3,3)
	Cubic	x_1^3	0.5342	11
	$x_1^2x_2$	0.1733	12	(1,1,2)
	$x_1^2x_3$	0.1283	13	(1,1,3)
	$x_1x_2^2$	0.7552	14	(1,2,2)
	$x_1x_2x_3$	0.5730	15	(1,2,3)
	$x_1x_3^2$	0.2735	16	(1,3,3)
	x_2^3	0.0514	17	(2,2,2)
	$x_2^2x_3$	-0.2552	18	(2,2,3)
	$x_2x_3^2$	0.1264	19	(2,3,3)
	x_3^3	0.1968	20	(3,3,3)

The least squares estimator of β means a slope for the corresponding coded variables. From the value, the sensitivity of the operating parameters can be predicted. For example, the fuel utilization (third term) has the largest value in the linear terms. It means that the fuel utilization, i.e., load distribution, has a significant effect on the system efficiency, as provided in Section 4.4. In addition, although air utilization (4th term) has the lowest absolute value, it is expected that the interaction between air utilization and the fuel utilization is significant in terms of the system efficiency, since the interaction term (9th term) is quite high.

Appendix E. Stream properties of SOFC-SAI engine hybrid system at the optimal operation (in Chapter 5)

Table E.1 – Stream properties of the SOFC–SAI engine hybrid system at the optimal operation (in Chapter 5)

State	Temp. [°C]	Mass flow [kg/hr]	Mole fraction on a wet basis [%]							
			CH ₄	H ₂	CO	CO ₂	H ₂ O	O ₂	N ₂	
Anode fuel	1	25	0.598	100.0	-	-	-	-	-	-
	2	150	2.277	28.57	-	-	-	71.43	-	-
	3	343	2.277	24.36	10.69	0.02	2.66	62.27	-	-
	3a	483	2.277	15.49	32.36	0.94	7.39	43.82	-	-
	4	566	2.277	8.56	46.97	3.97	8.76	31.74	-	-
Engine intake	5	750	4.07	-	15.44	2.75	15.43	66.38	-	-
	6	433	4.07	-	15.44	2.75	15.43	66.38	-	-
	7	25	4.66	-	-	-	-	-	21.00	79.00
	8	276	8.73	-	8.64	1.54	8.63	37.14	9.25	34.80
Engine exhaust	9	372	8.73	-	0.41	0.27	10.42	47.65	4.72	36.53
	10	421	8.73	-	-	-	10.73	48.22	4.39	36.66
	11	288	8.73	-	-	-	10.73	48.22	4.39	36.66
Cathode air	12	25	30.73	-	-	-	-	-	21.00	79.00
	12a	86	30.73	-	-	-	-	-	21.00	79.00
	13	566	30.73	-	-	-	-	-	21.00	79.00
	14	750	28.94	-	-	-	-	-	16.62	83.38
	14a	676	28.94	-	-	-	-	-	16.62	83.38
System exhaust	15	179	28.94	-	-	-	-	-	16.62	83.38
	16	156	8.73	-	-	-	10.73	48.22	4.39	36.66
	17	173	37.67	-	-	-	2.75	12.36	13.49	71.40
	18	97	37.67	-	-	-	2.75	12.36	13.49	71.40
	18a	50	37.67	-	-	-	2.75	12.36	13.49	71.40
Steam	19	25	1.68	-	-	-	-	100.0	-	-
	20	100	1.68	-	-	-	-	100.0	-	-
	21	206	1.68	-	-	-	-	100.0	-	-

References

- [1] Kim S, Jung JY, Song HH, Song SJ, Ahn KY, Lee SM, Lee YD, Kang S. Optimization of molten carbonate fuel cell (MCFC) and homogeneous charge compression ignition (HCCI) engine hybrid system for distributed power generation. *international journal of hydrogen energy*. 2014;39:1826-40.
- [2] Yun J, Cho K, Lee YD, Yu S. Four different configurations of a 5 kW class shell-and-tube methane steam reformer with a low-temperature heat source. *International Journal of Hydrogen Energy*. 2018;43:4546-62.
- [3] Gong Y, Huang K. Study of a renewable biomass fueled SOFC: the effect of catalysts. *International Journal of Hydrogen Energy*. 2013;38:16518-23.
- [4] Ravi N, Liao H-H, Jungkunz AF, Song HH, Gerdes JC. Modeling and control of exhaust recompression hcci: Split fuel injection for cylinder-individual combustion control. *IEEE Control Systems*. 2012;32:26-42.
- [5] (U.S.) EIA. *Annual Energy Outlook 2019: With projections to 2050*. 2019.
- [6] O'hayre R, Cha S-W, Prinz FB, Colella W. *Fuel cell fundamentals*: John Wiley & Sons; 2016.
- [7] Leone P, Matencio T, Garciã M, Domigues Z, Lanzini A, Santarelli M. Limiting factors for a planar solid oxide fuel cell under different flow and temperature conditions. *Fuel Cells*. 2013;13:733-42.
- [8] Park SH, Lee YD, Ahn KY. Performance analysis of an SOFC/HCCI engine hybrid system: system simulation and thermo-economic comparison. *International Journal of Hydrogen Energy*. 2014;39:1799-810.
- [9] Buonomano A, Calise F, d'Accadia MD, Palombo A, Vicidomini M. Hybrid solid oxide fuel cells–gas turbine systems for combined heat and power: a review.

Applied Energy. 2015;156:32-85.

[10] Yi JH, Choi JH, Kim TS. Comparative evaluation of viable options for combining a gas turbine and a solid oxide fuel cell for high performance. Applied Thermal Engineering. 2016;100:840-8.

[11] Gandiglio M, Lanzini A, Leone P, Santarelli M, Borchiellini R. Thermo-economic analysis of large solid oxide fuel cell plants: Atmospheric vs. pressurized performance. Energy. 2013;55:142-55.

[12] Lee YD. Thermodynamic, economic and environmental evaluation of solid-oxide fuel-cell hybrid power-generation systems: Technische Universität Berlin; 2015.

[13] Lee YD, Ahn KY, Morosuk T, Tsatsaronis G. Exergetic and exergoeconomic evaluation of an SOFC-Engine hybrid power generation system. Energy. 2018;145:810-22.

[14] Choi W, Kim J, Kim Y, Kim S, Oh S, Song HH. Experimental study of homogeneous charge compression ignition engine operation fuelled by emulated solid oxide fuel cell anode off-gas. Applied energy. 2018;229:42-62.

[15] Kang S, Ahn K-Y. Dynamic modeling of solid oxide fuel cell and engine hybrid system for distributed power generation. Applied Energy. 2017;195:1086-99.

[16] Lee YD, Ahn KY, Morosuk T, Tsatsaronis G. Exergetic and exergoeconomic evaluation of a solid-oxide fuel-cell-based combined heat and power generation system. Energy conversion and management. 2014;85:154-64.

[17] Wu Z, Tan P, Zhu P, Cai W, Chen B, Yang F, Zhang Z, Porpatham E, Ni M. Performance analysis of a novel SOFC-HCCI engine hybrid system coupled with metal hydride reactor for H₂ addition by waste heat recovery. Energy Conversion and Management. 2019;191:119-31.

- [18] Chuahy FD, Kokjohn SL. Solid oxide fuel cell and advanced combustion engine combined cycle: A pathway to 70% electrical efficiency. *Applied energy*. 2019;235:391-408.
- [19] Hellström E, Stefanopoulou AG, Jiang L. Cyclic variability and dynamical instabilities in autoignition engines with high residuals. *IEEE Transactions on Control Systems Technology*. 2013;21:1527-36.
- [20] Gorzelic P, Hellström E, Stefanopoulou A, Li J. Model-based feedback control for an automated transfer out of SI operation during SI to HCCI transitions in gasoline engines. *ASME 2012 5th Annual Dynamic Systems and Control Conference joint with the JSME 2012 11th Motion and Vibration Conference: American Society of Mechanical Engineers*; 2012. p. 359-67.
- [21] Matthews J, Santoso H, Cheng WK. Load control for an HCCI engine. *SAE Technical Paper*; 2005.
- [22] Song H, Edwards C. Understanding chemical effects in low-load-limit extension of homogeneous charge compression ignition engines via recompression reaction. *International Journal of Engine Research*. 2009;10:231-50.
- [23] Nam Y, Kim J, Bahk C, Jang I, Song HH, Lee D. Modeling, Estimation, and Control of HCCI Engine With In-Cylinder Pressure Sensing. *Journal of Dynamic Systems, Measurement, and Control*. 2018;140:061015.
- [24] Yi JH, Kim TS. Effects of fuel utilization on performance of SOFC/gas turbine combined power generation systems. *Journal of Mechanical Science and Technology*. 2017;31:3091-100.
- [25] Rokni M. Thermodynamic analysis of SOFC (solid oxide fuel cell)–Stirling hybrid plants using alternative fuels. *Energy*. 2013;61:87-97.
- [26] Park YJ, Min G, Hong J. Comparative study of solid oxide fuel cell-

combined heat and power system designs for optimal thermal integration. *Energy Conversion and Management*. 2019;182:351-68.

[27] Kuhn J, Kesler O. Carbon deposition thresholds on nickel-based solid oxide fuel cell anodes I. Fuel utilization. *Journal of Power Sources*. 2015;277:443-54.

[28] Shin G, Yun J, Yu S. Thermal design of methane steam reformer with low-temperature non-reactive heat source for high efficiency engine-hybrid stationary fuel cell system. *International Journal of Hydrogen Energy*. 2017;42:14697-707.

[29] Seo Y-S, Shirley A, Kolaczkowski S. Evaluation of thermodynamically favourable operating conditions for production of hydrogen in three different reforming technologies. *Journal of Power sources*. 2002;108:213-25.

[30] Kuhn J, Kesler O. Carbon deposition thresholds on nickel-based solid oxide fuel cell anodes II. Steam: carbon ratio and current density. *Journal of Power Sources*. 2015;277:455-63.

[31] Oh S, Song HH. Exergy analysis on non-catalyzed partial oxidation reforming using homogeneous charge compression ignition engine in a solid oxide fuel cell system. *International Journal of Hydrogen Energy*. 2018;43:2943-60.

[32] Lee YD, Kim YS, Kang S, Ahn KY, Choi S, Park J, Song HH. High-efficiency Fuel cell–Engine hybrid power generation system. *The Korean Society of Mechanical Engineers*; 2017. p. 1440-2.

[33] Goodwin DG, Moffat HK, Speth RL. *Cantera: An object-oriented software toolkit for chemical kinetics, thermodynamics, and transport processes*. Caltech, Pasadena, CA. 2009.

[34] Smith GP, Golden DM, Frenklach M, Moriarty NW, Eiteneer B, Goldenberg M, Bowman CT, Hanson RK, Song S, Gardiner Jr W. *GRI-Mech 3.0*, 1999. URL http://www.me.berkeley.edu/gri_mech. 2011.

- [35] Lieuwen T, Yetter R, Yang V. Synthesis gas combustion: fundamentals and applications: CRC Press; 2009.
- [36] Holtappels P, De Haart L, Stimming U, Vinke I, Mogensen M. Reaction of CO/CO₂ gas mixtures on Ni-YSZ cermet electrodes. *Journal of Applied Electrochemistry*. 1999;29:561-8.
- [37] Matsuzaki Y, Yasuda I. Electrochemical Oxidation of H₂ and CO in a H₂-H₂O-CO-CO₂ System at the Interface of a Ni-YSZ Cermet Electrode and YSZ Electrolyte. *Journal of the Electrochemical Society*. 2000;147:1630-5.
- [38] Andersson M, Yuan J, Sundén B. SOFC modeling considering hydrogen and carbon monoxide as electrochemical reactants. *Journal of Power Sources*. 2013;232:42-54.
- [39] Bergman TL, Incropera FP, Lavine AS, DeWitt DP. Introduction to heat transfer: John Wiley & Sons; 2011.
- [40] Cho K, Yun J, Yu S. Performance Characteristics of a 5kW Class Mid-Temperature Methane-Steam Reformer Under Different Operating Conditions. *Transactions of the Korean Society of Mechanical Engineers - B*. 2018;42:259-65.
- [41] Heywood JB. Internal combustion engine fundamentals. 1988.
- [42] Sonntag RE, Borgnakke C, Van Wylen GJ, Van Wyk S. Fundamentals of thermodynamics: Wiley New York; 1998.
- [43] Wagner RM, Edwards KD, Daw CS, Green JB, Bunting BG. On the nature of cyclic dispersion in spark assisted HCCI combustion. *SAE Technical Paper*; 2006.
- [44] Larimore J, Hellström E, Sterniak J, Jiang L, Stefanopoulou AG. Experiments and analysis of high cyclic variability at the operational limits of spark-assisted HCCI combustion. *American Control Conference (ACC)*, 2012:

IEEE; 2012. p. 2072-7.

[45] Glewen WJ, Wagner RM, Edwards KD, Daw CS. Analysis of cyclic variability in spark-assisted HCCI combustion using a double Wiebe function. *Proceedings of the Combustion Institute*. 2009;32:2885-92.

[46] Hires S, Tabaczynski R, Novak J. The prediction of ignition delay and combustion intervals for a homogeneous charge, spark ignition engine. *SAE transactions*. 1978:1053-67.

[47] Persson H, Hultqvist A, Johansson B, Remón A. Investigation of the early flame development in spark assisted HCCI combustion using high speed chemiluminescence imaging. *SAE Technical Paper*; 2007.

[48] Manofsky L, Vavra J, Assanis DN, Babajimopoulos A. Bridging the gap between HCCI and SI: Spark-assisted compression ignition. *SAE Technical Paper*; 2011.

[49] Livengood J, Wu P. Correlation of autoignition phenomena in internal combustion engines and rapid compression machines. *Symposium (international) on combustion: Elsevier*; 1955. p. 347-56.

[50] Hernández JJ, Lapuerta M, Sanz-Argent J. Autoignition prediction capability of the Livengood–Wu correlation applied to fuels of commercial interest. *International Journal of Engine Research*. 2014;15:817-29.

[51] Song H, Song HH. Knock Prediction of Two-Stage Ignition Fuels with Modified Livengood-Wu Integration Model by Cool Flame Elimination Method. *SAE Technical Paper*; 2016.

[52] Costamagna P, Honegger K. Modeling of solid oxide heat exchanger integrated stacks and simulation at high fuel utilization. *Journal of the Electrochemical Society*. 1998;145:3995-4007.

[53] Bessette NF, Wepfer WJ, Winnick J. A mathematical model of a solid oxide

- fuel cell. *Journal of the Electrochemical Society*. 1995;142:3792-800.
- [54] Chan S, Khor K, Xia Z. A complete polarization model of a solid oxide fuel cell and its sensitivity to the change of cell component thickness. *Journal of power sources*. 2001;93:130-40.
- [55] Yamasaki Y, Kaneko S. Prediction of ignition and combustion development in an HCCI engine fueled by syngas. *SAE Technical Paper*; 2014.
- [56] Myers RH, Montgomery DC, Anderson-Cook CM. *Response surface methodology: process and product optimization using designed experiments*: John Wiley & Sons; 2016.
- [57] Vasu SS, Davidson DF, Hanson RK. Shock tube study of syngas ignition in rich CO₂ mixtures and determination of the rate of $H + O_2 + CO_2 \rightarrow HO_2 + CO_2$. *Energy & Fuels*. 2011;25:990-7.
- [58] Kalitan DM, Mertens JD, Crofton MW, Petersen EL. Ignition and oxidation of lean CO/H₂ fuel blends in air. *Journal of propulsion and power*. 2007;23:1291-301.
- [59] Herzler J, Naumann C. Shock tube study of the ignition of lean CO/H₂ fuel blends at intermediate temperatures and high pressure. *Combustion Science and Technology*. 2008;180:2015-28.

국 문 초 록

고체산화물 연료전지(SOFC)-내연기관(ICE) 하이브리드 시스템의 목적은 수소를 포함하는 SOFC 애노드오프가스(애노드배출가스)의 잔여 연료를 내연기관에서 사용함으로써 시스템 효율을 향상시키는 것에 있다. 본 연구는 스파크-어시스트 점화(SAI)를 사용하는 엔진을 적용한 새로운 하이브리드 시스템을 제안하였다. 이는 SOFC-ICE 하이브리드 시스템을 위해 새롭게 시도하는 연소 전략이므로, 상기 연소 전략의 운전 가능성 및 하이브리드 시스템 운전에 미치는 영향에 대한 분석을 수행하였다. 또한, 시스템 효율의 향상을 위해 새로운 시스템 구성 설계 및 연료전지와 엔진의 전기화학 반응 및 연소 반응과 관련이 있는 연료이용률, 산소이용률, 당량비와 같은 운전 변수에 대한 최적화 연구를 수행하였다.

본 연구가 제안하는 SOFC-SAI 엔진 하이브리드 시스템은 연료전지, 엔진, 외부개질기, 열교환기, 촉매산화장치 및 혼합부로 이루어진다. 전체 시스템 운전 성능의 분석을 위해, 엔진을 제외한 모든 구성 요소는 본 연구에서 개발한 단순화된 무차원 물리 기반 모델링을 바탕으로 시뮬레이션 해석을 수행하였다. 특히 연료전지의 경우에는, 스택 내부의 전기화학 반응, 내부 개질 반응 및 수성가스 평형 반응 등을 고려하여 개발되었다. 실제 스택 실험 결과와의 정합을 통해 부하, 연료조성, 공기공급 등 운전 조건 변화의 영향을 반영할 수 있도록 하였으며, 연료전지 모델의 정확성을 확보하였다. 엔진의 연소 가능성 및 운전 특성은 실제 단기통 엔진의 실험을 통해 분석하였다. 이를 기반으로, 연료전지와 시스템 구성 요소(BOP)에 대한 시뮬레이션 모델과 실제 엔진 실험 결과를 연계하여 전체적인 SOFC-SAI 엔진 하이브리드 시스템의 운전 성능에 대한 분석을 진행하였다.

첫째, 엔진의 연소 현상이 시스템에 미치는 현상을 분석하기 위해, 흡기 온도, 당량비, 점화시기와 같은 엔진 운전 변수 변화에 대한 엔진 실험을

진행하였으며, 에너지 및 엑서지 관점에서 하이브리드 시스템의 운전 성능에 대한 분석을 수행하였다. 그 결과, 8.2의 낮은 압축비에서 흡기온도를 $\sim 280^{\circ}\text{C}$ 까지 감소시켜도, SAI에 의해 안정적인 애노드오프가스의 연소가 달성되는 것을 확인하였다 (COV: 5-7%). 필요 흡기온도가 낮아짐으로써, 결과적으로 엔진의 엑서지 효율이 $\sim 37\%$ 까지 향상되었으며, 하이브리드 시스템 내 열에너지가 다른 구성 요소에 더욱 효율적으로 사용될 수 있음을 확인하였다. 이로 인해, 하이브리드 시스템의 자연운전성이 향상될 수 있으며, $\sim 61.6\%$ 의 시스템 효율을 달성 할 수 있음이 시스템 해석을 통해 확인되었다. 이때 엔진은 전체 시스템 출력 중 $\sim 14\%$ 의 전력을 생산하며, 질소 산화물 배출은 거의 발생하지 않음을 확인하였다.

둘째, 시스템 효율 및 자연운전성 향상을 위해 시스템 구성을 새롭게 설계하였다. 본 연구의 하이브리드 시스템은 천연가스를 기반으로 하기 때문에, 연료전지 운전 관점에서 외부 개질율을 향상시키는 것이 중요하다. 이를 위해, 시스템 내 열원인 애노드/캐소드 오프가스의 열에너지와 BOP 운전을 위해 필요한 열에너지 공급량을 고려하여, 최적의 열에너지 분배를 위한 시스템 구성 설계안을 선정하였다.

셋째, 본 연구에서 제안 및 설계한 SOFC-SAI 엔진 하이브리드 시스템의 최적 운전 조건에 대한 분석을 진행하였다. 최적 운전 조건 분석에 앞서 하이브리드 시스템의 운전 특성에 대한 이해를 위해, 운전 변수 별 영향에 대한 분석을 수행하였다. 이러한 분석 결과를 기반으로, 실험 계획법 (DOE) 및 Response surface method (반응표면법, RSM)을 사용하여 연료이용률, 산소이용률, 당량비에 대한 운전 조건 최적화를 진행하였다. 하이브리드 시스템의 반응표면(Response surface)은 최소자승법(Least squares method (LSM))을 사용하여 얻어지는 다중선형회귀모델(Multiple linear regression model)로서, 이를 위해 실험 계획법에 의거하여 수행한 관측 데이터(Observation data)가 사용되었다. 본 연구의

관측데이터는 엔진 실험 데이터와 시뮬레이션 모델(연료전지, BOP)의 연계를 통해 얻은 하이브리드 시스템 성능 해석 결과이다. 결과적으로, 하이브리드 시스템의 최적 운전 조건은 반응표면 및 연료전지의 자열운전성, 엔진의 연소안정성을 고려한 비선형 부등식 제한조건(non-linear inequality constraint)하에서 분석되었다. 그 결과, SOFC-SAI 엔진 하이브리드 시스템은 5kW급의 작은 발전 용량임에도 불구하고 최대 ~63.2%의 발전 효율을 달성할 수 있음을 확인하였으며, 최대 효율 운전점(설계점) 및 탈 설계점에서의 하이브리드 시스템 최적 운전 특성에 대한 분석을 수행하였다.

결론적으로, 본 연구는 운전 조건에 따라 스파크 점화(SI) 운전 뿐만 아니라 스파크-어시스트 예혼합압축착화(SA-HCCI or SACI)엔진으로 운전이 가능한, SAI를 사용하는 새로운 SOFC-ICE 하이브리드 시스템을 제안하였다. 이는 SOFC-ICE 하이브리드 시스템을 위한 새로운 연소 전략이며, SAI 운전의 적합성은 실제 엔진 실험을 통해 검증되었다. 따라서, 본 연구는 SAI를 새로운 하이브리드 시스템의 연소 전략으로 채택하였으며, 연료전지의 연료이용률 등 운전 조건이 변화하여도 SAI를 통해 애노드오프가스의 안정적 연소가 가능함을 확인하였다. 또한, 시스템 내 애노드/캐소드 오프가스의 열에너지 분배를 고려하여 새로운 하이브리드 시스템 구성을 설계하였으며, 최적 운전 조건에 대한 분석을 진행하였다. 이러한 연구 결과를 기반으로, 본 연구가 새롭게 제안하는 SOFC-SAI 엔진 하이브리드 시스템에서, 하이브리드 시스템의 성능, 효율 및 운전안정성이 개선되었음을 확인하였다. 따라서 본 연구 결과는 SOFC-ICE 하이브리드 시스템 개발 및 상용화에 기여할 것으로 기대된다.

주요어: 수소연료전지, 고체산화물 연료전지-내연기관 하이브리드 시스템, 합성 가스 연소, 스파크 점화, 스파크-어시스트 압축착화, 시스템 수준 모델링 및 분석, 시스템 설계, 최적 운전, 시스템 효율

학 번 : 2013 - 23058